

**MECHANICAL AND GEOLOGICAL CONTROLS  
ON THE LONG-TERM EVOLUTION OF NORMAL FAULTS**

by

*Jean-Arthur Louis Olive*

B.S., Ecole Normale Supérieure, 2007  
M.S., Institut de Physique du Globe de Paris, 2009

Submitted in partial fulfillment of the requirements for the degree of

Doctor of Philosophy

at the

MASSACHUSETTS INSTITUTE OF TECHNOLOGY

and the

WOODS HOLE OCEANOGRAPHIC INSTITUTION

February 2015

© 2015 *Jean-Arthur Louis Olive*, All rights reserved

The author hereby grants to MIT and WHOI permission to reproduce and to distribute publicly paper and electronic copies of this thesis document in whole or in part in any medium now known or hereafter created.

Signature of Author

Signature redacted

MIT/WHOI Joint Program in Oceanography / Applied Ocean Science and Engineering  
December 12, 2014

Certified by

Signature redacted

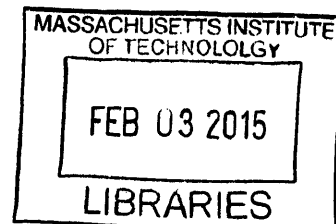
Mark D. Behn  
Associate Scientist, Department of Geology and Geophysics, WHOI  
Thesis Supervisor

Accepted by

Signature redacted

Timothy L. Grove  
Professor of Geology  
Department of Earth, Atmospheric and Planetary Sciences, MIT  
Chair, Joint Committee for Geology and Geophysics

**ARCHIVES**





# **Mechanical and Geological Controls on the Long-Term Evolution of Normal Faults**

by

JEAN-ARTHUR LOUIS OLIVE

Submitted to the MIT/WHOI Joint Program in Oceanography / Applied Ocean Science  
and Engineering on December 12, 2014 in partial fulfillment of the requirements  
for the degree of Doctor of Philosophy in Geophysics

## **Abstract**

This thesis investigates the long-term evolution of rift-bounding normal faults. To first order, the observed diversity of extensional tectonic styles reflects differences in the maximum offset that can be accommodated on individual faults during their life span. My main objective is to develop a theoretical framework that explains these differences in terms of a few key mechanical and geological controls. I start by laying out the energy cost associated with slip on a normal fault, which consists of (1) overcoming the frictional resistance on the fault, (2) bending the faulted layer and (3) sustaining the growth of topography. In Chapter 2, I propose that flexural rotation of the active fault plane enables faults to evolve along a path of minimal energy, thereby enhancing their life span. Flexural rotation occurs more rapidly in thinner faulted layers, and can potentially explain the wide range of normal fault dips documented with focal mechanisms. In Chapter 3, I show that surface processes can enhance the life span of continental normal faults by reducing the energy cost associated with topography build-up. In Chapter 4, I focus on lithospheric bending induced by fault growth, which is well described by elasto-plastic flexure models. I demonstrate that numerical models that treat the lithosphere as a visco-plastic solid can properly predict fault evolution only when the rate-dependent viscous flexural wavelength of the lithosphere is accommodated within the numerical domain. In Chapter 5, I consider the interplay of faulting and crustal emplacement at a slow mid-ocean ridge. I show that a depth-variable rate of magma emplacement can reconcile the formation of long-lived detachment faults, which requires a moderate melt supply, and the exhumation of large volumes of lower crustal material. Finally, in Chapter 6 I investigate the three-dimensional interactions between normal faults in a lithosphere of varying thickness. I suggest that large along-axis gradients in lithospheric thickness can prevent the growth of continuous faults along-axis, and instead decouple the modes of faulting at the segment center and at the segment end.

**Thesis Supervisor:** Dr. Mark Behn, Associate Scientist with Tenure, WHOI

**Chair of the Defense:** Dr. Jian Lin, Senior Scientist, WHOI

**Thesis Committee:**

Dr. Javier Escartin, Directeur de Recherche, CNRS-IPGP

Prof. Brian Evans, MIT

Prof. Yajing Liu, McGill

Dr. Brian E. Tucholke, Scientist Emeritus, WHOI



## Acknowledgements

It all started seven years ago when Dr. Mark Behn from the Woods Hole Oceanographic Institution received yet another random student email asking for a research internship. Little did I know at the time that this email would pass all of Mark's background checks (1/ "he has funding ", 2/ "my French friends approve of him") and open a whole new chapter of my life - a chapter filled with exciting science, trips to exotic locations, and lots of espressos (an estimated 3800). And now here we are. I may still not know much about baseball or the proper use of m-dashes, but I am walking out of grad school as an independent (and slightly sarcastic) scientist, which is perhaps what I am most grateful for. I look forward to future collaborations on proving that grain size reduction is the key to a good espresso, if not to Plate Tectonics, life on Earth, and the meaning of existence. *Merci infiniment*, Mark.

Many thanks also go to my thesis committee for their support over the years and to Jian Lin for being a great defense chair. Javier- I owe you more than I can list here, and I don't even know where to start. I will keep this short and thank you for your precious guidance and for inviting me on the ODEMAR cruise, which is possibly the coolest thing I've ever been a part of. I promise I will work on my GMT skills. Yajing-*merci (en québécois)* for your continued support and for introducing me to earthquake mechanics. I'm looking forward to working with you in the near future (and to numerous Montréal trips!). Brian (Tucholke)- I have enjoyed working with you and I want to thank you for teaching me how to properly map faults in numerical models. Brian (Evans)-thank you for many stimulating discussions of lithosphere rheology. I learned a lot from being your lab TA in my first year and hope we will keep in touch.

This thesis has benefited from numerous collaborations both inside and outside WHOI/MIT. I first need to thank Eric Mittelstaedt, with whom I developed the 2-D Matlab code used throughout this work and the 3-D code (HiPStER) presented in Chapter 6. We make a great team when it comes to coding, debugging, and bar hopping (not necessarily in that order). Eric- I couldn't have done it without you. Thank you for constantly reminding me that "it should work". Many thanks also go to Garrett Ito for his guidance during code development and for many great science discussions. Young B. Z. Klein- you made the 2-D code so fast that Mark started expecting even more results. I do not thank you for that. Dave May and Matt Knepley have also been incredibly helpful and patient with us as we slowly figured out the intricacies of PETSc.

I am thankful to have been adopted by a family of normal fault modelers whose illustrious members – namely Roger Buck, Don Forsyth, Luc Lavier and Eunseo Choi – have provided invaluable feedback on my work. I am also lucky to have interacted with incredibly supportive scientists at WHOI such as Rob Sohn, Jeff McGuire, Henry Dick, Meg and Maurice Tivey, Adam Soule, Debbie Smith, Hans Schouten and Frieder Klein (just to name a few), as well the APO dream team and some pretty awesome postdocs. Special thanks go to Julia Westwater (for that glass of wine on the eve of my defense, among many other things), to Dorsey Wanless, Laura Stevens, and Nathan Miller with

whom I shared the Behn of my existence, to Thibaut Barreyre, and to Masako Tominaga (Doumo Arigatou from your pocket modeler). On the MIT side, I wish to acknowledge Tim Grove, Rob van der Hilst, Alison Malcolm, Oli Jagoutz, Brad Hager, and Taylor Perron for their continued support and for providing me with great teaching opportunities. I am also indebted to my French connections, and in particular to Stéphane Rondenay, Mathilde Cannat, Fabrice Fontaine, Jean-Philippe Avouac, Edouard Kaminski, and Nicolas Chamot-Rooke, who first suggested I contact WHOI for a Masters internship. Last but not least, François Rosé has been the best geology teacher I could have hoped for as an undergraduate, *et je tenais à lui adresser mes remerciements les plus chaleureux en français dans le texte.*

It goes without saying that I owe what little sanity I have left after 5.3 years in grad school to the companionship of my fellow grad students and friends. First, a tip of my hat goes to my illustrious predecessors in EAPS: Christy, Jay "Jay-Jay" Barr, Erin, Scott, Nate, Noah, Fred, Jimmy, Vera, Emily, Casey, Evy, and many others who welcomed me to MIT/WHOI and introduced me to the art of pub trivia. Among this very special crowd, the one and only Mike Krawczynski deserves a very special *merci* for being a wonderful friend, roommate, and mentor. I have also overlapped with numerous EAPSters, JPers, and PAOCers who made life outside the "lab" extremely enjoyable. To Ben Mandler- you are a true rosbif friend and I am lucky to know you. GENAU! To Michael "Whales" Sori (18)- I just have to say "ONE MORE LONG POND". To Ruel "Truth Baron" Jerry- it has been an honor being your favorite (and only) French person in the office. By the way, Sori had your passport all along. Yodit- I cannot thank you enough for encouraging me to "simmer down" and for making the Black Hole such a wonderful place. Jill and Santiago- you are my bros, and I know we'll have many more jaguar moments. Many thanks to Frank (Listen!), Melissa, Dan (A and O), Deepak, Papa Jaap, Elena, Skylar, Kate, Aimee, Alex (E and A), Min (X and D), Bram, Abby, Ale-Alejandra, Christopher, Christine (mentee), Steve, Josh, Sara, the Fit-o-Planktons, Claire, Brian Green, Steph, Max, Marie, Sharon, Cosi, René, Kelsey, Back Bar, Jordon, Greg, Helen, Annie, Bloc 11, and all my geology-related friends. Thank you also to my friends from outside the Green Building: John Platt, Harriett, Joël (*tu lunches?*), Rémi (*#espritcompétitif*), and to my roommates at 25 Webster: Claudia, Rapharel (*Molhar as plantas no fim de semana*), Estelle, Thibaut, and Lisa. Thibaut, *merci pour ton schedule et les heures de GTA en fin de thèse (j'adore le concept).*

West of Boston and Woods Hole, I am thankful for my many friends in California and Idaho, starting with Luca Malatesta who introduced me to geomorphology and to the LA hipster scene, which can be surprisingly intertwined. West Coast Swiss Coast. I am also forever grateful to the Lilley-pad gang for showing me the real 'Murika. East of Massachusetts - while Boston and Paris have spread apart by another 13 cm during the making of this thesis - I have remained close to many people on the old continent who made every visit to France a terrific time. This one is for you, Kristel de Quartz, Barbara, Dubi (ah ouais?), Benjamin, Kiki, Lieutenant Dan, Le Cerf, PSG, Amaya, Matthias, Claire, Bérénice, Guillaume, Ronan, Samuel, Alexis, Dorothée, et tous les autres... To Alexandre, Romain, and Edouard- We'll always have Alicudi. Je vous suivrais au bout du

monde, surtout si on y va en ferry SIREMAR (et si Ed' conduit, H supervise et Al' gère mon manque de café).

To Niya- thank you for keeping me as sane as you possibly can and for putting up with my many (normal) faults.

Last but not least, je remercie mes parents et ma grande sœur préférée pour leur soutien et leur confiance. Je souhaite dédier cette thèse à Pépé, qui l'aurait lu, aurait marqué une longue pause et aurait dit:

"Ah oui, peut-être."

---

Funding was provided by the National Science Foundation through grants OCE-1154238, EAR-0854673, and by a Charles M. Vest Presidential Fellowship.

*"Il a bossé pendant des jours  
Tâchant avec amour d'améliorer l'modèle  
Quand il déjeunait avec nous  
Il dévorait d'un coup sa soupe aux vermicelles"*

**Boris Vian, *La Java des Bombes Atomiques***

# Contents

<b>Abstract</b>	<b>3</b>
<b>Acknowledgements</b>	<b>5</b>
<b>1. Introduction</b>	<b>13</b>
<b>2. Rapid rotation of normal fault induced by lithospheric flexure: An explanation for the global distribution of normal fault dips</b>	<b>19</b>
2.1 Introduction .....	20
2.2 Work minimization model for fault rotation .....	23
2.3 Semi-analytic results for fault rotation .....	30
2.3.1 Elastic (infinitely strong) faulted layer .....	30
2.3.2 Elastic / pseudo-plastic faulted layer .....	32
2.4 Numerical models of fault rotation in an elasto-plastic layer .....	35
2.5 Discussion .....	38
2.5.1 Work minimization and dip evolution .....	38
2.5.2 Rheologic controls on rotation rate and life span of normal faults .....	41
2.5.3 Implications for extensional rift systems .....	45
2.6 Conclusions .....	49
Appendix 2.1 Calculation of the bending work term $W_{INT}$ .....	50
Appendix 2.2 Equations for fault dip, work and stress as a function of heave .....	51
<b>3. Modes of extensional faulting controlled by surface processes</b>	<b>55</b>
3.1 Introduction .....	56
3.2 Numerical experiments .....	58
3.3 Results .....	62
3.4 Topographic forcing on fault life span .....	66
3.5 Application to rift systems .....	69
3.6 Conclusions .....	70
Appendix 3.1 Kinematic model of fault rotation .....	71
Appendix 3.2 Comparison with the energy minimization model of Chapter 2 .....	73
<b>4. The role of elasticity in simulating long-term tectonic extension</b>	<b>77</b>
4.1 Introduction .....	78
4.2 Methods .....	80
4.2.1 Numerical methodology .....	80
4.2.2 Implementation of visco-elasticity .....	81
4.2.3 Implementation of plasticity .....	83
4.2.4 Model setup .....	84

4.3 Numerical results .....	85
4.3.1 Fault-induced topography .....	87
4.3.2 Fault dip .....	89
4.3.3 Fault life span .....	91
4.4 Semi-analytical approach: simple scalings to guide the interpretation of numerical simulations .....	93
4.4.1 Fault-induced topography .....	93
4.4.2 Fault rotation .....	99
4.4.3 Fault life span .....	102
4.5 Concluding remarks .....	103
 Appendix 4.1 Fault-induced topography in a viscous lithosphere .....	106
 <b>5. Oceanic core complex structure controlled by the depth-distribution of magma emplacement</b> .....	<b>113</b>
5.1 Introduction .....	114
5.2 Numerical simulations of melt emplacement near a growing fault .....	117
5.3 Results .....	120
5.4 Discussion .....	124
5.5 Conclusions and perspectives .....	128
 <b>6. The effect of lithospheric thickness variations on the three-dimensional growth of normal faults</b> .....	<b>131</b>
6.1 Introduction .....	132
6.2 Numerical methodology: the HiPStER approach .....	137
6.2.1 Governing equations and discretization .....	138
6.2.2 Numerical strategy for solving the linear system .....	142
6.3 Numerical experiments of fault evolution in a brittle layer of varying thickness .....	143
6.4 Results .....	146
6.4.1 Variations in along-axis slope with constant average lithospheric thickness .....	146
6.4.2 Variations in average lithospheric thickness .....	158
6.4.3 Fault evolution around an along-axis notch .....	159
6.5 Discussion .....	160
6.5.1 Patterns of initial strain localization .....	160
6.5.2 Continuity of faults along an extension segment .....	162
6.5.3 Fault displacement profiles and fault linkage .....	166
6.5.4 On the applicability of 2-D scalings to 3-D fault growth .....	166
6.5.5 Potential comparisons between models and observables .....	168
6.6 Conclusions and perspectives .....	170
 <b>References</b> .....	<b>173</b>





# **Chapter 1:**

## **Introduction**

A fundamental feature of plate tectonics is the rifting of continental lithosphere followed by the opening of a new ocean basin. These processes are the surface manifestation of large-scale ( $10^3$  km) divergent flow in the Earth's mantle, and yet active rifting is focused within relatively narrow zones ( $\leq 10^2$  km) termed extensional plate boundaries. This discrepancy in scale reflects the ability of the lithosphere to localize deformation through a combination of ductile creep and brittle failure. In this thesis I examine the long-term growth of normal faults, which are highly localized brittle shear zones that accommodate extension in the upper part of the lithosphere. Normal faults display a variety of morphologies from steep, step-like half-grabens to large-offset detachments exhuming lower-crustal units in core complexes. My main goal throughout this work is to build a simple mechanical framework accounting for the diversity of normal fault styles. To do so, I will investigate key mechanical and geological parameters controlling how much offset can be accommodated on a single normal fault before it becomes mechanically favorable to break a new one. Specifically, quantifying the mechanics that control fault life span is important for understanding rift morphology because they determine whether an extensional plate boundary is more likely to feature multiple short-offset faults or a few large-offset detachments.

My thesis is broadly divided into 5 inter-related studies of normal fault evolution. In Chapter 2, I set up the problem of normal fault growth as an energy balance and discuss the effect of fault rotation on fault longevity. Chapter 3 focuses on the gravitational energy cost associated with topography build-up during faulting, and establishes that erosion and sedimentation can enhance fault life span by relieving a portion of the topographic forcing. Chapter 4 investigates the flexural response of the

lithosphere to fault growth from a rheological perspective, and assesses the role of elasticity in numerical models of tectonic extension. In Chapter 5, this theoretical framework is applied to faulting at slow-spreading mid-ocean ridges, where crustal accretion accommodates a significant fraction of the extension in a depth- and time-variable manner. Finally, Chapter 6 presents preliminary results from 3-D simulations of fault growth in a lithosphere of varying thickness. The corresponding numerical methodology is described, and perspectives for modeling rift dynamics in 3-D are discussed. Below I provide a more detailed description of the fundamental mechanical problem that underlies this thesis, and outline the contribution of each chapter toward its resolution.

The Earth's lithosphere behaves as a frictional material, in which there exists an energetically optimal orientation at which faults form. This orientation is associated with the lowest deviatoric failure stress. If the least compressive stress is sub-horizontal—a reasonable assumption near the surface or seafloor in an extensional setting—then the optimal normal fault dip is about  $60^\circ$  for a friction coefficient of 0.6. While this theory does a good job at describing the onset of faulting, it cannot predict the evolution of the fault as it accumulates finite offset. When considered over time scales longer than many seismic cycles, the long-term displacement field is tangential to the fault in its vicinity and locally features a significant vertical component. Far from the fault, however, the displacement field approximates that of a rigid plate undergoing horizontal translation.

This discrepancy between the near field and the far field must be accommodated by internal deformation of the footwall and hanging wall blocks and the growth of topography. These processes have an energy cost which accumulates as fault offset grows and adds to the dissipation of frictional energy along the fault. At some point, it becomes energetically favorable to break a new fault than to sustain slip on the initial fault. The longevity of slip on a given normal fault is therefore controlled by the rate at which the various energy costs increase with increasing fault heave. Assuming that (1) the faulted layer is best described as an elasto-plastic solid, and (2) the effect of an underlying viscously creeping layer can be neglected, then it can be shown that the thickness of the faulted layer is the first-order control on the rate of increase of the various energy components. This rate is more rapid in thicker faulted layers, leading to shorter fault life

spans and the development of rifts characterized by multiple small faults. To first order, this analysis is consistent with the absence of large-offset detachments at young, immature rifts characterized by a large effective elastic thickness and / or a thick seismogenic layer. However, it does not explain why oceanic detachment faults are more commonly found near the ends of slow spreading mid ocean ridge segments, where the lithosphere is expected to be thicker than at segment centers. This paradox suggests that in order to fully understand the diversity of faulting modes, additional controls beyond the faulted layer thickness must be considered, and some of the basic assumptions of finite extension theory may have to be re-evaluated.

In Chapter 2, I focus on the evolution of fault dip, a central parameter in the energy budget of a growing normal fault. Recognizing that a shallow-dipping fault induces less lithospheric flexure while offering more frictional resistance to slip, I postulate that normal faults evolve along the lowest-energy path that balances these two effects. This predicts that faults should rotate rapidly toward shallower angles, and that rotation rates should be faster in thinner faulted layers. I validate these two predictions using 2-D numerical simulations of fault growth in an elasto-plastic layer. I further propose that the rotation mechanism at play is a moment imbalance in the displacement field associated with lithospheric flexure. This potentially explains why most seismically active normal faults have dips between  $30^\circ$  and  $60^\circ$  as opposed to the  $60^\circ$  angle predicted by Andersonian theory. Finally, I propose that the similarity in fault dip distributions across extensional plate boundaries reflects a similarity in the mechanical thickness of the faulted layer in many rift settings.

In Chapter 3, I focus on the energy cost associated with the growth of topography during normal faulting, a term that was ignored in the analysis conducted in Chapter 2. Specifically, I assess whether the redistribution of surficial masses due to erosion and sedimentation can significantly affect the growth of normal faults by modulating this energy term. I conduct 2-D numerical simulations of fault growth where the surface boundary condition models the effect of erosion and short-range sediment transport. I show that surface processes acting at rates comparable to, or faster than fault slip can enhance fault longevity by a factor that is greater in thinner faulted layers. I therefore propose that surface processes are essential in allowing sub-aerial rift-bounding faults to

accumulate offsets as large as  $\sim 10$  km. Coincidentally, I show that surface processes have little influence on fault rotation kinematics, which are best explained by flexural processes. I develop a strictly kinematic model for fault rotation and incorporate it in a fully consistent force balance model of normal fault longevity that does not rely on empirical scalings for the bending component.

Based on the results of Chapter 2 and 3, it appears that capturing the physics of elasto-plastic flexure is essential for predicting the evolution of normal faults. However, many numerical models of long-term tectonic extension treat the lithosphere as a visco-plastic solid for ease of implementation. In Chapter 4, I assess the consequences of this assumption by systematically comparing 2-D numerical simulations of normal fault growth in an elasto-plastic and a visco-plastic layer. I show that the first-order effect of faulted layer thickness on rotation kinematics and fault life span is similar in visco-plastic and elasto-plastic models. However, the visco-plastic description introduces a dependence of the results on the imposed extension rate. At faster extension rates, visco-plastic faulted layers tend to behave as rigid solids, which suppresses fault rotation and enhances fault life span. In order to quantitatively interpret this result, I derive the rate-dependent bending wavelength of a viscous thin plate undergoing faulting. I show that the elasto-plastic and visco-plastic models agree best when this wavelength is fully resolved within the numerical domain. This study has broad implications for numerical studies of long-term lithosphere dynamics that incorporate localized brittle deformation.

In Chapter 5, I return to the paradox of fault life span at mid-ocean ridges, where widespread detachment faulting appears to occur preferentially in regions of thicker lithosphere (contrary to the predictions in Chapters 2 and 3). In these settings, normal faulting occurs alongside with the emplacement of new oceanic crust, which typically accommodates a large fraction of the total plate separation. Earlier modeling studies proposed that magmatic emplacement leads to off-axis migration of normal faults into thicker lithosphere, resulting in rapid abandonment and short fault life span. These studies suggested that detachment fault growth was only possible in areas where magma supply was moderate, allowing faults to grow in thin axial lithosphere without migrating off-axis. However, moderate melt supply seems inconsistent with the large amounts of lower crustal material often exhumed in the footwall of oceanic detachment faults. To

reconcile the theory with the observations, I conduct 2-D numerical simulations of normal fault growth coupled with depth-dependent rates of crustal accretion. I show that faulting patterns are controlled solely by the rates of magma intrusion above the brittle-ductile transition, with moderate rates favoring long-lived faults. Further, I show that materials intruded beneath the brittle-ductile transition during detachment fault growth are symmetrically partitioned between the fault side and the conjugate side, and that detachment fault growth is unaffected by changes in the rates of crust emplacement in the ductile regime. This suggests that the depth-distribution of melt emplacement may be a more critical control on detachment fault growth than the total melt supply.

Chapters 2 through 5 are based on two-dimensional models, which assume that the along-axis dimension of normal fault systems greatly exceeds its vertical and horizontal length scales, i.e., the thickness and flexural wavelength of the faulted layer. However, as exemplified by slow-spreading ridges, the faulted layer thickness and mechanical properties of extensional plate boundaries are inherently three-dimensional. Developing 3-D numerical models of long-term tectonic extension is challenging due to their heavy computational requirements and the sharp rheological contrasts that are typical of localized brittle behavior. In Chapter 6 I report initial results from a new finite-difference code solving for visco-elasto-plastic flow in a 3-D continuum, which I developed in collaboration with Pr. Eric Mittelstaedt (University of Idaho). Here I focus on three-dimensional normal fault growth in a brittle layer that thickens along-axis. I investigate whether (1) a single continuous fault develops following the 2-D scalings dictated by the average layer thickness, or whether (2) distinct fault segments develop in regions of varying thicknesses, with complex linkage structures. I further discuss new perspectives for 3-D numerical modeling of extensional tectonics.

In summary, this thesis focuses on the long-term evolution of normal fault systems as they interact with surface processes, magmatic processes, and each other in two and three dimensions. The models presented here make a number of predictions that can be tested with a combination of geological observation and geophysical methods. Conversely, three-dimensional models of normal fault growth hold great potential to inform the structural interpretation of direct geological observations at the seafloor, or at continental rifts.



## **Chapter 2:**

# **Rapid flexural rotation of normal faults: An explanation for the global distribution of normal fault dips<sup>1</sup>**

### **Abstract**

We present a mechanical model to explain why most seismically active normal faults have dips much lower (30–60°) than expected from Anderson-Byerlee theory (60–65°). Our model builds on classic finite extension theory, but incorporates rotation of the active fault plane as a response to the build-up of bending stresses with increasing extension. We postulate that fault plane rotation acts to minimize the amount of extensional work required to sustain slip on the fault. In an elastic layer, this assumption results in rapid rotation of the active fault plane from ~60° down to 30–45° before fault heave has reached ~50% of the faulted layer thickness. Commensurate, but overall slower rotation occurs in faulted layers of finite strength. Fault rotation rates scale as the inverse of the faulted layer thickness, which is in quantitative agreement with 2D geodynamic simulations that include an elasto-plastic description of the lithosphere. We show that fault rotation promotes longer-lived fault extension compared to continued slip on a high angle normal fault, and discuss the implications of such a mechanism for fault evolution in continental rift systems and oceanic spreading centers.

---

<sup>1</sup> Published as: Olive, J.-A., and M. D. Behn (2014), Rapid rotation of normal faults due to flexural stresses: An explanation for the global distribution of normal fault dips, *J. Geophys. Res.*, 119.

## 2.1. Introduction

Normal faults are highly localized zones of brittle shear deformation that accommodate extension in the crust and lithosphere. Andersonian theory predicts that in an extensional system normal faults will form with a dip angle of 60–65° [Anderson, 1951], corresponding to a coefficient of friction of 0.6–0.85 common for most rock types [Byerlee, 1978]. However, this prediction is not consistent with fault dips inferred from focal mechanisms of normal faulting earthquakes large enough to rupture a representative portion of the fault plane. The global distribution of active fault dips resembles a Gaussian distribution centered on 45° and limited to angles between 20° and 65° [Jackson and White, 1989; Thatcher and Hill, 1991; Collettini and Sibson, 2001; Yang and Chen, 2008] with a few notable outliers at very low [Abers, 1991; Abers et al., 1997] and very high [Yang and Chen, 2008] angles (Figure 2-1). A similar pattern of fault dips is observed at the scale of individual rift systems [Jackson and White, 1989].

One hypothesis to reconcile Andersonian theory with the observed distribution of fault dips is to assume a low coefficient of friction ( $< 0.3$ ) associated with the presence of weak minerals [e.g., serpentine; Escartin et al., 1997] in the fault zone. This could account for faults initiating at dips closer to 50°, but would not allow dips lower than 45° in an Andersonian stress field where the principal stresses are horizontal and vertical. Alternatively, accumulated elastic stresses in the faulted layer could cause significant deviation of the principal stresses from the horizontal / vertical [Spencer and Chase, 1989]. Such elastic stresses could arise from uncompensated surface or Moho topography and/or shear from an underlying viscous layer. Another possibility is that intermediate-dipping normal faults initiate as the reactivation of thrust faults under an Andersonian, extensional state of stress. While it is mechanically easiest to reactivate fault planes dipping at 60°, it is not significantly more difficult to reactivate planes dipping in the 40–80° range [Collettini and Sibson, 2001]. Although reactivation may be an important process in some continental rifts, it clearly does not apply to oceanic spreading centers where faulting occurs in newly formed lithosphere. Further, each of these mechanisms requires a specific set of conditions that relaxes the assumptions of Andersonian theory. It is therefore unclear to what extent these processes (or any combination of them) would be reflected in the dip distribution at the scale of both global

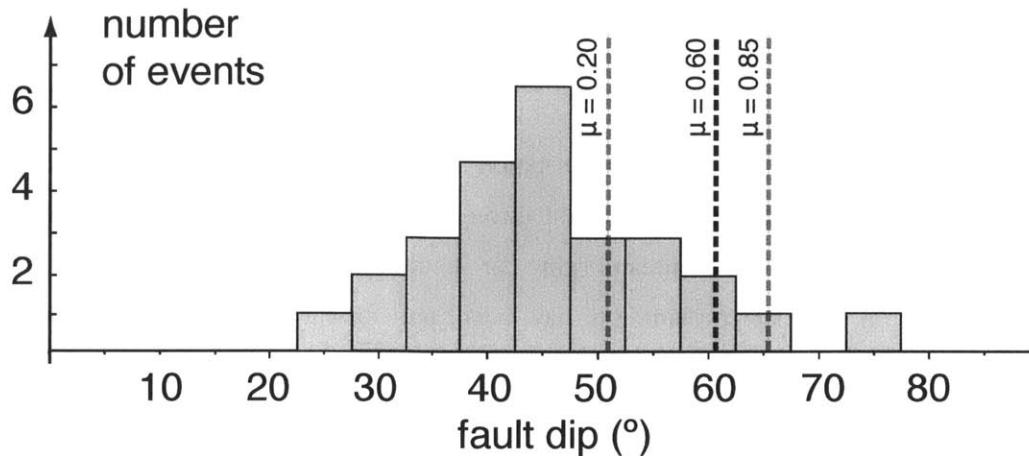


**Figure 2-1.** Dip distribution of 28 large ( $M_w > 5$ ) dip-slip (rakes within  $30^\circ$  of downdip direction) normal fault ruptures (modified from *Yang and Chen* [2008]). Fault dips are inferred from focal mechanisms where local geology allows the nodal plane that likely corresponds to the rupture plane to be determined. Data from the compilation of *Jackson and White* [1989] and *Collettini and Sibson* [2001], complemented by data from *Abers et al.*, [1991; 1997] (low-dip end) and *Yang and Chen* [2008] (high-dip end).

and individual rifts. It has also been suggested that the  $45^\circ$  mode of the dip distribution corresponds to the dip of pressure-insensitive ductile shear zones beneath the seismogenic layer into which faults root [*Thatcher and Hill*, 1991]. While this process may affect the dip distribution at all scales, it does not account for the spread of the distribution and is not well characterized from a mechanical perspective.

Another class of models that have been proposed to explain the observed distribution of fault dips argues that normal faults initiate at Andersonian angles of  $60\text{--}65^\circ$  but later rotate to shallower angles. One popular mechanism is a domino-style rotation of a set of parallel normal faults [*Proffett*, 1977; *Jackson and White*, 1989] down to a frictional lockup angle of  $\sim 30^\circ$  [*Collettini and Sibson*, 2001] at which slip is no longer permitted, and a new set of steep faults forms to accommodate extension. In an Andersonian state of stress, slip on faults dipping  $< 30^\circ$  is only possible when fluid pressure exceeds the horizontal tensile stress. Such high fluid pressure is difficult to envision in settings where tensional stress promotes high permeability and drained conditions, which could explain why the observed range of normal fault dips is largely

greater than  $30^\circ$ . However, the domino model is purely geometric and does not predict rotation rates or account for the possibility that a fault could become inactive before it reaches the lockup angle.

An alternative model for fault rotation involves isostatic adjustment of the footwall in response to tectonic denudation through plastic flow, resulting in low-angle detachment surfaces exposed as metamorphic core complexes [Buck, 1988; Wernicke and Axen, 1988]. A similar explanation has been put forward to explain low-angle detachments (or oceanic core complexes) found at slow- and ultraslow-spreading mid-ocean ridges, and has been termed the “rolling hinge” model [Buck, 1988; Lavier *et al.*, 1999]. These models, which emphasize the effect of isostasy, are only valid for faults that have accommodated very large offsets (10–50 km) and explain the shallow dips of exposed fault surfaces rather than active fault planes. However, a recent numerical study of normal fault evolution [Behn and Ito, 2008] reported rotation of active fault planes from  $\sim 55^\circ$  down to  $\sim 35^\circ$  over less than 4 km of extension and prior to any rollover of the exhumed fault surface. More recently, Choi and Buck [2012] reported similar rotation in numerical simulations, which they attributed to flexural processes. They further proposed that flexural rotation of the active portion of detachment faults to shallower angles could lead to the formation of splay faults in the hanging wall, provided the detachment has retained sufficient strength. However, Choi and Buck [2012] did not investigate the physical mechanism by which flexure of the brittle layer leads to rotation of the active fault plane.

In this study, we present a simple mechanical framework for understanding rapid normal fault rotation after initiation at a high angle. We build on the classic finite extension theory of Forsyth [1992] and Buck [1993], and consider the effect of flexure on the optimal dip of a fault. Specifically, we derive the simplified energy budget of a growing fault and propose that fault rotation occurs in a way that systematically minimizes the external work required to sustain growth. We explore this hypothesis with a simple semi-analytical model that first considers a purely elastic, infinitely strong faulted layer. This allows us to identify the key factors that control fault rotation kinematics and fault life span. We then incorporate a simplified treatment of plasticity in the semi-analytical model to account for the finite strength of the lithosphere. In order to

show that our simplified model captures the first-order physics of the system, we then compare our semi-analytic results with more realistic 2D geodynamic simulations of normal fault growth in an elasto-plastic layer, which do not explicitly involve the assumption of “work minimization”. Finally, we discuss applications of these models to fault evolution and the distribution of active fault dips in rift systems worldwide.

## 2.2 Work-minimization model for fault rotation

Lithospheric flexure in response to slip on a normal fault has long been identified as a key mechanism to explain the topographical features of grabens and core-complexes [e.g., *Vening-Meinesz*, 1950; *Buck*, 1988; *King et al.*, 1988]. It is therefore expected that the associated build-up of flexural stresses should feed back and influence subsequent fault evolution. *Forsyth* [1992] showed that flexure of a faulted layer due to finite offset on a normal fault acts to decrease its optimal dip (i.e., the dip that requires the least horizontal tension to keep the fault active) down to almost 30° after a few kilometers of extension. He showed that in order for a fault to remain active, horizontal tension must overcome frictional resistance as well as the build-up of topography and related flexural stresses. *Forsyth* [1992] proposed that faults would be abandoned when it becomes mechanically easier to break a new fault than to sustain slip on a preexisting fault. Using the assumption that fault dip does not change during growth, he concluded that only faults initiated at a shallow angle could accumulate large offsets because they would remain relatively close to their optimal dip during growth. This force balance model was later refined by *Buck* [1993] and *Lavier et al.* [2000], who treated the faulted layer as an elasto-plastic rather than purely elastic thin plate. This assumption led to the prediction that normal faults would stay active longer when the faulted layer is thinner, in agreement with geological observations [*Lavier and Buck*, 2002]. However, like *Forsyth* [1992], these models did not explicitly consider the possibility that fault dip may readjust to the build-up of bending stresses, although the models of *Lavier et al.* [2000] did feature rotation of the shallowest portion of the active fault due to flexure. Here we present a mechanism by which flexural stresses could induce a rapid decrease in the dip of a growing fault, and discuss its implications for fault life span. We propose that faults

rotate in response to flexure of the footwall and hanging wall, and do so in a manner that systematically minimizes the amount of work required to sustain slip on the fault.

Let us consider the energy balance on a growing normal fault, following the approach of *Cooke and Murphy* [2004]. We assume a fault of dip  $\theta$ , which cuts through a layer of thickness  $H$  and accumulates a horizontal extension  $h$  (Figure 2-2). Far field tensional forces supply mechanical work  $W_{EXT}$  to the system. This work can be related to the average tensional stress ( $\sigma_R$ ) by

$$W_{EXT} = \int_0^h \sigma_R H dh \quad (2.1)$$

In order to sustain slip on the fault, the external work must overcome the frictional resistance along the fault surface ( $W_{FRIC}$ ), and supply mechanical energy for bending the hanging wall and footwall ( $W_{INT}$ ). In addition, work may be done against gravity ( $W_{GRAV}$ ) as the fault creates topography, energy may be spent breaking new fault surface ( $W_{PROP}$ ), and some work may be dissipated in the form of earthquakes ( $W_{SEIS}$ ).

Since topography is modeled as the flexural readjustment of rigid displacement across a fault under gravity (see below and Appendix 2.1), the work required to generate and sustain topography is included in  $W_{INT}$ , and we ignore all other sources of work done by or against gravity ( $W_{GRAV} = 0$ ). Further, we assume that extension is accommodated on a single normal fault and that no new fault surfaces are formed as long as the fault is actively slipping. We can therefore neglect the energy cost of breaking intact lithosphere ( $W_{PROP} = 0$ ). Lastly, the earthquake energy term ( $W_{SEIS}$ ) integrates the drop in shear stress that occurs during each seismic rupture over many seismic cycles. This stress drop corresponds to a drop in fault strength that occurs when transitioning from static to dynamic friction. Overall, this term can be viewed as an intermittent dissipation of a portion of the fault's frictional energy. Here we consider only a continuously growing fault that slips aseismically and neglect  $W_{SEIS}$ . We note, however, that if the fault grows by repeated earthquakes, its long-term averaged strength is perhaps best represented by its dynamic shear strength. This can be incorporated in our model by considering a lower friction coefficient in a continuously slipping fault.

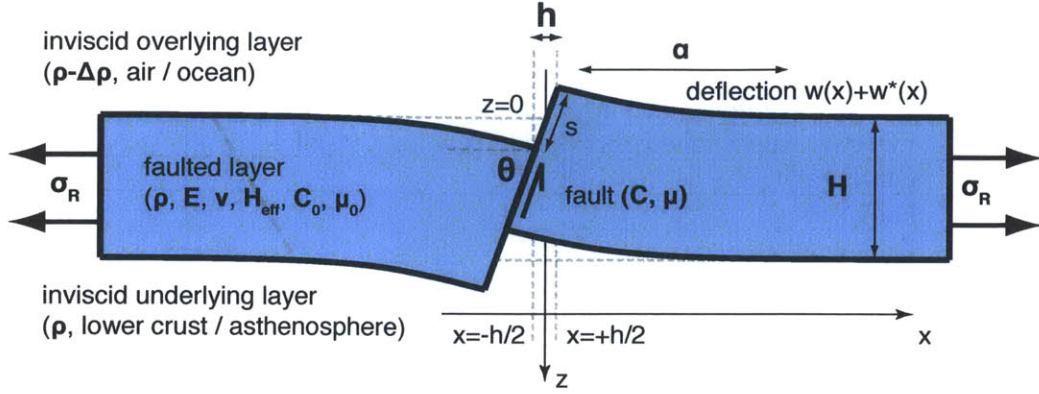


**Figure 2-2.** Schematic set-up of our semi-analytical model for fault evolution in an elastic / pseudo-plastic layer. A far-field tensional stress,  $\sigma_R$ , drives extension along the fault (of heave  $h$ ) and the associated deflection of the hanging wall and footwall blocks. The fault zone has a weak rheology characterized by a friction coefficient  $\mu$  and cohesion  $C$ . Far from the fault, intact rocks (with  $\mu_0$ ,  $C_0$ ) deform elastically or plastically with an effective elastic thickness  $H_{eff}$ . Slip on the fault ceases when  $\sigma_R$  becomes sufficient to break a new fault in intact rock.

The simplifying assumptions listed above yield the following work balance:

$$W_{EXT} = W_{FRIC} + W_{INT} \quad (2.2)$$

The frictional dissipation term is obtained by integrating shear stress multiplied by slip along the fault surface:

$$W_{FRIC} = \int_0^L \tau(l)s(l)dl \quad (2.3)$$

By considering average stresses through the faulted layer and uniformly distributed slip on the fault plane, we can write

$$W_{FRIC} = \tau s L \quad (2.4)$$

where  $\tau$  is shear stress,  $s$  is the fault offset ( $h/\cos\theta$ ) and  $L$  is the fault length ( $H/\sin\theta$ ). Slip on the fault is permitted as long as the Mohr-Coulomb criterion is met:

$$|\tau| = \mu|\sigma_n| + C \quad (2.5)$$

where  $\mu$  is the coefficient of friction,  $\sigma_n$  is normal stress on the fault surface, and  $C$  is cohesion. A summary of notations is provided in Table 2-1.

Symbol	Definition	Value
$H$	Thickness of the faulted layer	
$H_{eff}$	Effective elastic thickness of the faulted layer ( $\leq H$ )	
$h$	Fault heave	
$s$	Fault offset	
$L$	Fault length	
$\rho$	Density of the faulted layer (and underlying layer)	2700-3300 $\text{kg.m}^{-3}$
$\Delta\rho$	Density contrast between the faulted layer and the overlying fluid layer	2300-2700 $\text{kg.m}^{-3}$
$g$	Gravitational acceleration	$9.81 \text{ m.s}^{-2}$
$\sigma_R$ , $\sigma_R^{BREAK}$	Horizontal tensional stress needed to sustain faulting, horizontal tensional stress required to break a new fault in intact rock	
$F_R$	Horizontal tensional force needed to sustain faulting ( $= H \sigma_R$ )	
$\tau$	Shear stress resolved on the fault	
$\sigma_n$	Normal stress resolved on the fault	
$C, C_0$	Cohesion of the fault zone, of the intact layer	
$\mu, \mu_0$	Friction coefficient in the fault zone, in the intact layer	
$\theta, \theta_0$	Dip of the fault, initial (optimal) dip of the fault	
$E$	Young's modulus	30-100 GPa
$\nu$	Poisson's ratio	0.25-0.5
$\eta_L$	Viscosity of the faulted layer (in numerical model)	$10^{24} \text{ Pa.s}$
$\eta_S$	Viscosity of the ocean layer (in numerical model)	$10^{17} \text{ Pa.s}$
$\eta_A$	Viscosity of the asthenosphere (in numerical model)	$10^{18} \text{ Pa.s}$
$U$	Spreading half-rate (in numerical model)	1 cm/yr
$D$	Flexural rigidity of the faulted layer	
$\alpha$	Flexural wavelength of the faulted layer	
$w(x)$	Flexural response of the faulted layer due to offset on the fault	
$w^*(x)$	Topography of the faulted layer driven by rigid motion along the fault	
$w^T(x)$	Total topography induced by offset on the fault	
$W_{INT}$	Mechanical work done internally straining (bending) the faulted layer	
$W_{FRIC}$	Work done against friction on the fault	
$W_{EXT}$	Total external work supplied to the system = $W_{FRIC} + W_{INT}$	

**Table 2-1.** Summary of notation and values for reference parameters.

Assuming an Andersonian stress state and an average lithostatic stress of  $-\rho gH/2$  in the faulted layer, the shear stress required for failure along the fault writes:

$$\tau = \frac{C + \mu\rho gH/2}{\sin\theta \cos\theta + \mu \sin^2\theta} \cos\theta \sin\theta \quad (2.6)$$

The frictional energy dissipated along the fault is therefore written:

$$W_{FRIC} = \frac{C + \mu\rho gH/2}{\sin\theta \cos\theta + \mu \sin^2\theta} Hh \quad (2.7)$$

The second component of work in Equation (2.2) corresponds to the internal strain energy stored in the faulted layer as the footwall and hanging wall are bent upward and downward, respectively.  $W_{INT}$  is defined as the integral of stress multiplied by strain over the faulted layer:

$$W_{INT} = \int_V \frac{1}{2} \sigma_{ij} \epsilon_{ij} dV \quad (2.8)$$

To estimate  $W_{INT}$ , we first treat the faulted layer as a thin elastic plate of thickness  $H$  with Young's modulus  $E$  and Poisson's ratio  $\nu$ , overlying an inviscid fluid half-space of the same density [Buck, 1988; 1993; Forsyth, 1992] (Figure 2-2). The density contrast between the layer and the overlying fluid (air or ocean) is  $\Delta\rho$ . This simplifying assumption allows us to relate  $W_{INT}$  to the deflection of the footwall and hanging wall blocks  $w(x)$ :

$$W_{INT} = \frac{1}{2} \int_{-\infty}^{+\infty} D \left( \frac{\partial^2 w}{\partial x^2} \right)^2 dx \quad (2.9)$$

where  $D$  is the flexural rigidity of the faulted layer,

$$D = \frac{EH^3}{12(1-\nu^2)} \quad (2.10)$$

The plate deflection resulting from slip on the fault is modeled by adding the contribution of (a) rigid motion of the hanging wall and footwall blocks along the fault and (b) flexure of the footwall and hanging wall blocks in response to gravity [Weissel and Karner, 1989]. If  $w^*(x)$  denotes the topography resulting from step (a) alone, the deflection  $w(x)$  corresponding to step (b) can be calculated as the flexural response to the load exerted by  $w^*(x)$ . This is achieved by solving the thin plate equation,

$$D \frac{d^4 w}{dx^4} + \Delta \rho g w = -\Delta \rho g w^*(x) \quad (2.11)$$

The final topography resulting from steps (a) and (b) is simply  $w^T(x) = w^*(x) + w(x)$ . Details of the solution method are given in Appendix 2.1. Specifically, we show that  $W_{INT}$  can be written as

$$W_{INT} = \frac{D}{16\alpha} \tan^2 \theta \Psi\left(\frac{h}{\alpha}\right) \quad (2.12)$$

where  $\alpha$  denotes the flexural wavelength of the faulted layer

$$\alpha = \left(\frac{4D}{\Delta \rho g}\right)^{\frac{1}{4}} \quad (2.13)$$

and  $\Psi(y)$  is a dimensionless function described in Appendix 2.1.

Combining Equations (2.7) and (2.12), we now have an expression for the frictional and flexural work components as a function of fault heave and dip (see Appendix 2.2 for details and function definitions).

$$W_{EXT} = \underbrace{A_F(\theta) R_F(h)}_{W_{FRIC}} + \underbrace{A_I(\theta) R_I(h)}_{W_{INT}} \quad (2.14)$$

We then postulate that flexure acts to rotate the active fault plane such that the energy required to sustain extensional deformation is minimized. In other words, fault dip evolves to minimize the increase in tensional work ( $W_{EXT}$ ) with increasing extension (Figure 2-3). In mathematical terms, fault dip can be determined for a given amount of extension by the constraint

$$\frac{\partial}{\partial \theta} \left( \frac{\partial W_{EXT}}{\partial h} \right) = 0 \quad (2.15)$$

In the framework of the *Forsyth* [1992] force balance model, this is equivalent to allowing faults to rotate toward their optimum dip angle. Combining Equations (2.14) and (2.15) allows us to formulate a nonlinear differential equation that we solve with a 4<sup>th</sup> order Runge-Kutta method (Appendix 2.2). The initial fault dip,  $\theta_0$ , is assumed optimal with respect to an Andersonian stress field and therefore only depends on the coefficient of friction of the host rock:

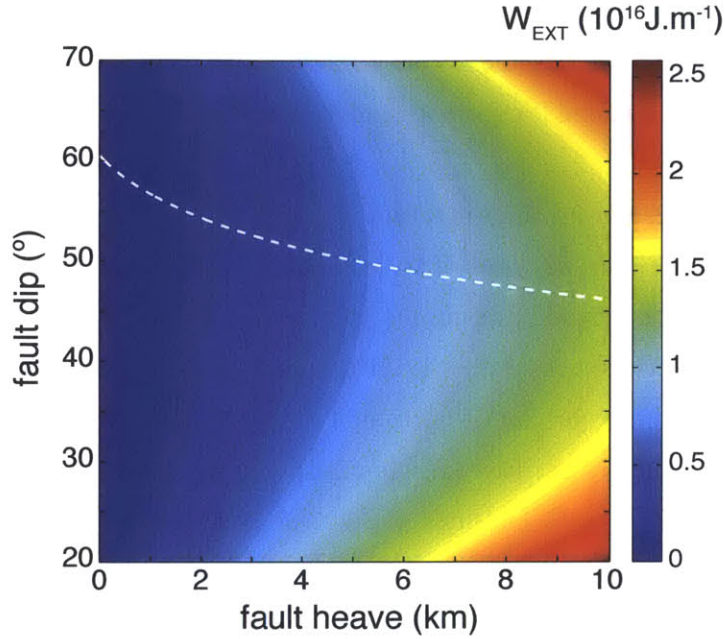


**Figure 2-3.** External work ( $W_{EXT}$ ) required to keep a normal fault active as a function of fault dip and heave for increasing amounts of extension in a 10 km thick elastic (infinitely strong) layer. In our model, faults grow such that their dip evolves to shallower angles in order to minimize the increase in external work  $W_{EXT}$ . This corresponds to the lowest-energy path represented by the white dashed line.

$$\theta_0 = \frac{\pi}{2} - \frac{1}{2} \tan^{-1} \left( \frac{1}{\mu_0} \right) \quad (2.16)$$

$\theta_0$  is necessarily greater than  $45^\circ$  and is equal to  $\sim 60^\circ$  and  $\sim 65^\circ$  for  $\mu_0 = 0.6$  and  $0.85$ , respectively (Figure 2-1). We can then calculate fault dip as well as the various work terms as a function of increasing heave. The average horizontal tension that drives extension on the fault can also be obtained from Equation (2.1):

$$\sigma_R = \frac{1}{H} \frac{\partial W_{EXT}}{\partial h} \quad (2.17)$$

A fault is abandoned when  $\sigma_R$  becomes greater than  $\sigma_R^{BREAK}$ , the stress required to break a new fault in intact lithosphere (friction  $\mu_0$ , cohesion  $C_0$ ) [Forsyth, 1992]:

$$\sigma_R^{BREAK} = \frac{C_0 + \mu_0 \rho g H / 2}{\sin \theta_0 \cos \theta_0 + \mu_0 \sin^2 \theta_0} \quad (2.18)$$

In all our calculations, we assume a cohesionless active fault plane and focus on the effects of changing fault zone friction and faulted layer thickness.

### 2.3. Semi-analytic results for fault rotation

#### 2.3.1. Elastic (infinitely strong) faulted layer

The work minimization hypothesis results in a rapid rotation of faults from steep to intermediate angles, which constitutes the lowest energy path for the system (Figure 2-3). The rotation rate (degrees per km of horizontal offset) is fastest immediately after fault initiation and subsequently decreases (Figure 2-4). For example, a fault with a friction coefficient of 0.6 cutting a 10 km-thick elastic layer will rotate from 60° down to 45° over < 5 km of horizontal extension. Further rotation down to 40° occurs over the next ~5 km of extension (Figure 2-4A). Greater density contrasts between the faulted layer and the overlying fluid layer, as well as stiffer elastic moduli lead to faster rotation (Figure 2-5A) down to about 35° after 10 km of extension.

We find that the average fault rotation rate (measured between  $h=0$  and  $h = H/2$ ) scales as the inverse of the faulted layer thickness (Figure 2-4B, “mean” line). Consequently, the total amount of rotation experienced by a fault depends directly on its heave normalized by the thickness of the faulted layer (Figure 2-5). While the exact functional form of this dependence is not fully resolved here, it appears stronger than the sensitivity to the elastic parameters of the layer and to the density contrast with respect to the overlying fluid layer (Figure 2-5A). Due to this effect, faults that cut and flex a 30 km-thick brittle layer will never undergo rotation rates greater than 2° per km of heave, and will therefore retain dips close to their initiation angles over a comparable amount of extension (Figure 2-4). Further, although the friction coefficient assumed for the fault zone sets the initiation angle of the fault, it has very little influence on the total amount of rotation experienced after a given amount of extension (Figure 2-5B). Low-friction faults may therefore reach angles as low as 20–25°, but only because they initiated at a lower angle.

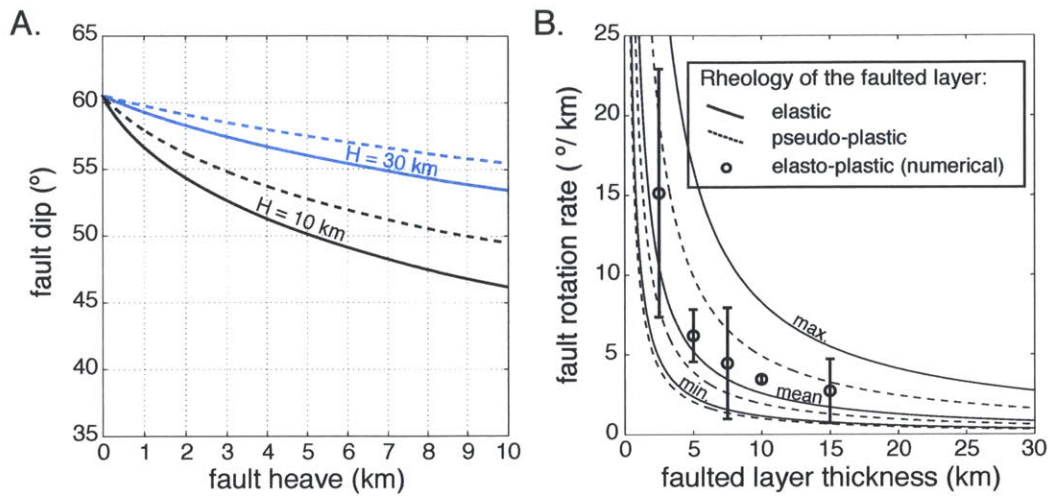


**Figure 2-4. A.** Dip evolution of a normal fault cutting through a 10 km (black) and 30 km (blue) thick faulted layer layer that is either elastic (lines) or pseudo-plastic with  $H_{eff}/H = 0.5$ . **B.** Rate of fault rotation immediately following initiation (maximum), at  $h = H/2$  (minimum) and averaged between these two stages, as calculated in our semi-analytical elastic (lines) and pseudo-plastic model ( $H_{eff}/H = 0.5$ , dashed lines), and measured from our numerical elasto-plastic model (open symbols). For the numerical runs the symbols show the mean rate; error bars indicate maximum and minimum rotation rates.

Fault rotation in response to the accumulation of flexural stresses naturally affects the force balance on the growing normal fault. Allowing faults to rotate towards their optimum dip limits the increase in horizontal tension  $\sigma_R$  that would occur at a fixed dip (Figure 2-6A). In some cases fault rotation ensures that  $\sigma_R$  does not exceed the stress required to break a new fault in intact rock, thereby promoting unlimited fault growth. This effect dominates in thin brittle layers where fault rotation is rapid (Figure 2-6A,  $H=5$  km case). In a thicker layer, fault rotation is slower and stresses accumulate faster, leading to fault abandonment and the creation of a new fault after moderate amounts of extension (Figure 2-6A,  $H=15$  km case). By contrast, when fault rotation is ignored in the force balance calculation for an elastic plate, fault life span increases very slightly with brittle layer thickness [e.g., *Shaw & Lin, 1996*].

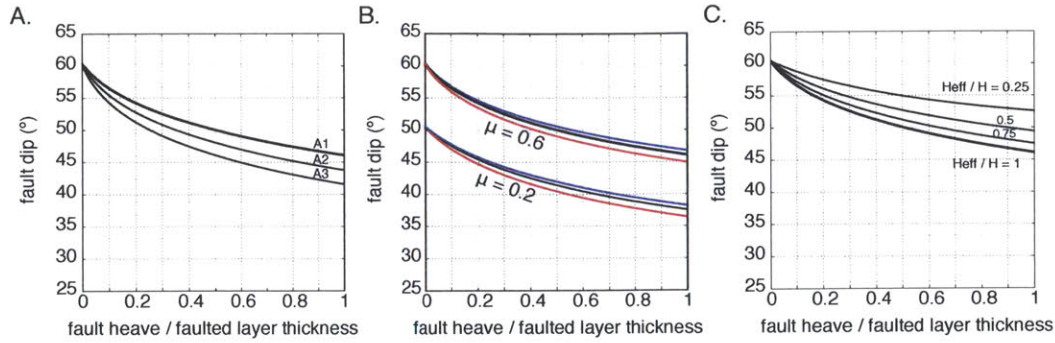


**Figure 2-5.** Evolution of fault dip as a function of accumulated horizontal offset ( $h$ ) normalized by the faulted layer thickness ( $H$ ) calculated from our semi-analytical model. **A.** Effect of changing the stiffness ( $E$ ,  $\nu$ ) and density contrast  $\Delta\rho$  of a 10 km-thick layer. A1: default case,  $E = 30$  GPa,  $\nu = 0.5$ ,  $\Delta\rho = 2300$  kg.m<sup>-3</sup>. A2:  $E = 150$  GPa,  $\nu = 0.25$ ,  $\Delta\rho = 2300$  kg.m<sup>-3</sup>. A3:  $E = 150$  GPa,  $\nu = 0.25$ ,  $\Delta\rho = 2700$  kg.m<sup>-3</sup>. **B.** Effect of changing fault friction with parameters from case A1. The blue, black and red curves correspond to  $H = 15$ , 10, and 5 km respectively. **C.** Effect of pseudo-plasticity in a 10 km-thick layer with parameters from case A1. The ratio  $H_{eff}/H$  is indicated next to each curve.

### 2.3.2. Elastic / pseudo-plastic faulted layer

So far we have only considered a purely elastic faulted layer in which tensional stresses can accumulate without limitation. A more realistic description of the lithosphere must involve a finite yield strength that acts as a maximum allowable stress and promotes diffuse plasticity that locally weakens the layer at large stress / strains. Below we incorporate this mechanism into our semi-analytical model in a highly simplified manner to qualitatively estimate its effect on fault rotation and life span.

We incorporate (pseudo-) plasticity by replacing the true faulted layer thickness  $H$  by a lower effective elastic thickness  $H_{eff} \leq H$  in all the terms related to  $W_{INT}$ . We use  $H_{eff}$  in Equations (2.10) and (2.13) to define an effective flexural rigidity  $D_{eff}$  and an effective flexural wavelength  $\alpha_{eff}$ . These parameters act as a crude measure of the amount of distributed plastic deformation that effectively weakens the faulted layer. In reality  $H_{eff}$  is spatially variable and a direct function of plate curvature and the assumed yield-strength envelope [Buck, 1988].  $H_{eff}$  will be smallest in the regions of highest curvature because these regions represent the areas that have accumulated the greatest flexural stresses.



**Figure 2-6.** Horizontal tension needed to sustain slip on a growing normal fault calculated as a function of accumulated heave, for various faulted layer thicknesses  $H$ , from our semi-analytical model of fault growth in a thin, elastic / pseudo-plastic layer. The multicolored curves correspond to cases where fault rotation is allowed to minimize the regional horizontal stress. Colors indicate the evolving fault dip. For comparison, dark red curves show stress increase in cases where fault rotation is not allowed and dip is held constant at  $60^\circ$ . The stars mark the amount of horizontal extension that can be accommodated before it becomes easier to break a new fault in intact lithosphere (requiring a stress shown as horizontal dashed lines) than to sustain slip on the active fault. The infinity symbols indicate cases where faults can grow indefinitely. **A.** Elastic faulted layers. **B.** Pseudo-plastic layers without rotation. The ratio  $H_{eff} / H$  is indicated next to each curve. **C.** Pseudo-plastic layers with rotation.

In low-curvature regions,  $H_{eff}$  likely retains a value close to  $H$ . In our simplified approach, we use a single  $H_{eff}$  value for the entire faulted layer, which represents an average effective thickness over a distance roughly equivalent to the (reduced) flexural wavelength of the plate. This approach clearly overestimates the amount of weakening due to plasticity, but it enables us to illustrate the first-order effects with the least amount of additional parameters.

The main effect of pseudo-plasticity is to slow down fault rotation with respect to the elastic case. In a 10 km-thick faulted layer with an effective elastic thickness of 5 km, a fault will only rotate down to  $\sim 50^\circ$  after 4 km of extension, as opposed to  $\sim 45^\circ$  in the purely elastic end-member (Figure 2-4A). For a given value of  $H$ , reducing the ratio  $H_{eff} / H$  leads to even slower rotation. This effect appears to hold over the entire range of  $H$  (Figure 2-4B). For a given  $H_{eff} / H$ , rotation rates in a pseudo-plastic faulted layer scale as the inverse of the true layer thickness, which is the same as in the elastic end-member case.

Figure 2-6B and 2-6C illustrate the effect of pseudo-plasticity on fault life span. In cases where faults are not allowed to rotate, a lower  $H_{eff} / H$  promotes longer fault life span by limiting the buildup of tensional stresses. Interestingly, for a given  $H_{eff} / H$ , fault life span appears almost insensitive to the true faulted layer thickness  $H$ . However, due to complex feedbacks between inelastic deformation and plate curvature, plastic weakening tends to be stronger in thinner (true thickness  $H$ ) plates. In other words,  $H_{eff} / H$  will

achieve lower values in plates that have a smaller initial  $H$  [e.g., *Buck*, 1988]. This effect is likely responsible for the classic prediction of longer fault life span in thinner faulted layers [*Buck*, 1993; *Lavier et al.*, 2000; *Lavier and Buck*, 2002; *Behn & Ito*, 2008]. In cases where faults are allowed to rotate (Figure 2-6C), pseudo-plasticity complements the effect of rotation in promoting even longer fault life span in thinner layers.

Our semi-analytical approach makes important predictions for dip evolution and fault life span. It is, however, limited by underlying assumptions that include: (1) the thin plate approximation for calculating  $W_{INT}$ , (2) a simplified treatment of plasticity, and (3) the hypothesis that rotation acts to minimize the increase in  $W_{EXT}$ . Therefore, to test validity of this approach, we compare our semi-analytical results with more complex numerical simulations of normal fault growth based solely on conservation of mass and momentum, which do not incorporate any of the assumptions made thus far.

#### **2.4. Numerical models of fault rotation in an elasto-plastic layer**

In this section, we compare our semi-analytical elastic results with numerical simulations of fault growth in an elasto-plastic brittle layer. We solve for conservation of mass and momentum in a 2D domain using the finite difference / particle-in-cell technique [*Harlow and Welch*, 1965] described by *Gerya* [2010]. Our model setup (Figure 2-7) involves a brittle layer of thickness  $H$ , viscosity  $\eta_L = 10^{24}$  Pa·s, Young's modulus  $E = 30$  GPa, and Poisson's ratio  $\nu = 0.5$ . The brittle layer is situated between a low-viscosity asthenosphere ( $\eta_A = 10^{18}$  Pa·s) below and a low-viscosity "sticky ocean" layer ( $\eta_S = 10^{17}$  Pa·s) [*Crameri et al.*, 2012] above. The asthenosphere and ocean layers have thicknesses similar to that of the brittle layer. The ocean layer has a density of  $1000 \text{ kg}\cdot\text{m}^{-3}$ ; the brittle and asthenospheric layers have densities of  $3300 \text{ kg}\cdot\text{m}^{-3}$ . To insure that flexure is not influenced by the model boundaries, the width of the box is set to 3 times the (elastic) flexural wavelength of the brittle layer (Equation 2.13). The height of the box is equal to 50% of its width. We pull on each side of the model domain at a half-rate,  $U$ , and compensate the horizontal outflow of ocean and rock by imposing a matching inflow of material through the top and bottom boundaries, respectively. Shear tractions are set to zero on all boundaries.

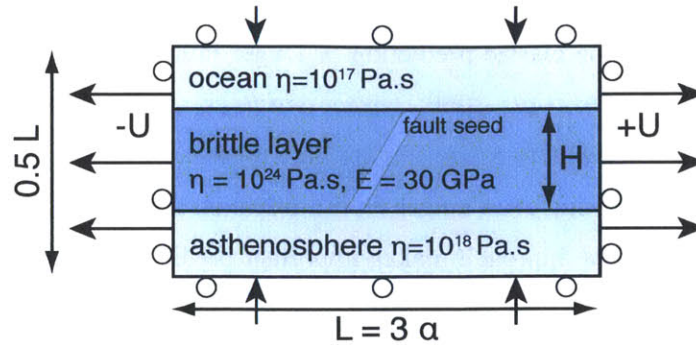


**Figure 2-7.** Schematic setup of our numerical models for fault evolution in an elasto-plastic layer. The faulted layer is forced to be effectively elastic by setting the viscosity to be sufficiently large that the Maxwell timescale greatly exceeds the numerical time step chosen to integrate elastic stresses. Plasticity is implemented following a Mohr-Coulomb criterion. The fault is seeded at the first time iteration as a thin band of low-cohesion material dipping at the optimal initiation angle (Equation 2.16), and then allowed to evolve freely as strain localizes on this narrow shear band. See text for details.

The brittle layer behaves as an elastic-plastic solid while the other layers are effectively viscous. Elasticity is implemented following *Moresi et al.* [2003]. We impose a Maxwell visco-elastic rheology law in which the time-derivative of the stress tensor is discretized with a backward finite difference scheme. This allows us to rewrite the rheological law as a simple viscous law with an effective viscosity that incorporates the elastic moduli and the time step chosen for the stress approximation (termed “computational time step” in *Gerya* [2010]). The terms related to the stresses from the previous iteration then appear in the discretized momentum conservation equation. The computational time step is chosen such that the effective viscosity vanishes in the high-viscosity ( $\eta_l$ ) brittle layer, allowing the terms related to past stresses to dominate the momentum equation rendering the layer effectively elastic.

Plastic failure follows the Mohr-Coulomb criterion (Equation 2.5) with a friction coefficient of 0.6. Strain localization is promoted by decreasing the cohesion (initially  $C_0 = 100$  MPa) linearly with the accumulated plastic strain [*Lavier et al.*, 2000]. The cohesion in intact material is  $C_0 = 100$  MPa. We chose such a high value to promote

longer fault life span ( $\sigma_R^{BREAK}$  is high), allowing us to follow the growth of a single fault over longer time scales before a new fault breaks, while still promoting diffuse plastic yielding in the footwall and hanging wall. Once a critical plastic strain corresponding to 250 m of fault offset is exceeded, cohesion is kept at a minimum value of 0.01 MPa. To initialize strain localization on a single normal fault at the beginning of each model run, we impose a rectangular “fault seed” of dip  $\theta_0$  (Equation 2.16) and width equal to 3 cell diagonals in the middle of the model domain. In this narrow region, plastic strain is set to the critical value and the cohesion is decreased accordingly. The grid resolution close to the fault is refined to about  $500 \times 500$  m or less, which enables a mature fault width that is typically less than 2 km. A “healing” mechanism is implemented in the code to promote strain localization [Lavier *et al.*, 2000]. This consists in reducing the accumulated plastic strain by a small amount at every time iteration. In regions of diffuse plastic yielding the accumulated strain and associated weakening heals within  $\sim 10,000$  years, but keeps building up in regions of localized deformation (i.e., shear zones). Once all the extensional strain has effectively localized on the fault (which usually takes less than 4 time iterations), we measure the average fault dip as a function of fault heave by visually fitting a line to the region of greatest accumulated plastic strain. Fault heave is estimated as the horizontal distance between the bottom of the hanging wall trough and the top of the footwall shoulder.

We ran 5 simulations spanning brittle layer thicknesses of  $H = 2.5$  to 15 km. In each simulation the fault rotated rapidly from its prescribed initiation angle ( $60^\circ$ ) down to angles as low as  $35^\circ$  at rates comparable to those inferred from the simple work minimization models (Figure 2-8, 2-9). Flexural stresses build up in the footwall and hanging wall, and quickly saturate at the yield stress (Figure 2-8B) resulting in diffuse yielding within about half a flexural wavelength from the fault. We fit the dip versus heave curves measured in each simulation between  $h=0$  and  $h=H/2$  with a second-order polynomial, and measured the average slope of the polynomial to determine a smooth estimate of the mean rotation rate (Figure 2-4B). Our measurements are consistent with a rotation rate that is inversely proportional to faulted layer thickness as in the simple elastic and pseudo-plastic model. In general, our numerically determined rotation rates tend to plot between

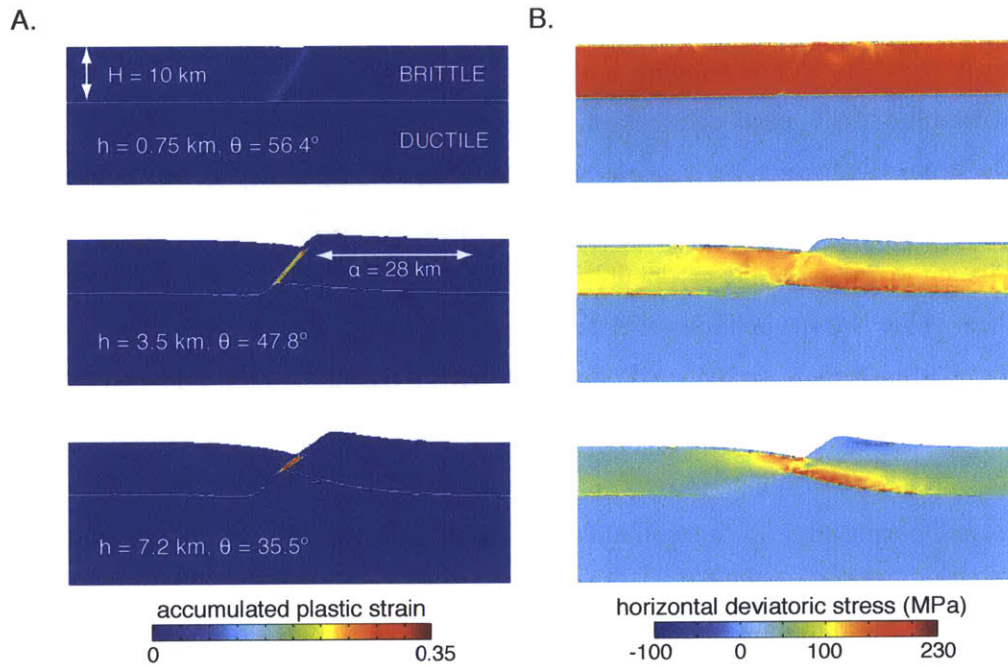


**Figure 2-8.** Snapshots of **A.** accumulated plastic strain and **B.** horizontal deviatoric stress ( $\sigma_{xx}$ ) for various amounts of extension in numerical models of fault growth in a 10 km thick elasto-plastic layer. Strain is highly localized into a < 2 km wide shear zone that represents the fault. The white line marks the brittle-ductile transition (base of the faulted layer).

the average rotation rates predicted for an infinitely strong layer and a pseudo-plastic layer with  $H_{eff}/H = 0.5$ .

## 2.5. Discussion

### 2.5.1 Work minimization and dip evolution

The models presented in this study illustrate that normal faults rotate in response to the flexure they induce in the surrounding elastic or elasto-plastic brittle layer. Complex numerical simulations yield results that are consistent with the assumption that the system evolves along the lowest possible energy path (Figure 2-3). Consider a fault undergoing a

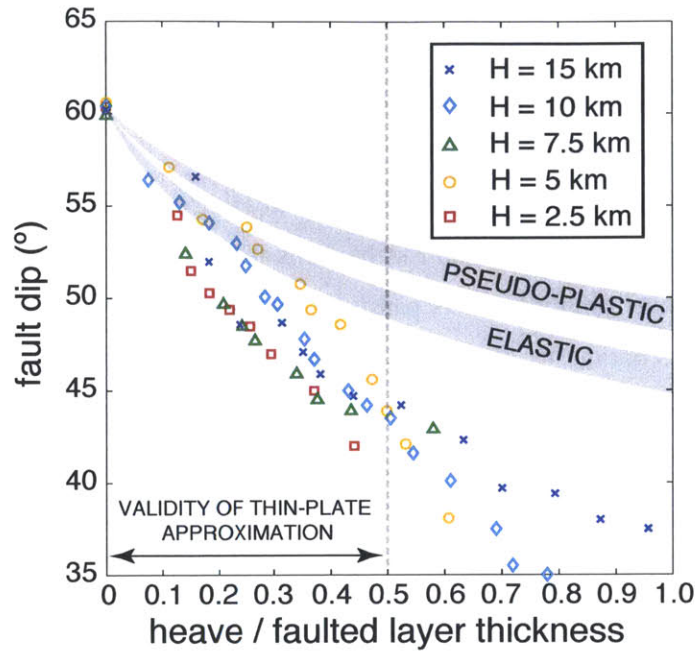


**Figure 2-9.** Dip evolution of a normal fault cutting through elastic, pseudo-plastic ( $H_{eff}/H = 0.5$ ), and elasto-plastic (colored symbols) brittle layers of varying thickness  $H$  between 15 and 5 km (the gray area represents the corresponding range of dips).

finite amount of horizontal extension  $\Delta h$ . The associated uplift and subsidence of the footwall and hanging wall will result in (a) accumulation of bending stresses and (b) a moment imbalance that promotes the rotation of the fault toward shallower angles. Growing the fault by  $\Delta h$  while allowing it to rotate by an angle  $\Delta\theta$  will result in a smaller increase in fault throw than if the fault were to retain its initial dip. Smaller fault throw means less topographic load on the footwall and hanging wall blocks, and therefore a smaller increase in bending work  $W_{INT}$  that must be overcome by an increase in the external work  $W_{EXT}$ . Rotating the fault by too large an amount, however, will increase the work done by frictional resistance  $W_{FRIC}$ , which must also be overcome by  $W_{EXT}$ . Therefore, we argue that  $\Delta\theta$  adopts the value that optimally balances these two effects. From Equation (2.17) we can see that minimizing the increase in  $W_{EXT}$  is equivalent to minimizing the tensional stress  $\sigma_R$ , or the tensional force  $F_R = H\sigma_R$  required to sustain slip on the fault [e.g., Forsyth, 1992; Buck, 1993]. The first component of  $W_{EXT}$  (first term

in Equation 2.14) corresponds to the frictional resistance of the fault, and is lowest when  $\theta = \theta_0$  immediately after fault initiation ( $h=0^+$ ). The second component, initially zero (second term in Equation 2.14), corresponds to the work done bending the faulted layer and is a growing function of  $\theta$  (Appendix 2.2). The effect of this term is to shift the minimum in  $F_R$  toward smaller dip angles with increasing extension (Figure 2-3).

We envision several physical mechanisms that can lead to rotation of the active fault plane. The most obvious one is passive advection of the fault in the displacement field induced by continuous flexural readjustment of the footwall and hanging-wall blocks. It is unclear, however, whether this effect alone can explain the magnitude and kinetics of rotation observed in our numerical simulations. Another potential mechanism for rotation is that coseismic stress changes during a normal faulting rupture may induce a net torque about a pivot located near the middle of the faulted layer [Dempsey *et al.*; 2012]. In numerical simulations by Dempsey *et al.* [2012], this torque led to finite rotation of the active fault plane over many seismic cycles at rates comparable to those found in this study. In our models we consider continuous slip on a weak fault as opposed to coseismic and interseismic phases. However, it is possible that a similar mechanism may be at play in our simulations, which can be regarded as an extremely slow “coseismic” deformation phase. A third potential mechanism for rotation involves continuous strain relocalization at progressively shallower angles within the narrow weak zone that surrounds a fault in our numerical models. In the Earth, this weak zone could correspond to damage areas that tend to form in the vicinity of faults [e.g., Collettini 2011]. Strain relocalization could be driven by stress rotation due to bending of the footwall and hanging-wall. We note that bending of the faulted layer is central to all the mechanisms discussed above, either in terms of displacement field or stress buildup.

We have found that the thickness of the faulted layer,  $H$ , exerts the strongest control on the kinematics of flexure-induced fault rotation. This is likely due to the fact that  $W_{FRIC}$  scales more strongly with  $H$  ( $\sim H^2$ ) than does  $W_{INT}$  ( $\sim H^{3/2}$  if  $h$  is small). We can therefore conclude that in thin layers (small  $H$ ) the relative increase in  $W_{EXT}$  ( $= W_{INT} + W_{FRIC}$ ) corresponding to an increase in fault heave  $\Delta h$  will be comparatively larger, and more sensitive to a change in fault dip than in thicker layers. In other words,  $W_{EXT}$  will be strongly dependent on the current fault dip if  $H$  is small, leading to a larger  $\Delta\theta$  for a

given  $\Delta h$ . As extension proceeds, topography grows and drives the accumulation of bending stresses. After large amounts of extension, the stress state of the faulted layer is primarily due to the flexure that has already occurred, and becomes less and less sensitive to future changes in fault dip, especially when fault heave becomes comparable to the layer thickness. This effect leads to a progressive decrease in rotation rates that is seen both in the semi-analytical and numerical models (Figures 2-4 and 2-9). The semi-analytical models best predict the results of the numerical simulations when fault heave is lower than half of the faulted layer thickness. This could indicate a limitation of the thin plate approximation when fault heave becomes comparable to plate thickness (Figure 2-9).

### ***2.5.2 Rheologic controls on rotation rate and life span of normal faults***

The rotation rates we measured in the numerical models (with a realistic treatment of plasticity) agree well with those predicted by our semi-analytic work-minimization model. Specifically, they tend to plot between the infinitely strong layer (elastic) end-member and a pseudo-plastic end-member where the effective elastic thickness is decreased to approximately half the true thickness throughout the layer (Figure 2-4B). This is consistent with the fact that only a portion of the faulted layer yields in the numerical simulations. Indeed, non-recoverable deformation accumulates preferentially in a distributed (i.e., non-localized manner) in regions of high plate curvature [Bodine and Watts, 1979; Buck, 1988].

The yield stress of the layer acts as an upper bound on the build-up of bending stresses and limits the increase of  $\sigma_R$  [Buck, 1993]. Less rotation is therefore required to adjust to the flexural stresses, accounting for slower fault rotation in elasto-plastic layers than in purely elastic layers. As fault heave approaches and exceeds  $H$ , the bending stress likely saturates over a large enough region that most of the subsequent deflection occurs through plastic flow. This phenomenon is thought to shape the domal morphology of exposed detachment surfaces by “rollover” [Buck, 1988; Lavier *et al.*, 1999]. If the bending stresses surrounding the fault are fixed at the yield stress, then changes in fault dip will not strongly affect  $\sigma_R$  and the fault will remain stuck at the dip it has reached through past elasto-plastic flexure. The numerical simulations of Choi and Buck [2012]

showed this kind of behavior when fault heave greatly exceeded  $H$ . Namely, they found that when the top of the active fault surface had rotated by  $\sim 20^\circ$  from its initiation angle the fault had reached a near-steady-state geometry. *Choi and Buck* [2012] were also able to resolve depth-dependent rotation of the fault zone, with little to no rotation occurring at the base of the fault. Our semi-analytical model averages the lithostatic stress along a planar fault zone, and thus cannot account for depth-dependent rotation. However, if one replaces  $H/2$  by depth along the fault in the derivation of the semi-analytical model, one would indeed expect faster fault rotation at shallower depths and the development of concave-down faults at very large offsets.

Fault rotation acts in the same manner as plasticity in limiting the increase in bending stresses during fault growth. *Buck* [1993] quantified the effect of plasticity alone and showed that the maximum flexural stress in an elasto-plastic layer scales linearly with  $H$ . Specifically, he showed that a fault will grow indefinitely while retaining its dip if the layer is thin enough that  $\sigma_R$  saturates at a value smaller than the stress needed to break a new fault (Equation 2.18). *Lavier and Buck* [2002] showed that rift zones dominated by long-lived normal faults (e.g., oceanic detachments or metamorphic core complexes) are generally associated with thinner lithosphere than rifts dominated by shorter-lived “half-graben” style faults. Incorporating our mechanism for fault rotation yields a similar prediction to that of a normal fault with constant dip in an extending elasto-plastic layer, namely, in both cases infinite fault growth is permitted in thin enough lithosphere. However, the additional influence of fault rotation will allow sustained slip on normal faults formed in thicker lithosphere than would be permitted if fault dip remained fixed at high angle. This is consistent with previous numerical simulations of fault development at mid-ocean ridges by *Behn and Ito* [2008], who found that a force balance model could only predict fault life span in an elasto-plastic lithosphere if it incorporated the reduction in fault dip observed in their numerical simulations. This suggests that both the finite yield strength of the lithosphere and the flexural rotation mechanism presented here are important components to the physics of normal fault growth.

The brittle-ductile transition (BDT), which controls the thickness of the layer affected by faulting, is largely thermally controlled, and has been inferred to correspond

to temperatures of 400–600°C in the oceanic and upper continental crust [e.g., *Hirth et al.*, 1998]. The depth, geometry, and evolution of the BDT results from a competition between heat advection in the solid flow field (underlying ductile flow, overlying brittle deformation and associated uplift / subsidence) and heat conduction, which can be enhanced by hydrothermal processes [*Phipps Morgan and Chen*, 1993; *Lavier and Buck*, 2002]. For simplicity, the numerical simulations presented here do not account for temperature evolution and temperature-dependent rheology. Consequently, the distribution of brittle and ductile materials is solely controlled by advection in the fault-related velocity field. This corresponds to an end-member scenario in which heat conduction and hydrothermal circulation are inefficient at extracting heat from the base of the faulted layer, resulting in a sharp BDT that is offset by the fault. In this scenario the area of contact between the hanging-wall and footwall blocks and the thickness of the rock column overlying the fault decreases with increasing fault offset (Figure 2-10A). Alternatively, if hydrothermal cooling is efficient at extracting heat from the lithosphere the BDT may remain relatively flat and not mimic the surface topography [e.g., *Lavier and Buck*, 2002], which will in turn result in a smaller reduction in the area of contact during extension.

To investigate whether such changes in the morphology of the BDT will influence the kinematics of fault rotation, we ran numerical simulations of fault growth in elasto-plastic lithosphere with a BDT that was forced to remain flat and at a fixed depth (Figure 2-10B). These runs yielded very similar rotation kinematics to the reference runs presented in Figure 2-9. The reason for this is twofold. First, bending of the brittle layer affects an area over which the layer thickness is largely unchanged (over a flexural wavelength  $\alpha$ ), but that is much larger than the zone immediately affected by the fault, making flexural rotation relatively insensitive to a net decrease in layer thickness close to the fault. Second, our model assumes the same density for the faulted layer and the underlying ductile asthenosphere. This means that gravitational deflection of the lithosphere is solely controlled by the density contrast at the surface / seafloor, and is insensitive to the geometry of the BDT. Introducing a buoyancy contrast along the BDT could introduce a restoring load that limits deflection and introduces asymmetry between

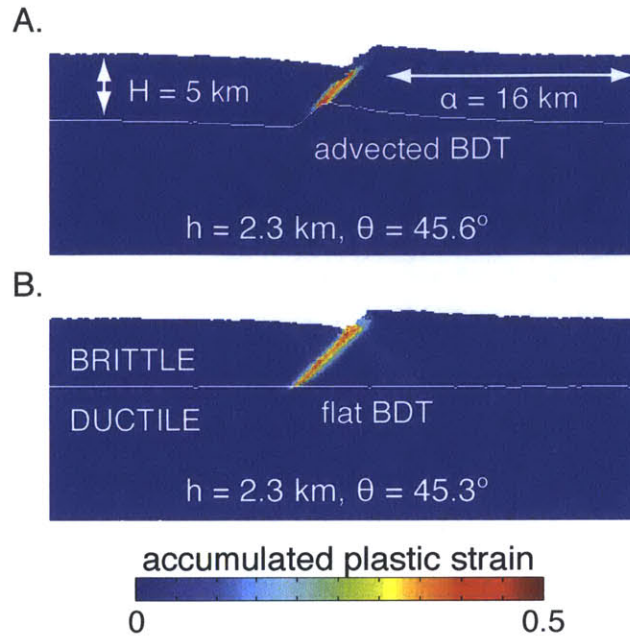


**Figure 2-10.** Snapshots of accumulated plastic strain after 2.3 km of horizontal extension along a fault cutting through a 5 km-thick elasto-plastic layer. In **A**, the brittle-ductile transition (BDT, white line) is advected in the ambient solid flow field and therefore offset by the fault. In **B**, the BDT is constrained to remain at a fixed depth, representing a scenario where heat is efficiently extracted through the brittle layer. Evolution of the BDT does not appear to strongly control the rotation kinematics of the fault.

the footwall and hanging wall [Weissel and Karner, 1989], potentially affecting fault rotation.

It is generally thought that fault zones progressively weaken as they accumulate offset, due to effects such as progressive damage and/or precipitation of soft minerals. In our models the fault is systematically treated as a zone of very low cohesion ( $\ll 1$  MPa). The choice of a low fault zone cohesion,  $C$ , has little effect on the evolution of  $\sigma_R$ , given that  $C \ll \mu\rho gH/2$  in the expression of  $W_{FRIC}$  (Equation 2.7). By contrast, cohesion of the unfaulted brittle material is critical in controlling when a new fault breaks and the previous fault is abandoned (Equation 2.18). Fault friction, however, has a very strong control on the initiation angle of normal faults (Equation 2.16). To estimate the extent to which the friction coefficient influences fault rotation, we calculated the dip evolution of

low-friction faults using our semi-analytical model. We found that fault friction had very little influence on rotation rates (Figure 2-5B). This is consistent with our interpretation of rotation kinematics being controlled primarily by flexural processes. Fault friction does, however, control the range of angles that an active fault will reach because it controls the angle of fault initiation. If flexure of the brittle layer can account for  $\sim 30^\circ$  of fault rotation over a total extension of  $\sim H$ , then a low-friction fault may reach angles as low as  $20^\circ$  if it initiated at  $50^\circ$  ( $\mu = 0.2$ ). An important consequence of this result is that a seismically-active normal fault dipping at an angle of  $40^\circ$  could either be a strong ( $\mu = 0.6$ ) fault that has accommodated a significant amount of extension ( $\sim 30\%$  of the faulted layer thickness), or a weak ( $\mu < 0.3$ ), young normal fault that has accommodated little offset (Figure 2-5B). While the distinction may be straightforward in the field, it is not at all obvious when one only considers catalogs of normal faulting earthquakes.

### ***2.5.3 Implications for extensional rift systems***

We propose that the dip distribution of normal faulting earthquakes (Figure 2-1) observed both globally and at individual rifts reflects a ubiquitous process of faults initiating at a steep angle ( $\sim 60^\circ$ ) before rapidly rotating toward shallower dips and being abandoned in favor of a new steep fault. In the framework of our model, the  $30\text{--}60^\circ$  range is a reflection of the typical brittle layer thickness ( $\leq \sim 15$  km) inferred in most extensional settings [e.g., *Chen and Molnar, 1983*]. Indeed, a 15 km brittle layer is thin enough to allow large amounts of rotation over the life span of the fault (Figure 2-6). If fault segments evolve in relative independence along the axis of a rift, then our model predicts that intermediate to shallow-dipping faults should be more prevalent than steep faults, consistent with the high-angle tail in the global distribution (Figure 2-1). Of course the extent to which the dip evolution of a single normal fault (Figure 2-5) is reflected in the shape of the global earthquake dip distribution is not straightforward. It depends on (1) the distribution of heaves within a fault population, which reflects the relative timing of fault growth (e.g., sequential vs. simultaneous) as well as the degree of along-axis fault interaction; and (2) how earthquakes sample the true dip distribution. Indeed, *Wernicke [1995]* suggested that low-angle fault planes may be characterized by longer earthquake

recurrence time and therefore be undersampled in global dip catalogs, thereby explaining the low-angle tail and bell-shape of the distribution shown in Figure 2-1.

Our model makes predictions for fault evolution, which can be tested with detailed regional studies of fault geometry and lithospheric rheology. For instance, our model predicts that strong faults ( $\mu > 0.6$ ), which initiate at a steep angle in a thick brittle layer ( $H > 25$  km), will only remain active over a few kilometers of extension before they are abandoned in favor of a new fault. Over their short life span, these faults will not experience large rotations from their initiation angle. This is consistent with the steepest-dipping normal faulting ruptures recorded in Mozambique [51–76° during the 2006 seismic sequence; *Yang and Chen, 2008*] where the seismogenic layer thickness (~30 km) is notably thicker than is typical in most continental rifts [*Chen and Molnar, 1983*]. Our model suggests that similar steep (slowly rotating) faults should be prevalent in regions of high brittle layer thickness such as the Baikal Rift in central Asia [e.g., *Watts and Burov, 2003*]. Unfortunately there is not a sufficiently complete record of normal faulting tensor solutions in which the fault plane can be clearly identified to accurately sample the dip distribution in such settings. Future studies should focus on assembling such detailed catalogs on the regional scale in order to systematically constrain fault dip as a function of lithospheric thickness (e.g., seismogenic layer thickness, equivalent elastic thickness, thermal models). As a first step in this direction, we compiled representative heat flow measurements for each region present in the global dip distribution shown in Figure 2-1, using data from the global heat flow dataset [*Pollack et al., 1993*] and the compilation used in *Lavier and Buck [2002]*. We treat conductive heat flow as a proxy for brittle layer thickness, with the expectation of greater heat flow in regions of thinner lithosphere. Figure 2-11 shows event dip plotted against regional heat flow. Events from Mozambique and the Baikal Rift plot at the high-dip / low heat flow end. Events from the Woodlark Basin, which are to date the shallowest-dipping normal faulting ruptures on record, plot on the high heat flux end, which is consistent with our results. Specifically, we expect that the lowest dip that a normal fault can reach should be smaller in thinner faulted layers. If this is the case, thorough regional compilations of unambiguous fault dips may help outline a minimum dip “envelope” on a plot of dip vs. heat flow (or another proxy for  $H$ ).

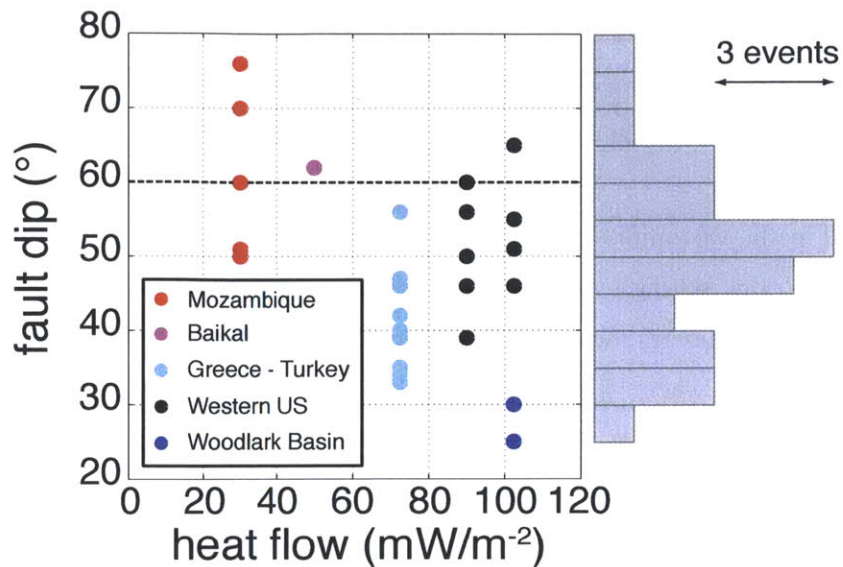


**Figure 2-11.** Compilation of normal fault dips making up the distribution shown in Figure 2-1 plotted against regional heat flow data [Pollack *et al.* 1993; Lavier and Buck 2002]. Heat flow serves as a proxy for faulted layer thickness, with higher heat flow expected in regions of thinner brittle layers. The global distribution of fault dips is reported on the right side of the graph.

Another obvious step in testing the predictions of fault rotation made here are through detailed geologic studies using paleomagnetism, thermobarometry, and/or synkinematic sediment sequences to reconstruct the rotational and growth history of normal fault systems. In practice comparing model predictions of dip versus heave with individual real-world faults is very challenging. This is mainly because measuring the total amount of extension accommodated by a fault is not straightforward, especially if surface processes alter or erase the geomorphological markers of finite extension (e.g., erosion of the uplifting footwall).

An additional complication is that surface processes may influence the force balance on a growing normal fault, either by adding load (deposition of sediments on the subsiding hanging wall), and/or by removing / redistributing load through footwall erosion, which would feed back onto the topographic and bending stresses. In the numerical models of Choi and Buck [2012], incorporating basin infill on the hanging wall

side of a growing fault indeed results in faster and overall greater amounts of fault rotation. Quantifying the effect of such processes on the build-up of flexural stresses and the subsequent readjustment of normal faults is beyond the scope of this study, but would constitute an interesting next step with potential implications for tectono-climatic interactions.

Finally, we emphasize that the models presented here are generally well suited for mid-ocean ridge settings. We have considered an end-member of rifting where a single normal fault dominates the strain field, which is often the case at asymmetric mid-ocean ridge segments where long-lived detachments accommodate most of the tectonic extension [Escartin *et al.*, 2008]. Our model predicts that very large offset ( $h > H$ ) detachment faults displaying flat, domal footwalls should dip at a relatively shallow angle ( $<45^\circ$ ) where they root at the ridge axis. The subsurface geometry of oceanic detachments is still a matter of debate, and to date the only direct constraint is from a single microseismicity study at the TAG segment of the Mid-Atlantic Ridge [DeMartin *et al.*, 2007]. Their study argues for a shallow dipping exhumed fault surface that roots into a steep ( $\sim 70^\circ$ ) active fault. In the conceptual framework of our model this would only be possible in an extremely weak elasto-plastic lithosphere, where rollover of the footwall occurs through widespread plastic flow and there is limited stress build-up to drive significant rotation of the active fault. Another possibility is that fault rotation is strongly depth-dependent and leads to a concave-down fault that retained a steep dip at depth while its upper portion rotated by  $20^\circ$  or more.

It is noteworthy, however, that TAG does not feature a fully formed, corrugated oceanic core-complex and has only accommodated about 4 km of horizontal extension between termination and breakaway. It is also unclear whether the steep cluster of seismicity observed at the axis is actually linked to the exhumed fault surface or whether it constitutes the initiation of a new fault at a high angle that marks the recent abandonment of the older TAG fault.

Additional studies of detachment microseismicity are needed to resolve the debate on active detachment roots, which has strong implications on the total amount of rotation recorded by exhumed lower-crustal units in the footwall of oceanic core complexes. We propose that footwall rotation recorded by paleomagnetic tracers [e.g., Garcés and Gee,

2007; *McLeod et al.*, 2011] may record both rollover of the exhumed footwall [*Buck*, 1988; *Lavier et al.*, 1999] and rotation of the active fault plane explored in this study. While these two components may be of similar magnitude, we expect rotation of the active fault plane to occur immediately after fault initiation, and therefore to be recorded in units closest to the detachment breakaway.

## **2.6. Conclusions**

We have shown that fault rotation in response to the evolving stress field associated with plate flexure provides a mechanism to explain the distribution of active normal fault dips observed globally and at the scale of individual rift systems. In our model, the fastest rotation rates occur immediately following fault initiation, and the average rotation rates scale as the inverse of the faulted layer thickness. Predicted fault dips span the entire 30–60° dip range documented in earthquake catalogs, except in cases where the faulted layer is > 25 km, in which case it rapidly becomes easier to initiate a new fault than to continue extension and rotation of the active fault. The predictions of our model can be tested through careful regional compilations of normal faulting mechanisms where one of the two nodal planes can be clearly identified as the rupture plane. Such compilations should be complemented by independent estimates of the thickness of the faulted layer and more generally of the local strength profile of the lithosphere. Fault-induced flexure and topographic stresses are essential controls on fault dip, which must be considered alongside fault strength and faulted layer strength. Finally, the sensitivity of topographic and bending stresses to surface processes (e.g., erosion and deposition) opens a range of implications for the long-term evolution and short-term seismogenic behavior of normal fault systems.

### Appendix 2.1. Calculation of the bending work term $W_{INT}$

To estimate the mechanical work required to bend the faulted layer,  $W_{INT}$ , from Equation (2.9) we first calculate the deflection of the faulted layer  $w(x)$  due to finite extension on the fault. This is done by convolving the right-hand side of Equation (2.9) with the Green's function describing the response of an infinite elastic thin plate to a point load:

$$w(x) = \int_{-\infty}^{+\infty} G(x,s)(-\Delta\rho gw^*(s)) ds \quad (2.S1)$$

where  $G(x,s)$  is written

$$G(x,s) = \frac{\alpha^3}{8D} \exp\left(-\left|\frac{x-s}{\alpha}\right|\right) \left( \cos\left|\frac{x-s}{\alpha}\right| + \sin\left|\frac{x-s}{\alpha}\right| \right) \quad (2.S2)$$

and  $w^*(x)$  is defined as

$$w^*(x) = \begin{cases} -\frac{h}{2} \tan\theta, & \forall x < -\frac{h}{2} \\ x \tan\theta, & \forall x \in \left[-\frac{h}{2}, \frac{h}{2}\right] \\ +\frac{h}{2} \tan\theta, & \forall x > +\frac{h}{2} \end{cases} \quad (2.S3)$$

This yields the total fault-induced topography  $w^T(x) = w(x) + w^*(x)$

$$w^T(x) = \frac{1}{4} \alpha \tan\theta \left( f\left(\left|\frac{x-h/2}{\alpha}\right|\right) - f\left(\left|\frac{x+h/2}{\alpha}\right|\right) \right) \quad (2.S4)$$

where  $f(x)$  is a dimensionless function defined as

$$f(x) = \exp(-x)(\sin x - \cos x) \quad (2.S5)$$

From Equation (2.9), we can now write

$$W_{INT} = \frac{D}{16\alpha^2} \tan^2 \theta \int_0^{+\infty} \left( f''\left(\left|\frac{x-h/2}{\alpha}\right|\right) - f''\left(\left|\frac{x+h/2}{\alpha}\right|\right) \right)^2 dx \quad (2.S6)$$

which can also be expressed as

$$W_{INT} = \frac{D}{16\alpha} \tan^2 \theta \Psi\left(\frac{h}{\alpha}\right) \quad (2.S7)$$

Where  $\Psi(y)$  is related to  $f(x)$  by

$$\Psi(y) = \int_0^{+\infty} \left( f''\left(x - \frac{1}{2}y\right) - f''\left(x + \frac{1}{2}y\right) \right)^2 dx \quad (2.S8)$$

The function  $\Psi(y)$  is estimated numerically with the trapezoidal method. Its graphical representation is shown in Figure 2-S1A.

## Appendix 2.2. Equations for fault dip, work and stress as a function of heave

Each term in Equation (2.14),  $W_{FRIC}$  and  $W_{INT}$ , can be written as the product of a function of dip,  $A(\theta)$ , and a function of heave,  $R(h)$ . Specifically,

$$A_F(\theta) = \frac{1}{\sin \theta \cos \theta + \mu \sin^2 \theta} \quad (2.S9)$$

$$R_F(h) = (C + \mu \rho g H / 2) H h \quad (2.S10)$$

$$A_I(\theta) = \tan^2 \theta \quad (2.S11)$$

$$R_I(h) = \frac{D}{16\alpha} \Psi\left(\frac{h}{\alpha}\right) \quad (2.S12)$$

To determine the fault dip that minimizes the increase in total extensional work ( $W_{EXT}$ ) with increasing extension, we differentiate  $W_{EXT}$  with respect to  $h$  and  $\theta$ .

$$\frac{\partial}{\partial \theta} \left( \frac{\partial W_{EXT}}{\partial h} \right) = (A_F''(\theta) R_F(h) + A_F'(\theta) R_F'(h)) \frac{\partial \theta}{\partial h} + A_F'(\theta) R_F'(h) + A_I'(\theta) R_I'(h) \quad (2.S13)$$

and this equal to zero to obtain the following nonlinear ODE:

$$\frac{\partial \theta}{\partial h} = - \frac{A_F'(\theta) R_F'(h) + A_I'(\theta) R_I'(h)}{A_F''(\theta) R_F(h) + A_I''(\theta) R_I(h)} \quad (2.S14)$$

Equation (2.S14) is solved with a 4<sup>th</sup> order Runge-Kutta method with the initial condition  $\theta(h=0) = \theta_0$ . Below are the expressions of the first and second order derivatives of functions  $A$  and  $R$ .

$$A_F'(\theta) = - \frac{\csc^4 \theta (\cos 2\theta + \mu \sin 2\theta)}{(\mu + \cot \theta)^2} \quad (2.S15)$$

$$A_F''(\theta) = \frac{2 \csc^2 \theta}{(\mu + \cot \theta)^3} (1 + \mu^2 + 3\mu^2 \cot^2 \theta + 3\mu \cot^3 \theta - \mu \cot \theta + \cot^4 \theta) \quad (2.S16)$$

$$A_I'(\theta) = 2 \tan \theta \sec^2 \theta \quad (2.S17)$$

$$A_I''(\theta) = -2(\cos 2\theta - 2)\sec^4 \theta \quad (2.S18)$$

$$R_F'(h) = (C + \mu \rho g H / 2) H \quad (2.S19)$$

$$R_I'(h) = \frac{D}{16\alpha^2} \Psi' \left( \frac{h}{\alpha} \right) \quad (2.S20)$$

The graphical representation of  $\Psi'(x)$  (estimated numerically) is shown in Figure 2-S1B.

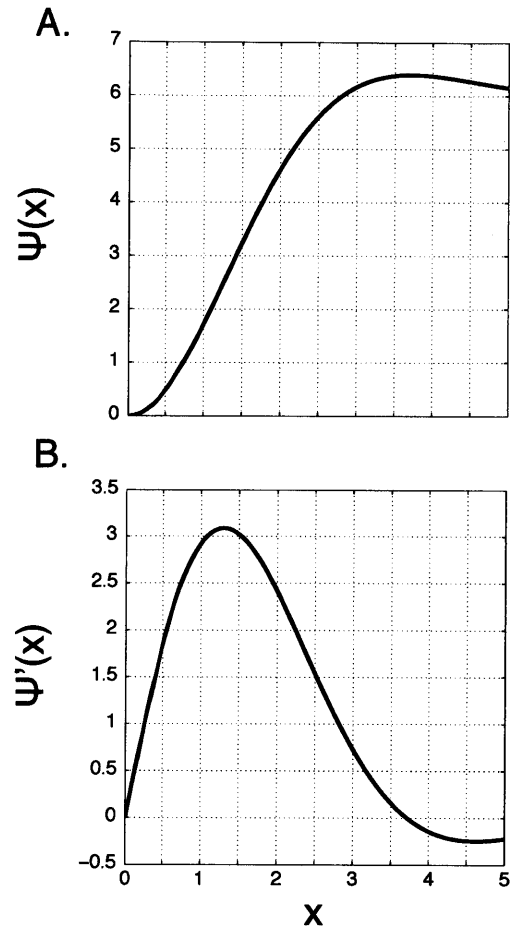


**Figure 2-S1.** Graphical representation of dimensionless function  $\Psi(x)$  (A) and its first derivative (B).  $\Psi(x)$  is used in the calculation of  $W_{INT}$  (Equation 2.12), and  $\Psi'(x)$  is used in the calculation of  $\sigma_R$  through Equation (2.S20).



## **Chapter 3:**

### **Modes of extensional faulting controlled by surface processes<sup>2</sup>**

#### **Abstract**

We investigate the feedbacks between surface processes and tectonics in an extensional setting by coupling a 2D geodynamical model with a landscape evolution law. Focusing on the evolution of a single normal fault, we show that surface processes significantly enhance the amount of horizontal extension a fault can accommodate before being abandoned in favor of a new fault. In simulations with very slow erosion rates, a 15 km-thick brittle layer extends via a succession of crosscutting short-lived faults (heave < 5 km). By contrast, when erosion rates are comparable to the regional extension velocity deformation is accommodated on long-lived faults (heave >10 km). Using simple scaling arguments, we quantify the effect of surface mass removal on the force balance acting on a growing normal fault. This leads us to propose that the major range-bounding normal faults observed in many continental rifts owe their large offsets to erosional and depositional processes.

---

<sup>2</sup> Published as: Olive, J.-A., Behn, M. D., and L. C. Malatesta (2014b), Modes of extensional faulting controlled by surface processes, *Geophys. Res. Lett.*, 41(19).

### 3.1. Introduction

Erosion, sediment transport, and deposition can strongly affect the state of stress and deformation at plate boundaries through the redistribution of surficial masses. These processes are well documented and have been extensively modeled in active orogens [e.g., *Koons*, 1989; *Molnar and England*, 1990; *Avouac and Burov*, 1996; *Willett*, 1999], where surface processes affect the balance of tectonic forces at the scale of the orogenic wedge. Specifically, it has been established that active surface processes favor strain localization along a few long-lived thrusts and back thrusts that are active synkinematically, thereby promoting sustained exhumation of deep crustal units [e.g., *Mugnier et al.*, 1997; *Willett*, 1999; *Konstantinovskaia and Malavieille*, 2005]. By contrast, the morphology of extensional environments is largely controlled by the geometry of a succession of lithospheric-scale normal faults that accommodate most of the strain near the axis of the rift. Potential feedbacks between surface processes and extensional tectonics should therefore be investigated in terms of a force balance at the scale of these individual faults. This study presents a simple mechanical framework quantifying the effect of surface processes on fault geometry and longevity, which is currently lacking in extensional settings.

Earlier studies of the long-term (0.1–10 Myr) coupling between erosion and rifting largely focused on the plate boundary scale and investigated complex feedbacks between surface processes and viscous flow in a multi-layered lithosphere. *Burov and Cloething* [1997], and *Burov and Poliakov* [2001] showed that erosion of the rift shoulder and sedimentation in the rift neck lead to greater lithospheric thinning and basin widening by affecting lithospheric strength profiles. More recently, *Bialas and Buck* [2009] used numerical models to argue that enhanced sedimentation in the northern Gulf of California promotes a transition to narrow rifting compared to the wider, more distributed rifting in the south. They attributed this result to sediments decreasing the change in gravitational force caused by the growth of topography during extension; thereby promoting prolonged extension in a narrow region. Unfortunately, due to their large-scale approach, their models did not properly resolve individual normal faults, and therefore could not test how changes in gravitational force affected the behavior of a specific normal fault.

Indeed, a key parameter in the evolution of extensional plate boundaries is the amount of offset that can be accommodated by a single normal fault before being abandoned in favor of a new one. Broadly speaking, fault life span determines whether the “building block” of a rift system is a half-graben structure (characteristic offset smaller than the faulted layer thickness, typically a few km), a long-lived, low-angle detachment fault (with offset in the 10–50 km range, resulting in surficial exposure of lower crustal units), or a combination of both [e.g., *Morley, 1995; Lavier et al., 2000; Lavier and Buck, 2002; Whitney et al., 2013*]. Over the past two decades a robust conceptual framework has been assembled to identify the first-order controls on the modes of extensional faulting [e.g., *Forsyth, 1992; Buck, 1993; Lavier et al., 2000; Lavier and Buck, 2002; Behn and Ito, 2008; Olive and Behn, 2014*]. These authors considered the mechanical cost of sustaining slip on a single normal fault, which requires an increase in tensional force as extension proceeds. The necessary force increase was shown to be faster in thicker elasto-plastic faulted layers. Consequently, the force threshold for breaking a new fault is met sooner in thicker layers, and extension proceeds by a succession of short-lived normal faults. If the faulted layer is sufficiently thin, the force build-up is moderate and the threshold may never be reached, favoring a succession of large offset faults.

A major limitation of this theory is that for brittle layer thicknesses typical of most continental rift zones only small offset faults are predicted, yet faulting in these regions range from short-lived faults to long-lived detachments forming metamorphic core complexes [e.g., *Whitney et al., 2013*]. Additional controls such as rapid hydrothermal cooling [*Lavier and Buck, 2002*] and magmatic processes [*Buck et al., 2005*] have been proposed to explain large offset faulting, but those are more relevant to mid-ocean ridge settings and thus cannot explain this discrepancy between the models and observations in continental rifts. On the other hand, sub-aerial rifts are subjected to surface processes that rework topography more or less efficiently depending on climatic parameters and basement lithology. By redistributing mass at the surface, these processes have the potential to modify the stress state of the lithosphere and thus influence fault evolution.

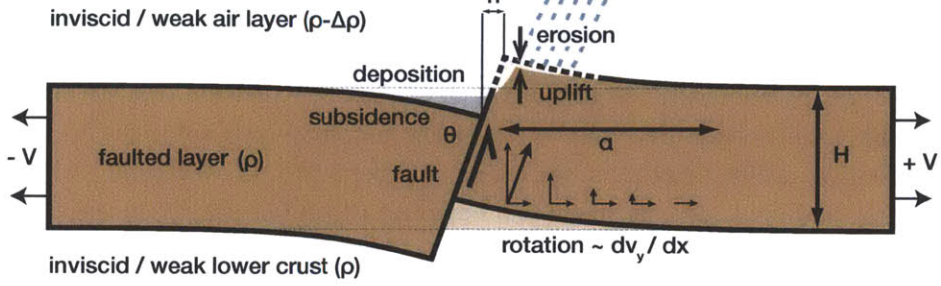
The aim of the present study is to quantify the effect of surface processes on fault life span in an extensional regime. To do so, we conduct 2D geodynamic simulations of fault evolution coupled to a parameterized erosion and deposition model. We complement this numerical approach with a force balance model that explicitly considers the gravitational contribution of topography, a term that was previously parameterized only in combination with footwall and hanging wall flexure [e.g., *Forsyth, 1992; Buck, 1993*] or ignored [*Olive and Behn, 2014*]. We find that when acting at rates comparable to fault slip, surface processes can significantly enhance fault life span by relieving a fraction of the topographic forcing. We identify faulting regimes controlled by the efficiency of surface processes and faulted layer thickness, and discuss their applicability to natural rift systems.

### 3.2. Numerical experiments

We solve for conservation of mass, momentum, and energy in a 2D domain using the finite difference / marker-in-cell technique [*Harlow and Welch, 1965*] described by *Gerya [2010]*. Our model setup (Figure 3-1a) is similar to that of *Olive and Behn [2014]* and treats the brittle upper crust as an elasto-plastic layer of thickness  $H$ , Young's modulus  $E$  (100 GPa), and Poisson's ratio  $\nu$  (0.5). The brittle layer lies above a weak viscous lower crust (Newtonian, with viscosity  $10^{18}$  Pa·s), and beneath a low-viscosity "sticky air" layer (viscosity  $10^{17}$  Pa·s) [*Crameri et al., 2012*]. The base of the faulted layer corresponds to the 600°C isotherm and evolves with temperature. Thermal conductivity is artificially enhanced such that thermal diffusion occurs faster than fault-induced advection, thereby allowing the faulted layer to retain its initial thickness during fault growth [*Lavier and Buck, 2002*]. This allows us to isolate the effect of redistributing surficial mass from that of advective thinning of the brittle layer.

The air layer has a density of  $10^{-2}$  kg·m<sup>-3</sup>; the brittle and lower crustal layers have densities of 2700 kg·m<sup>-3</sup>. To insure that deformation is not influenced by the model boundaries, the width of the box is set to 3 times the (elastic) flexural wavelength of the brittle layer. We pull on each side of the domain at a half-rate,  $V$ , and compensate the horizontal outflow of air and rock by imposing a matching inflow of material through the

**a. model setup**

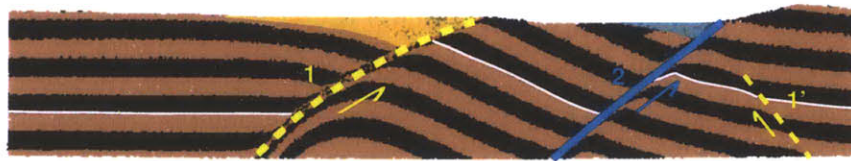


total horizontal extension = 22 km

**b.**  $E_{20} = 0.015 \text{ mm.yr}^{-1}$ ,  $E_{20} / S = 0.0005$



**c.**  $E_{20} = 1.0 \text{ mm.yr}^{-1}$ ,  $E_{20} / S = 0.35$



**d.**  $E_{20} = 15 \text{ mm.yr}^{-1}$ ,  $E_{20} / S = 5.3$



**Figure 3-1. a.** Setup of the numerical and force balance model. An elasto-plastic layer of thickness  $H$  with a weak fault initially seeded at a  $\theta = 60^\circ$  angle undergoes extension at a half-rate  $V$ . The layer has density  $\rho$  and is sandwiched between two weak / inviscid layers (not shown). As the fault accumulates horizontal offset  $h$ , the hanging wall and footwall blocks undergo flexure (over a wavelength  $\alpha$ ), which results in topography growth and fault rotation. The material upwelling beneath the footwall has the same lithology as the brittle layer, but acquires its brittle nature through thermal equilibration as it cools below  $600^\circ\text{C}$ . Surface processes cause footwall erosion and partial filling of flexural basins. **b-d.** Snapshots of numerical simulations after 22 km of extension in a 15 km thick layer extending at a half-rate of  $1 \text{ mm.yr}^{-1}$ . Surface topography is subjected to erosion rates (calibrated on a  $20^\circ$  mean elevation slope) of **(b.)** 0.015, **(c.)** 1.0, and **(d.)**  $15 \text{ mm.yr}^{-1}$ . Yellow dashed lines indicate faults that have been abandoned in a sequence indicated by the numbers. Blue faults are actively growing at the time of the snapshot. Colored areas indicate the material that deposited while the fault of corresponding color was active. In the case of panel **(b)**, where faults are short-lived and closely spaced, the blue material integrates deposits associated with the successive growth of fault #2 and fault #3. The solid white line marks the top of lower crustal units.

top and bottom boundaries of the numerical domain, respectively. Shear tractions are set to zero on all boundaries.

Localized plastic failure (i.e., faulting) occurs spontaneously in our simulations following a Drucker-Prager criterion that approximates an inscribed Mohr-Coulomb yield surface with a friction coefficient of 0.6. Strain localization is promoted by decreasing the material cohesion (initially  $C_0 = 100 \text{ MPa}$ ) linearly with accumulated plastic strain [Lavier *et al.*, 2000] down to a value of 0.01 MPa after a critical plastic strain corresponding to  $\sim 200 \text{ m}$  of fault offset has been exceeded. To initialize strain localization on a single normal fault we impose a rectangular “fault seed” of dip  $\theta_0 = 60^\circ$  and width equal to about 2 grid cells in the middle of the domain within the brittle layer at the beginning of each model run. In this narrow region, plastic strain is set to the critical value and cohesion is decreased accordingly. A “healing” mechanism is implemented to promote strain localization [Poliakov and Buck, 1998].

Surface topography,  $y(x)$ , is tracked using a chain of closely spaced markers that separate the air layer from the brittle rock layer. At the end of each “tectonic” time step ( $\Delta t$ ), the topography is advected using the current velocity field. We then modify the

topography by solving a landscape evolution law on the surface marker chain over the time  $\Delta t$ . All markers located above the updated topography become of type “air” (i.e., acquire the density and rheological properties of the weak air layer), while markers located beneath become “rock”. This new marker distribution is then used to calculate the next “tectonic” velocity field.

The first step in our landscape evolution model consists of eroding topography to create a surface that reflects the mean elevation profile of a mountain range. The 2-D nature of our approach simplifies the average of the profiles of concave-up trunk rivers and convex-up ridgelines to a largely constant slope that relaxes to shallower angles across the foothills. To do so, we scale the erosion rate with the local slope:

$$\frac{\partial y}{\partial t} = -K \left| \frac{\partial y}{\partial x} \right|^n \quad (3.1)$$

Because the profile of mean elevations differs from that of the trunk river, we omit the upstream drainage area component used in stream power models [e.g., *Whipple, 2004*, and references therein]. We set  $n = 1.3$ , which was empirically found to generate realistic topographies across a range of  $K$  values. The coefficient  $K$  accounts for erosional resistance and climatic conditions, and can be calibrated at field sites where mean elevation slope and erosion rate are known. For simplicity, we hereafter refer to various values of  $K$  (the main control on the efficiency of surface processes) in terms of the corresponding erosion rate in a  $20^\circ$  sloping mountain front,  $E_{20}$ , defined as

$$E_{20} = K \tan^n(20^\circ) \quad (3.2)$$

Following the erosion step, we identify watersheds across the model domain by first locating the topographic highs. We calculate the volume of eroded material in each watershed and then deposit that volume horizontally at the bottom of the same watershed. The flat deposition at the toe of the slopes simulates sediment redistribution processes in floodplains or playas. Deposition ceases if the eroded volume exceeds the current basin capacity. In this scenario, the filled basin is then integrated with the neighboring watershed at the next erosion step. Negligible sedimentation occurs in watersheds that border the model domain because the edges of the model act as sinks allowing the material to leave the domain.

We conducted 21 numerical simulations in which we systematically varied  $E_{20}$  between 0.015 and 150  $\text{mm}\cdot\text{yr}^{-1}$ , with an emphasis on the geologically relevant interval of 0.015–10  $\text{mm}\cdot\text{yr}^{-1}$  [e.g., *Herman et al.*, 2013]. We chose a brittle layer thickness of 15 km extending at a half-rate of either 1 or 10  $\text{mm}\cdot\text{yr}^{-1}$ , which is representative of many continental rifts [e.g., *Chen and Molnar*, 1983; *Strak*, 2012]. We also examined cases with a 25 km thick layer, representing colder rifts such as certain portions of the East African Rift or the Baikal Rift [*Lavier and Buck*, 2002]. A summary of our simulation parameters is given in Table 3-1. In each run, we measure the total amount of horizontal extension ( $h_{MAX}$ ) accommodated on the initial fault when (if) the next fault breaks; or more precisely when accumulated plastic strain starts to heal on the initial fault and build up on the new fault. We also monitor the progressive rotation of the initial fault and characterize the modes of faulting (e.g., multiple, short-lived faults vs. a single long-lived detachment) over  $\sim 40$  km of total extension.

### 3.3. Results

In all numerical simulations, shear deformation localizes rapidly along the seeded fault, inducing flexural uplift and subsidence of the footwall and hanging wall blocks, respectively (Figure 3-1a). The exposed fault scarp systematically features the steepest slopes and is therefore subjected to the fastest erosion. The corresponding erosion products deposit in the flexural basin formed by the subsiding hanging wall, while the ridge of the footwall retreats away from the basin. As extension proceeds on the fault, an equilibrium topography consisting of a footwall high and a partially filled hanging wall basin is reached in cases where  $E_{20}$  and  $V$  are of the same order of magnitude. Topography is essentially suppressed when  $E_{20}$  exceeds  $\sim 5$  times the extension half-rate  $V$ .

Our numerical simulations reveal that for a given layer thickness and extension rate, increasing the erosion rate  $E_{20}$  can have a dramatic effect on the modes of faulting. Figure 3-1b-d shows snapshots of layer deformation after 22 km of total extension in a 15 km thick layer at a half-rate  $V = 1 \text{ mm}\cdot\text{yr}^{-1}$ . At very low erosion rates ( $E_{20} = 0.015 \text{ mm}\cdot\text{yr}^{-1}$ , Figure 3-1b), the initial fault accommodates  $\sim 3.7$  km of extension before an antithetic fault breaks and takes up the next  $\sim 6$  km of extension, uplifting and

$E_{20}$ (mm.yr <sup>-1</sup> )	V (mm.yr <sup>-1</sup> )	$E_{20} / S$	H (km)	$\theta_{MIN}$ (°)	$h_{MAX}$ (km)
0.015	1	0.005	15	47.4	3.6
0.15	1	0.05	15	44.7	4.0
0.5	1	0.18	15	43.5	4.8
0.75	1	0.27	15	41.2	6.1
1.0	1	0.35	15	32.6	14.5
1.5	1	0.53	15	33.1	11.0
2.5	1	0.88	15	33.6	11.2
5	1	1.77	15	33.1	12.5
7.5	1	2.65	15	31.9	infinite
10	1	3.54	15	32.0	infinite
15	1	5.30	15	32.7	infinite
0.015	1	0.005	25	47.6	4.0
0.5	1	0.18	25	45.8	5.6
1.0	1	0.35	25	40.1	8.3
5.0	1	1.77	25	39.2	9.4
15	1	5.30	25	36.1	14.3
0.015	10	0.0005	15	48.0	3.7
1.0	10	0.04	15	46.1	4.1
10	10	0.35	15	35.5	10.6
15	10	0.53	15	32.2	13.3
150	10	5.30	15	30.9	infinite

**Table 3-1.** Summary of parameters and results of our numerical experiments.

subsequently eroding the sediments deposited in the hanging wall of the first fault. A third antithetic fault then forms, and new sediments begin infilling the basin formed by the 3<sup>rd</sup> active fault and the topographic high inherited, but not yet eroded, from the second fault. Extension therefore proceeds as a succession of short-offset antithetic faults.

By contrast, at a higher erosion rate of 1 mm·yr<sup>-1</sup>, the initial fault remains active longer and accommodates more extension. In this case, the first ~10 km of extension are taken up on the initial fault, followed by the development of two blind antithetic faults in the footwall block. Over the next few km of extension, the two small faults (1' and 2 in Figure 3-1c) accommodate a significant fraction of the total plate separation, until the fault dipping parallel to the master fault cuts through the entire layer and localizes all the

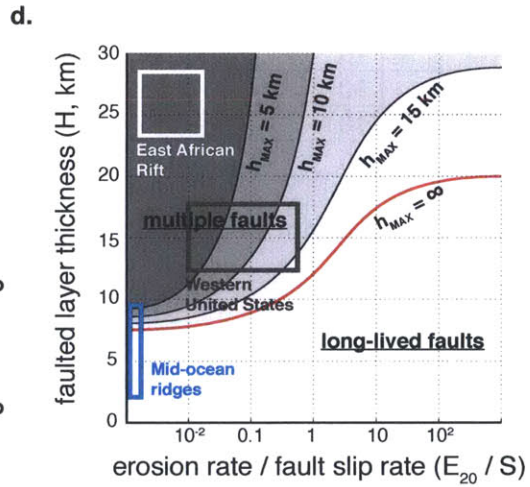
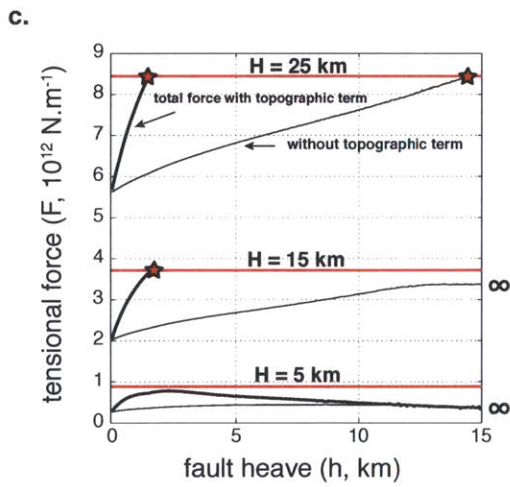
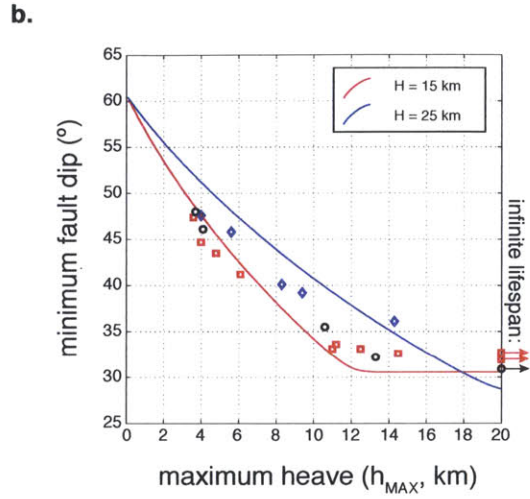
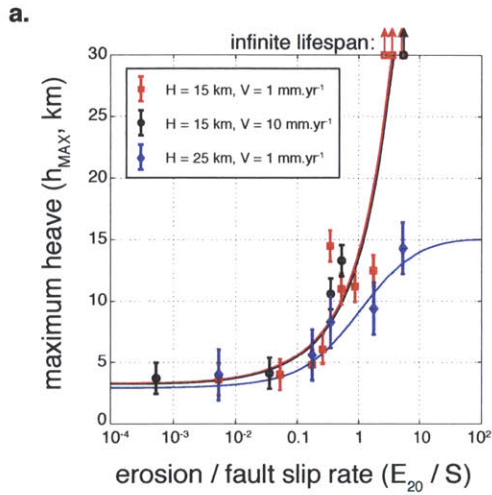


**Figure 3-2.** **a.** Maximum heave accommodated on the initial normal fault in the numerical model, as a function of erosion rate ( $E_{20}$ , calibrated on  $20^\circ$  mean elevation slopes) normalized by the long-term fault slip rate ( $S = 2V / \cos \theta$ , assuming a mean fault dip of  $45^\circ$ ). Data points span various brittle layer thicknesses and extension rates (see legend). Arrows indicate cases where faults grew indefinitely. The error bars correspond to 3 cell sizes near the fault ( $\sim 1.5$  km), which sets the uncertainty in our measurement of fault life span. The red, black and blue curves illustrate the behavior expected from our force-balance model, with the color key indicated in the legend. **b.** Lowest dip reached by the initial normal fault (initially dipping  $60^\circ$ ) when it becomes abandoned in favor of a new fault (or for an “infinite” amount of offset). The red and blue curves correspond to our kinematic model of fault rotation (see Appendix 3.1) in a 15 km and a 25 km-thick faulted layer, respectively. **c.** Force needed to sustain slip on a normal fault as a function of accumulated heave, for various faulted layer thicknesses  $H$ . The thick and thin lines show the total force with and without the component corresponding to topography growth  $F_{TOPO}$ , respectively. The red stars mark the amount of horizontal extension that can be accommodated when the force threshold to break a new fault in intact lithosphere (horizontal red line) is reached. The infinity symbols indicate cases where faults can grow indefinitely. **d.** Conceptual regime diagram showing fault life span  $h_{MAX}$  as a function of faulted layer thickness and the ratio of erosion rate to long-term slip rates, as inferred from our force balance model. Representative parameter values are indicated for various extensional settings.

extension (Fault 2 in Figure 3-1c), resulting in abandonment of the initial master fault. Fault 2 becomes the next master fault, and the same pattern repeats. Extension is therefore taken up by a succession of large offset (10–15 km) sub-parallel faults. A topographic high can only be sustained in the footwall of the actively growing fault since erosion rapidly levels the topography once a fault is abandoned.

Finally, at very high erosion rates ( $E_{20} = 15 \text{ mm} \cdot \text{yr}^{-1}$ ) (Figure 3-1d) the initial fault remains active indefinitely, accommodating  $\geq 50$  km of extension (corresponding to the extent of the simulation). Significant flexural deformation occurs in the footwall, and lower-crustal units become exposed at the surface. However, no characteristic topography can develop as the (unrealistically) high erosion rates force the surface to remain flat throughout the experiment.

Figure 3-2a (and Table 3-1) shows the life span  $h_{MAX}$  of the initially seeded fault plotted against the reference erosion rate  $E_{20}$  normalized by the average fault slip rate  $S$ .

Faults in a 15 km-thick brittle layer subjected to slow erosion rates ( $E_{20} \leq 0.15 \text{ mm}\cdot\text{yr}^{-1}$ ) accommodate  $\sim 4$  km of extension before being abandoned, regardless of extension rate. Fault life span is weakly sensitive to very slow erosion rates, but increases sharply when the ratio of erosion rate to long-term fault slip rate  $E_{20} / S$  exceeds  $\sim 0.1$ .  $E_{20} / S > \sim 2$  promote infinite growth of the initial normal fault and the suppression of all topography. Brittle layer thickness strongly modulates the sensitivity of fault life span to surface processes. Consistently with earlier studies, fault life span is systematically shorter in a 25 km-thick layer than in a 15-km thick layer, across the entire range of  $E_{20} / S$  (Figure 3-2a). Moreover, while extremely fast normalized erosion rates ( $E_{20} / S > \sim 2$ ) lead to infinite fault growth in a 15 km-thick layer, these rates only extend fault life span to 15 km in a 25 km-thick lithosphere.

In addition to topography and fault life span, we also monitor the evolving fault dip by visually fitting a line to the region of greatest accumulated plastic strain (Figure 3-2b). When fault offset becomes comparable to the thickness of the faulted layer, the fault develops significant concave down curvature [e.g., *Choi and Buck, 2012*]. In these situations, we restrict our visual fit to the upper-half of the faulted layer to yield an upper estimate of fault rotation. Faults rotate rapidly from their initial angle ( $\sim 60^\circ$ ) down to dips of  $30\text{--}45^\circ$ , in accordance with a model in which the fault rotates to minimize the total extensional work [*Olive and Behn, 2014*]. We find that fault rotation is slower in a 25 km thick faulted layer than in a 15 km thick layer, consistent with the predictions of *Olive and Behn [2014]*. Rotation progressively slows with total extension, reaching a minimum dip when the total fault heave exceeds the faulted layer thickness. The amount of rotation at a given time depends solely on the faulted layer thickness and the amount of extension accommodated on the fault. Thus, surface processes act to prolong fault life span, but do not strongly influence the kinematics of fault rotation.

### **3.4. Topographic forcing on fault life span**

To further quantify the influence of surface processes on fault life span, we complement our numerical approach with a simple force balance model for a growing normal fault [*Buck, 1991; Lavier et al., 2000; Behn and Ito, 2008*]. The basic assumption of this class of models is that an active fault will be abandoned when the force required to keep it

active exceeds the threshold force needed to break a new fault. The total force,  $F$ , represents the depth-averaged deviatoric stress acting on the fault [Forsyth, 1992], and can be decomposed into the force required to sustain frictional slip on the fault,  $F_{FRIC}$ , the force required to bend the footwall and hanging wall blocks as the fault accumulates offset,  $F_{BEND}$ , and the force required to sustain topography,  $F_{TOPO}$ .

By definition, the work done by the bending and topographic forces corresponds to the internal strain energy stored in the faulted layer, and to the change in gravitational potential energy associated with topography build-up, respectively.  $F_{BEND}$  and  $F_{TOPO}$  can therefore be expressed as the derivative of those work terms with respect to horizontal extension [Forsyth, 1992; Buck, 1993; Olive and Behn, 2014]. We estimate these forces by treating the faulted layer as an elasto-plastic thin plate [Buck, 1988; 1993] with a triangular yield strength envelope approximating that used in the numerical simulations. Fault topography, after a given amount of horizontal extension  $h$ , is modeled as the flexural readjustment to the rigid uplift / subsidence of the footwall and hanging wall [Weissel and Karner, 1989; Olive and Behn, 2014]. Plate rigidity is decreased iteratively in regions of high plate curvature, until the effective elastic bending moment matches that of the elasto-plastic plate [Buck, 1988]. The flexure equation with spatially varying rigidity is then solved with finite difference to obtain the fault induced topography  $y(x)$ . The bending work  $W_{BEND}$  is obtained by integrating the bending stress times the bending strain over the entire layer. The topographic work corresponds to the change in gravitational potential energy associated with offsetting the air-rock density contrast,  $\Delta\rho$ , from its initial flat state.

It has long been recognized that fault dip plays a key role in modulating the forces acting on a fault [Forsyth, 1992]. Here we incorporate fault rotation to the force balance model using a simple kinematic approach. Following Olive and Behn [2014], we assume that fault rotation results from passive advection of the fault in the displacement field induced by flexure of the footwall and hanging-wall blocks. The rotational component of this displacement field is due largely to the decreasing magnitude of vertical motion that occurs over approximately one flexural wavelength from the fault (Figure 3-1a). The average rotation rate therefore inversely scales with the flexural wavelength, and is slower in stronger, thicker layers.

Once the modeled fault topography is obtained for a given amount of extension  $h$ , we infer the effective flexural wavelength of our elasto-plastic thin plate and use it to update the fault angle at step  $h+\Delta h$  (see details in Appendix 3.1). To prevent the fault from reaching very low dip angles in the force balance model, which are not observed in the numerical models, we assume that rotation ceases once the heave becomes comparable to the faulted layer thickness. This corresponds to faults that have acquired significant curvature after footwall rollover has occurred [Choi and Buck, 2012]. This approach is simpler to implement in an elasto-plastic layer than the energy minimization model of Olive and Behn [2014] and predicts similar rotation kinematics, suggesting that flexural rotation allows faults to stay close to their lowest energy configuration (see Appendix 3.2). Our predictions of fault rotation are shown in Figure 3-2b, and match the results of our numerical simulations. In particular, slower rotation in the thicker 25 km layer is well explained by the scaling of rotation rates with the inverse of flexural wavelength ( $\sim H^{3/4}$ ).

Armed with a self-consistent force balance model that incorporates fault rotation, we can now quantify the effect of topographic growth on fault life span. In Figure 3-2c we plot the increase in the total force acting on a growing fault with and without the topographic component  $F_{TOPO}$  (thick and thin black lines, respectively). Ignoring  $F_{TOPO}$  in the force balance is analogous to cases in which erosion and deposition rapidly suppress topographic growth, i.e.,  $E_{20} \gg S$  in our numerical simulations. Consistent with Buck [1993] and Lavier *et al.* [2000], we find that faults growing in thin layers ( $H < \sim 10$  km) remain active indefinitely as the force required to sustain fault slip never exceeds the threshold to break a new fault. This occurs regardless of the incorporation of  $F_{TOPO}$ . By contrast, thicker ( $\geq 10$  km) layers only produce small offset ( $\sim 2$  km) faults when  $F_{TOPO}$  is included in the force balance. However, removing  $F_{TOPO}$  (as would correspond to more rapid erosion and deposition rates) causes a dramatic increase in fault life span. In particular, for layer thicknesses of 15–25 km, removing  $F_{TOPO}$  has a significantly greater effect on fault life span than does brittle layer thickness. Finally, we note that the topographic force accounts for a smaller proportion of the total force acting on a fault when the brittle layer is thicker. This explains why very active surface processes promote

infinite fault growth in 15 km thick layers, while only extending fault life span to ~15 km in 25 km-thick layers.

### 3.5. Application to rift systems

The conceptual regime diagram shown in Figure 3-2d summarizes our findings. This is analogous to the regime diagrams proposed by *Lavier et al.* [2000] and *Lavier and Buck* [2002] with a new parameter accounting for the efficiency of surface processes at relieving topographic loads. Continental rifts are frequently characterized by a brittle layer thickness of ~15 km, as inferred from seismicity, flexural and heat flow constraints [*Chen and Molnar*, 1983]. Models that do not include surface processes predict that faulting in a 15 km-thick brittle layer (i.e., the upper continental crust) should proceed by a succession (or synkinematic slip) of moderate-offset ( $h_{MAX} \sim 3\text{--}5$  km) normal faults leading to the formation of grabens and half-grabens. However, significant offset has been observed along major faults of the Basin and Range province. For instance, the Wasatch fault in Utah has accumulated as much as 11 km of vertical offset [*Parry and Bruhn*, 1987]. As shown above, such large offsets in 15–25 km-thick lithosphere can only occur if surface processes relieve a portion of the topographic forcing, provided that erosion acts at rates comparable to tectonic slip. Thermochronologic studies suggest long-term slip rates on the Wasatch fault of  $\sim 0.4$  mm.yr<sup>-1</sup> over the last ~10 Myrs [*Naeser et al.*, 1983] and erosion rates ranging from 0.07 to 0.14 mm.yr<sup>-1</sup> in Wasatch Mountains river catchments along the Weber segment [*Stock et al.*, 2009]. These erosion rates can be extrapolated to a representative  $E_{20}$  value of  $\sim 0.16$  mm.yr<sup>-1</sup> after calibration against local mean elevation slopes. This yields a ratio of  $E_{20} / S \sim 0.4$ , which in our models promotes fault life span as large as 10–15 km. Thus, we propose that the Wasatch fault owes its significant life span to the coupling between tectonics and surface processes. Further, by ensuring a longer fault life span, surface processes promote further rotation away from a steep Andersonian initiation angle and indeed dips as low as ~30–45° have been proposed for the Wasatch fault [*Harris et al.*, 2000].

Some rift zones (e.g., the Baikal Rift, portions of the East African Rift, the Gulf of Suez) are associated with thicker brittle layers (25–30 km) potentially inherited from a cratonic lithosphere and / or associated with lower heat flow [e.g., *Chen and Molnar*,

1983; *Lavier and Buck, 2002*]. Along the East-African Rift, for instance, many half-grabens feature valley-bounding faults that accommodate only a few km of extension before deformation jumps to another locus [e.g., *Morley, 1995*] and large-offset normal faults are absent. This is consistent with the slow erosion rates ( $< 0.1 \text{ mm.yr}^{-1}$ ) inferred over the East African Rift [*Herman et al., 2013*]. However, active glacial erosion may have locally contributed to anomalously high displacement ( $> 6 \text{ km}$ ) on horst-bounding faults, as proposed in the Rwenzori Mountains [*Ring, 2008*].

Finally, we note that mid-ocean ridges are generally characterized by thin ( $< 10 \text{ km}$ ) lithosphere, and very limited erosion and sedimentation. Thus, fault evolution and the frequency of large-offset oceanic detachment faults in these environments are likely controlled by the thin lithosphere and the kinematic effects of dike emplacement [*Buck et al., 2005; Tucholke et al., 2008*]. However, *Choi & Buck [2012]* showed that volcanic infill of flexural basins can influence patterns of fault evolution at ridges, and thus even in these environments surface mass redistribution may play a role in controlling the mode of faulting.

### **3.6. Conclusions**

In conclusion, we have shown that surface processes can significantly enhance the life span of an individual normal fault, provided they act on a time scale comparable to, or faster than, long-term tectonic rates. We suggest that erosion and deposition are essential in sustaining slip on large-offset range bounding normal faults at continental rifts which would otherwise have been abandoned after a few km of offset. Future challenges include: (1) parameterizing the effects of erosion in a way that can be linked to climatic parameters [e.g., *Willett, 2009*], and (2) investigating the three-dimensional feedbacks between fault growth and surface processes, which may include controls on fault segmentation and linkage.

### Appendix 3.1. Kinematic model of fault rotation

In the second chapter of this thesis [Olive and Behn, 2014], we presented a conceptual framework for understanding the rapid rotation of normal faults from a steep 60°-initiation angle down to dip angles in the 30–45° range, over a few km of offset. We proposed that fault evolution proceeded in a manner that systematically minimized the mechanical work required to sustain fault slip, and showed that (1) this assumption results in rotation rates that scale roughly as the inverse of the faulted layer thickness, and (2) accounting for rotation is essential to correctly predict fault life span in a force balance model. Here we adopt a complementary approach, which is significantly less computationally challenging to implement, but produces very similar rotation rates (see below). Specifically, instead of assuming work minimization, we model fault rotation as the passive advection of the fault plane in the displacement field induced by flexural relaxation of the footwall and hanging wall blocks.

If we denote  $\dot{\Omega}$  the average rotation rate of the near-fault displacement field, then the fault rotation rate will scale roughly as

$$\frac{\partial\theta}{\partial t} \sim -\dot{\Omega} \quad (3.S1)$$

To first order, the main source of rotation in the flexural displacement field is the lateral gradient of vertical motion (Figure 3-1a), which is maximal at the fault and equal to  $V \tan\theta$ , and becomes negligible a fraction of the flexural wavelength ( $\gamma\alpha$ , the lever arm, where  $\gamma$  is a scaling factor and  $\alpha$  is the flexural wavelength) away from the fault. We therefore write

$$\dot{\Omega} \sim \frac{1}{2} \frac{\partial v_z}{\partial x} \sim \frac{1}{2} \frac{V \tan\theta}{\gamma\alpha} \quad (3.S2)$$

Plugging (3.S2) into (3.S1) with the constraint  $h = 2Vt$  yields

$$\frac{\partial\theta}{\partial h} = -\frac{\tan\theta}{4\gamma\alpha} \quad (3.S3)$$

Which can be integrated into

$$\theta = \sin^{-1} \left( \sin\theta_0 \exp \left( -\frac{1}{4\gamma} \int_0^h \frac{dh}{\alpha(h)} \right) \right) \quad (3.S4)$$

In addition, we taper the rotation rate at heaves greater than 80% of the faulted layer thickness so that rotation ceases at large offsets, when the fault has become curved and the idealized fault geometry depicted in Figure 3-1a no longer applies.

Fault rotation enters the force balance model in several ways. As extension proceeds, the elastic-plastic iterations predict the fault-induced topography [Buck, 1988; 1993]. At every extension step ( $h$ ), we fit this topography with the elastic solution of *Weissel and Karner* [1989] and determine an equivalent elastic thickness for the entire plate. We then use it to calculate an equivalent flexural wavelength,  $\alpha(h)$ , which enters into the calculation of the next fault dip at step ( $h+\Delta h$ ) following Equation (3.S4). We find that a scaling factor  $\gamma = 0.25$  provides a good fit to the numerical models, regardless of layer thickness and other parameters. In other words, the lever arm associated with fault rotation corresponds to about a fourth of the effective flexural wavelength of the faulted layer.

Once fault dip has been updated, it enters the calculation of the frictional force  $F_{FRIC}$ , following [Behn and Ito, 2008]

$$F_{FRIC} = \frac{\mu\rho gH/2 + HC}{\mu \sin^2 \theta + \sin \theta \cos \theta} \quad (3.S5)$$

For reference, the threshold for breaking a new fault is given by

$$F_{BREAK} = \frac{\mu\rho gH/2 + HC_0}{\mu \sin^2 \theta_0 + \sin \theta_0 \cos \theta_0} \quad (3.S6)$$

where  $\theta_0$  corresponds to the Andersonian dip for a new fault breaking intact lithosphere. (All notations are summarized in Figure 3-1a).

Fault dip also enters the calculation of the bending and topographic forces. A fault that rotates as it accumulates offset generates less throw than if it were to retain its initial angle. We therefore slightly modify the method of *Weissel and Karner* [1989] by using an effective dip  $\theta_{EFF}$  in the loading term of the flexure equation ( $w^*(x)$  in *Olive and Behn*, 2014). For a given amount of heave ( $h$ ) this effective dip yields the amount of throw that would have been reached by a rotating fault, and can be written:

$$\theta_{EFF} = \tan^{-1} \left( \frac{1}{h} \int_0^h \tan \theta(h) dh \right) \quad (3.S7)$$

$\theta_{EFF}$  then enters the calculation of the fault-induced topography and the associated work terms. Specifically, the bending work  $W_{BEND}$  is obtained by integrating the bending stress times the bending strain over the entire layer [Olive and Behn, 2014], while the topographic work  $W_{TOPO}$  corresponds to the change in gravitational potential energy associated with offsetting the air-rock density contrast,  $\Delta\rho$ , from its initial flat state, and is written

$$W_{TOPO} = \int_{-\infty}^{+\infty} \Delta\rho g y^2(x) dx \quad (3.S8)$$

### Appendix 3.2. Comparison with the energy minimization model of Chapter 2

In the second chapter of this thesis [Olive and Behn, 2014], we suggested that fault rotation proceeds in a manner that minimizes the work needed to sustain fault slip, but did not explicitly consider the physical mechanism that causes rotation. The present approach suggests that passive advection of the fault plane in a flexural displacement field provides a good candidate to explain the kinetics of rotation observed in numerical experiments. Indeed, this new model predicts the rotation kinematics observed in our simulations (Figure 3-2b). Much like the energy minimization model, it accounts for rapid rotation of normal faults down to dip angles of 30–45° over fault heaves shorter than half of the faulted layer thickness. Further, the inverse scaling of rotation rate with layer thickness is evident from Equation (3.S3) and is derived from the fact that thicker layers bend on a larger wavelength, making faults rotate about a longer lever arm.

Finally, we find that the present kinematic model for fault rotation predicts dips that remain close to the lowest energy configuration throughout fault evolution, even though energy minimization was not assumed. Figure 3-S1 compares the kinematic elastic-plastic solution for a 15 km thick layer (red line in Figure 3-2b) to an energy minimization model where plasticity is accounted for by assuming an effective elastic thickness of 7.5 km. Colors indicate the total amount of work required to sustain slip on the fault. The kinematic rotation model predicts slightly slower rotation than the energy minimization model for small offsets, which provides a better fit to numerical experiments (Figure 3-2b).

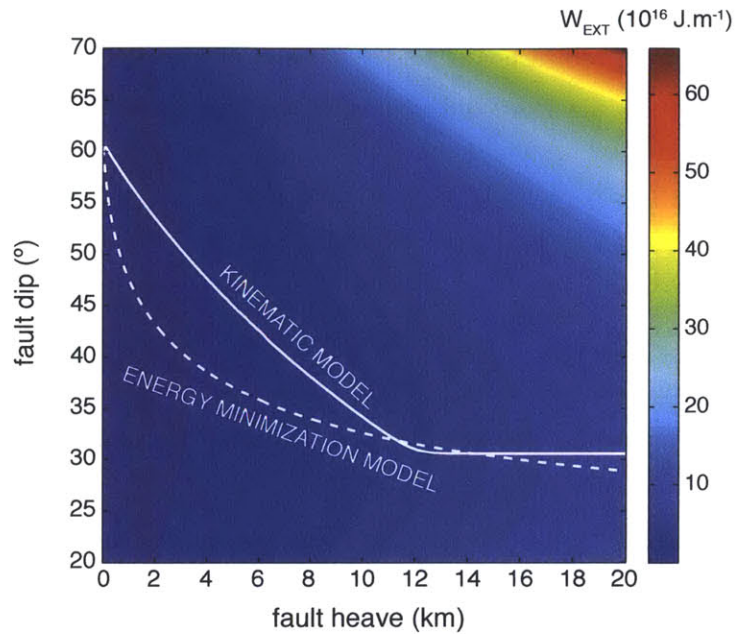


**Figure 3-S1.** Total external work ( $W_{EXT} = W_{FRIC} + W_{BEND} + W_{TOPO}$ ) required to keep a normal fault active as a function of fault dip and heave for increasing amounts of extension in a 15 km thick elastic pseudo-plastic layer with an effective elastic thickness of 7.5 km. The white dashed line indicates the lowest energy path computed following the model of *Olive and Behn* [2014] taking into account all energy terms:  $W_{FRIC}$ ,  $W_{BEND}$ , and  $W_{TOPO}$ , the last of which was previously ignored. The thick white line shows the kinematic rotation model used in this study.





## **Chapter 4:**

### **The role of elasticity in simulating long-term tectonic extension**

#### **Abstract**

While elasticity is a defining characteristic of the Earth's lithosphere, it is often ignored in numerical models of long-term tectonic processes in favor of a simpler visco-plastic description. Here we assess the consequences of this assumption on a well-studied geodynamic problem: the growth of individual normal faults at an extensional plate boundary. We conduct 2-D numerical simulations of extension in elasto-plastic and visco-plastic layers using a finite difference, particle-in-cell numerical approach. Our models span a wide range of faulted layer thicknesses and extension rates, which allows us to quantify the role of elasticity on three key observables: fault-induced topography, fault rotation, and fault life span. In agreement with earlier studies, simulations carried out in elasto-plastic layers produce rate-independent lithospheric flexure accompanied by rapid fault rotation and shorter fault life spans in thicker faulted layers. By contrast, models carried out with a visco-plastic lithosphere produce results that depend strongly on extension rate. At slow extension rates and moderate lithospheric viscosities, fault evolution is qualitatively similar to the elasto-plastic cases. However, fast rates and high lithospheric viscosities generate little deformation of the footwall and hanging wall blocks, suppress fault rotation, and promote long-lived faults associated with unrealistically flat topography. To help interpret these results, we adapt a classic analytical model for fault-induced elastic flexure to the case of a thin viscous plate. By doing so we elucidate the rate-dependence of the flexural wavelength of a viscous plate, and quantify the length scale over which topography decays away from the fault as a function of extension rate. We show that visco-plastic numerical simulations qualitatively mimic the behavior of their elasto-plastic counterparts only if the horizontal dimension of the model domain accommodates  $\sim 2$  viscous flexural wavelengths. When this criterion is not met, the rate-dependence of visco-plastic plate behavior produces unrealistic deformation patterns that can hinder geological interpretations, especially in models of long-term lithosphere evolution that involve sequential faulting.

#### 4.1. Introduction

The Earth's lithosphere is commonly defined as the outermost mechanical layer that can withstand deviatoric stresses as large as  $\sim 10^2$  MPa before it yields, either through brittle failure or localized viscous creep [e.g., *Murrell, 1976; Goetze and Evans, 1979; Watts and Burov, 2003*]. Consequently, it does not undergo diffuse viscous deformation at time scales characteristic of mantle convection or plate boundary processes. In fact, when subjected to stresses below the brittle strength, the lithosphere is best described as an elastic medium. Short-term tectonic processes (seconds to months) such as seismic wave propagation or coseismic stress changes are well accounted for by linear elastic models [e.g., *King et al., 1994; Segall, 2010*]. This is also true for some long-term processes ( $10^5$ – $10^7$  yrs) including lithospheric flexure in response to seamount loading, subduction, and active faulting, which are all well modeled by the deflection of a thin elastic plate [e.g., *Watts, 2001*]. Interestingly, elastic models often do a good job at predicting flexural patterns even in regions where brittle failure is known to be pervasive. For example, the long-wavelength topography of outer rises near subduction trenches is well predicted by elastic plate models [e.g., *Turcotte and Schubert, 2002*] even though widespread normal faulting is well documented in these settings, indicative of brittle failure of the lithosphere [e.g., *Ranero et al., 2003; Zhang et al., 2014*]. Elastic rheology therefore underlies the behavior of the lithosphere over a range of spatial and temporal scales, and stress conditions.

In spite of its importance in plate tectonic processes, elastic rheology is absent from many numerical geodynamic models, which treat the lithosphere as a high-viscosity visco-plastic solid. This description can be simpler to implement in a Stokes flow solver because it does not require keeping track of the build-up of stresses over time. A common justification for this simplification is that the duration of these simulations (1–100 Myrs) exceeds the Maxwell time scale expected for the lithosphere ( $< 0.3$  Myr). For example, *Kaus and Becker [2007]* showed that elasticity has little influence on the development of Rayleigh-Taylor instabilities with viscosities and density contrasts representative of mantle convection and sub-lithospheric flow conditions. However, they pointed out that incorporating elasticity significantly changes the patterns of stress accumulation throughout the model domain. One might therefore expect a key role of elasticity in

problems involving plate flexure, buckling instabilities, and strain localization [Schmalholz and Podladchikov, 1999; Kaus and Podladchikov, 2006]. In particular, models of long-term lithospheric deformation that involve faulting (e.g., mountain building and rifting) may be especially sensitive to the incorporation of elasticity. Here we focus on extensional plate boundaries, and particularly on the growth of individual rift-bounding normal faults, which involves both strain localization and lithospheric flexure.

Many numerical studies of rifting do not include elasticity [e.g., Behn *et al.*, 2002b; Gerya 2010b; 2013; Allken *et al.*, 2011, 2012; 2013; Püthe and Gerya, 2013] and treat the oceanic lithosphere or brittle upper crust as a high viscosity visco-plastic layer. However, in the context of long-term tectonic rifting models, the importance of elasticity may be twofold. First, the relevant time scale in such models is not the duration of the simulation, but the life span of individual normal faults, which can be as short as  $\sim 10^4$  yrs depending on geological parameters and extension rate. The visco-plastic approximation routinely applied to mantle convection models may therefore not apply here. Second, numerous studies, including Chapters 2 and 3 of this thesis have shown that normal fault evolution is controlled by the build-up of elasto-plastic stresses in the faulted layer. This build-up is generally attributed to the flexural readjustment of the footwall and hanging wall blocks in response to fault growth [Buck, 1988; Weissel and Karner, 1989; King *et al.*, 1988], and has consequences for both fault rotation [Olive and Behn, 2014; Olive *et al.*, 2014b] and fault life span, hereafter defined as the amount of horizontal offset that can be accommodated on a fault before it is abandoned in favor of a new fault [Forsyth, 1992; Buck, 1993; Lavier *et al.*, 2000; Behn and Ito, 2008]. It is therefore unclear to what extent a visco-plastic description of the lithosphere can produce behaviors that are relevant for understanding geological systems.

To address this issue, we compare numerical simulations of extension carried out within the same numerical code, but with a visco-plastic vs. elasto-plastic brittle layer. We identify and interpret the discrepancies between the two sets of simulations with the help of semi-analytical models of flexure in elastic and viscous thin plates. Specifically, we show that a key to avoiding unrealistic rate-dependence of model results that do not incorporate elasticity is to resolve the time-evolving viscous flexural wavelength of

visco-plastic layers within the model domain. We conclude with recommendations for the numerical modeling community and guidelines for interpreting visco-plastic models.

## 4.2. Methods

To assess the effect of elasticity on the development of normal faults, we performed 29 simulations of extension on a single fault in uniform brittle layers of varying thicknesses over a range of extension rates, both with and without elasticity. We systematically characterized fault-induced topography, fault dip, and fault life span from each of these simulations.

### 4.2.1. Numerical methodology

Our simulations were carried out using a 2-D finite-difference / particle-in-cell code [Harlow and Welch 1965; Gerya and Yuen 2003; 2007] that we developed based on the methodology of Gerya [2010a]. This code relies heavily on Matlab's built-in functions and capabilities for vector operations, and achieves computation speeds on par with standard serial compiled language codes. We solve for conservation of mass, momentum and energy in a 2D continuum assuming material incompressibility:

$$\frac{\partial v_i}{\partial x_i} = 0 \quad (4.1)$$

$$\frac{\partial \sigma'_{ij}}{\partial x_j} - \frac{\partial P}{\partial x_i} + \rho g_i = 0 \quad (4.2)$$

$$\rho c_p \frac{DT}{Dt} = \frac{\partial}{\partial x_i} \left( k \frac{\partial T}{\partial x_i} \right) \quad (4.3)$$

where  $v_i$ ,  $\sigma'_{ij}$ , and  $T$  denote velocities, deviatoric stresses, and temperature, respectively (See Table 4-1 for a summary of all variables). Repeated indices imply summation and the first term in (4.3) is the material time-derivative of  $T$ . These equations are discretized on an Eulerian grid using a conservative finite difference scheme on a fully staggered grid [Gerya 2010a; Duretz *et al.*, 2011]. The matrix equation for the discretization is then solved with Matlab's direct "backslash" solver. Advection is handled by moving tracer particles, which carry material properties, passively, in the velocity field with a fourth-order Runge-Kutta method over an advection time step  $\Delta t_m$ . This time step is set so that

markers do not move by more than a fraction of the smallest cell size at each iteration. Properties are passed between nodes and particles through bilinear interpolation.

#### 4.2.2. Implementation of visco-elasticity

In order to close the system of conservation equations (4.1–4.3), we assume a Maxwell linear stress-strain relationship of the form

$$\dot{\epsilon}_{ij} = \frac{1}{2\eta}\sigma'_{ij} + \frac{1}{2G}\frac{D\sigma'_{ij}}{Dt} \quad (4.4)$$

This type of material behaves elastically when deformed over a time scale shorter than its Maxwell characteristic time  $\tau_M$

$$\tau_M = \frac{\eta}{G} \quad (4.5)$$

Following *Moresi et al.* [2003], we discretize the Eulerian part of the material derivative

$\frac{D\sigma'_{ij}}{Dt}$  using backward finite difference and a “visco-elastic” time step  $\Delta t$  (referred to as

“computational time step” by *Gerya* [2010a]), yielding

$$\dot{\epsilon}_{ij} = \frac{1}{2\eta}\sigma'_{ij} + \frac{1}{2G}\frac{\sigma'^{(t)}_{ij} - \sigma'^{(t-\Delta t)}_{ij}}{\Delta t} \quad (4.6)$$

Advection and rotation of the deviatoric stresses are handled separately on the particles [*Gerya*, 2010a; *Keller et al.* 2013]. From Equation (4.6), we can rewrite the stress-strain relationship at time  $t$ :

$$\sigma'_{ij} = 2\eta Z \dot{\epsilon}_{ij} + (1-Z)\sigma'^{(t-\Delta t)}_{ij} \quad (4.7)$$

in which we introduce a visco-elastic ratio  $Z$

$$Z = \frac{G\Delta t}{G\Delta t + \eta} \quad (4.8)$$

Upon inserting Equation (4.7) into Equation (4.2), conservation of momentum can be rewritten as

$$\frac{\partial}{\partial x_j}(2\eta Z \dot{\epsilon}_{ij}) - \frac{\partial P}{\partial x_i} + \rho g_i = -\frac{\partial}{\partial x_j}((1-Z)\sigma'^{(t-\Delta t)}_{ij}) \quad (4.9)$$

Symbol	Definition	Value
$v_i$	Velocity field	
$P$	Pressure field	
$\sigma'_{ij}$	Deviatoric stress tensor	
$g$	Gravitational acceleration	9.81 m.s <sup>-2</sup>
$\rho$	Density field	
$\rho_R$	Density of the faulted layer and underlying asthenosphere	3300 kg.m <sup>-3</sup>
$\rho_O$	Density of the ocean layer	1000 kg.m <sup>-3</sup>
$\Delta\rho$	Density contrast between the faulted layer and the overlying fluid layer	2300 kg.m <sup>-3</sup>
$T$	Temperature field	
$c_P$	Heat capacity	
$k$	Thermal conductivity	
$\Delta t_m$	Advection time step	
$\Delta t$	Visco-elastic time step	
$Z$	Visco-elastic ratio	
$G$	Shear modulus	10 GPa
$\nu$	Poisson's ratio	0.5
$E$	Young's modulus	30 GPa
$\eta$	Viscosity field	
$\eta_L$	Viscosity of the faulted layer (in numerical model)	10 <sup>24</sup> Pa.s
$\eta_O$	Viscosity of the ocean layer (in numerical model)	10 <sup>17</sup> Pa.s
$\eta_A$	Viscosity of the asthenosphere (in numerical model)	10 <sup>18</sup> Pa.s
$U$	Full extension rate	
$H$	Faulted layer thickness	
$h$	Fault heave	
$C$	Cohesion	0.01-100 MPa
$\mu$	Friction coefficient	0.6
$\theta$	Dip of the fault	
$E$	Young's modulus	30-100 GPa
$\nu$	Poisson's ratio	0.25-0.5
$\eta_L$	Viscosity of the faulted layer (in numerical model)	10 <sup>24</sup> Pa.s
$\eta_S$	Viscosity of the ocean layer (in numerical model)	10 <sup>17</sup> Pa.s
$\eta_A$	Viscosity of the asthenosphere (in numerical model)	10 <sup>18</sup> Pa.s
$\alpha_E$	Flexural wavelength of the elastic faulted layer	
$\alpha_V$	Flexural wavelength of the viscous faulted layer	
$L$	Width of the numerical model	
$\gamma$	Ratio of the flexural wavelength of the faulted layer to the domain width	
$\gamma_F$	Value of $\gamma$ below which flexure is accommodated	
$U_C$	Extension rate below which flexure is accommodated if the box width is set to 3 $\alpha_E$	

**Table 4-1.** Summary of parameter notations.

In this formulation, the elasticity terms appear as a modified viscosity ( $\eta Z$ ) in the stress divergence term and as a stress history term on the right-hand side. If one chooses a computational time step much shorter than the Maxwell time ( $\Delta t \ll \tau_M$ ), the material effectively behaves elastically ( $Z \sim 0$ ). By setting  $\Delta t \gg \tau_M$ , all elastic effects are turned off ( $Z \sim 1$ ). The computational time step must, however, be resolved by the advection time step ( $\Delta t_m < \Delta t$ ). This framework allows direct comparisons of simulations with and without elasticity.

#### 4.2.3. Implementation of plasticity

In addition to the modifications due to the elastic terms, the effective viscosity  $\eta$  used in Equation (4.9) can also be modified to account for non-linear material creep (power-law rheologies) and plasticity. For simplicity, we restrict ourselves to Newtonian rheologies in this study, however, we account for material plasticity by lowering the effective viscosity wherever the second invariant of the deviatoric stresses ( $\sigma'_{II}$ ) exceeds the yield stress ( $\sigma_y$ ):

$$\eta_{VEP} = \begin{cases} \eta & \text{where } \sigma'_{II} < \sigma_y \\ \frac{\sigma_y}{2\dot{\epsilon}_{II}} & \text{where } \sigma'_{II} \geq \sigma_y \end{cases} \quad (4.10)$$

Accumulated plastic strain is updated at every iteration wherever  $\sigma'_{II} \geq \sigma_y$ , following

$$\epsilon_p^{(t+\Delta t_m)} = \epsilon_p^{(t)} + \Delta t_m \dot{\epsilon}_{II} \quad (4.11)$$

The yield stress is calculated using a Drucker-Prager failure criterion written as a smooth approximation of the Mohr-Coulomb criterion with a friction coefficient  $\mu = 0.6$  and initial cohesion  $C = 100$  MPa. To promote strain localization, cohesion is weakened linearly with accumulated plastic strain [e.g., *Lavier et al.*, 2000] until a critical plastic strain  $\epsilon_{CRIT}$  corresponding to 100 m of slip on a 3 element-wide fault is exceeded. Cohesion cannot decrease below a minimum value of 0.01 MPa. We also implement a healing mechanism [*Poliakov et al.*, 1998], which progressively reduces the accumulated plastic strain over a long time scale  $\tau_H$  such that plastic strains builds up preferentially in regions of sustained localized shear (high strain rate) and heals in regions of diffuse yielding.

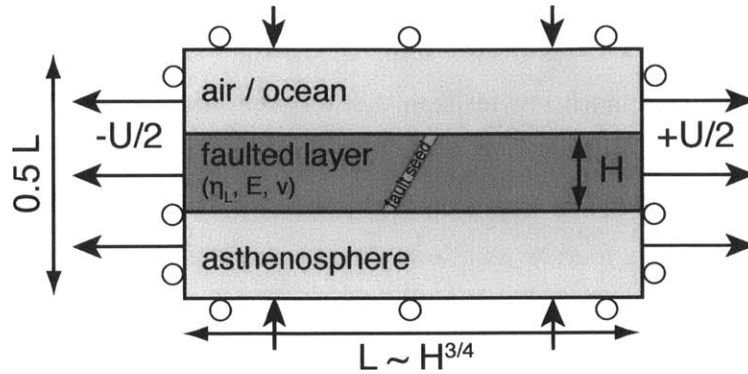


**Figure 4-1.** Schematic setup of our numerical models for fault evolution in an elasto-plastic or a visco-plastic layer sandwiched between two viscous layers. A single 60°-dipping fault is seeded at the first time iteration as a thin band of low-cohesion material, and then allowed to evolve freely as strain localizes along this narrow shear band.

#### 4.2.4. Model setup

The model consists of a brittle lithosphere layer of thickness  $H = 10\text{--}30$  km sandwiched between two weak layers of equal thicknesses representing the overlying ocean [Crameri *et al.*, 2012] and the underlying asthenosphere (Figure 4-1). Horizontal extension is imposed on the two vertical sides at full rates  $U = 0.02\text{--}20$  cm/yr. All boundaries are free slip, with prescribed influx of material through the top and bottom to compensate the flux out the sides. Ocean and rock densities are  $\rho_O = 1000$  kg m<sup>-3</sup> and  $\rho_R = 3300$  kg m<sup>-3</sup>, respectively. The brittle “faulted” layer has a viscosity  $\eta_L = 10^{23}\text{--}10^{25}$  Pa·s, while the ocean and asthenosphere have viscosities of  $10^{17}$  and  $10^{18}$  Pa·s, respectively. The Young’s modulus  $E$  and Poisson’s ratio  $\nu$  are set to  $E = 30$  GPa and  $\nu = 0.5$  (incompressible) throughout the domain, yielding  $G = 10$  GPa. This results in a short Maxwell time in the weak layers (0.3–3 years) and a long Maxwell time in the faulted layer (0.3–30 Myrs). Simulations with an elasto-plastic faulted layer were conducted with a visco-elastic time step  $\Delta t$  equal to  $10^{-3}$  times the Maxwell time of the brittle layer. Simulations with a visco-plastic (no elasticity) faulted layer were carried out with a visco-elastic time step  $\Delta t$  equal to  $10^8$  times the Maxwell time of the faulted layer. In all cases, both the weak ocean and asthenosphere layers behave viscously ( $\Delta t \gg \tau_M$ ).

To ensure a single normal fault develops in the center of the model domain, we initialize the model with a rectangular (three element-wide) “fault seed” dipping at an angle  $\theta_0 = 60^\circ$  throughout the faulted layer, which is the optimal orientation with respect to a friction coefficient of 0.6 in an Andersonian stress state. In the fault seed, plastic strain is set to its critical value  $\epsilon_{\text{CRIT}}$ , and cohesion is weakened accordingly. The box width ( $L$ ) is set to three times the elastic flexural wavelength of the faulted layer  $\alpha_E$ , which is given by

$$\alpha_E = \left( \frac{4D}{\Delta\rho g} \right)^{\frac{1}{4}} \quad (4.12)$$

where  $\Delta\rho = 2300 \text{ kg m}^{-3}$  is the density contrast between the faulted layer and the overlying ocean, and  $D$  is the flexural rigidity of the elastic layer:

$$D = \frac{EH^3}{12(1-\nu^2)} \quad (4.13)$$

The height of the box is  $L/2$ . The grid resolution close to the fault is refined to  $\sim 1$  km or less ( $< 500$  m in cases with  $H < 15$  km), ensuring a mature fault width typically narrower than 3 km. Finally, the plastic strain healing time scale  $\tau_H$  is scaled with the extension rate so that  $U \times \tau_H = 6300$  m. This is done to prevent excessive fault healing in simulations with very slow extension rates.

For simplicity, we do not solve for conservation of energy and ignored any temperature-dependence of material properties. The faulted layer is therefore consistently offset and bent by the growing normal fault. This simplification emphasizes the effect of flexure on fault evolution [*Olive and Behn, 2014*], and allows more direct comparisons with simple thin plate bending models.

### 4.3. Numerical results

Numerical simulations were performed for 29 cases varying different model parameters including  $H$ ,  $U$  and  $\eta_L$ . Model parameters for all simulations are summarized in Table 4-2. Note that the “slow” ( $U \leq 0.2$  cm/yr) elasto-plastic runs require a higher  $\eta_L$  ( $10^{25}$  Pa·s) to ensure that the duration of the entire simulation remains shorter than the Maxwell time of the faulted layer (and the layer therefore remains elastic throughout the run). The observables of interest throughout this study are fault topography, dip and life span.

Run name	Rheology	$\eta_L$ (Pa.s)	H (km)	U (cm/yr)	L (km)	Deformation mode	Second fault breaks?
E10slow	EP	$10^{25}$	10	0.2	84	NA	No
E10ref	EP	$10^{24}$	10	2	84	NA	No
E10fast	EP	$10^{24}$	10	20	84	NA	No
E15slow	EP	$10^{25}$	15	0.2	112	NA	No
E15ref	EP	$10^{24}$	15	2	112	NA	No
E15fast	EP	$10^{24}$	15	20	112	NA	No
E20slow	EP	$10^{25}$	20	0.2	140	NA	No
E20ref	EP	$10^{24}$	20	2	140	NA	No
E20fast	EP	$10^{24}$	20	20	140	NA	No
E30slow	EP	$10^{25}$	30	0.2	190	NA	FS ( $h = 11$ km)
E30ref	EP	$10^{24}$	30	2	190	NA	FS ( $h = 10$ km)
E30fast	EP	$10^{24}$	30	20	190	NA	FS ( $h = 12$ km)
V10veryslow	VP	$10^{24}$	10	0.02	84	PAF	No
V10slow	VP	$10^{24}$	10	0.2	84	PAF	No
V10ref	VP	$10^{24}$	10	2	84	RBD	No
V10fast	VP	$10^{24}$	10	20	84	RBD	No
V15slow	VP	$10^{24}$	15	0.2	112	PAF	FS ( $h = 5.2$ km)
V15ref	VP	$10^{24}$	15	2	112	RBD	No
V15fast	VP	$10^{24}$	15	20	112	RBD	No
V20slow	VP	$10^{24}$	20	0.2	140	PAF	FS ( $h = 4.4$ km)
V20ref	VP	$10^{24}$	20	2	140	RBD	No
V20ref_23	VP	$10^{23}$	20	2	140	PAF	FS ( $h=5.1$ km)
V20fast	VP	$10^{24}$	20	20	140	RBD	No
V20fast_23	VP	$10^{23}$	20	20	140	RBD	No
V30slow	VP	$10^{24}$	30	0.2	190	PAF	FS ( $h = 5.1$ km)
V30ref	VP	$10^{24}$	30	2	190	PAF	FS & HS ( $h = 8.5$ km)
V30ref_23	VP	$10^{23}$	30	2	190	PAF	FS ( $h=4.0$ km)
V30fast	VP	$10^{24}$	30	20	190	RBD	No
V30fast_23	VP	$10^{23}$	30	20	190	PAF	FS & HS ( $h=8.6$ km)
V10ref_23LB	VP	$10^{23}$	10	2	146	PAF	No
V10fast_23LB	VP	$10^{23}$	10	20	260	PAF	No
V20ref_23LB	VP	$10^{23}$	20	2	246	PAF	FS ( $h=4.6$ km)
V20fast_23LB	VP	$10^{23}$	20	20	436	PAF	HS ( $h=6.4$ km)

**Table 4-2.** Summary of numerical simulations. Lithospheric rheology is indicated as EP (elasto-plastic) or VP (visco-plastic). PAF and RBD refer to "Progressively Accommodated Flexure" and "Rigid Block Deformation", respectively.  $h$  indicates the amount of heave accumulated by the initial fault when a new fault breaks. FS = Footwall Snapping. HS = Hanging wall snapping, following the definition of *Lavier et al.* [2000].

For systematic comparisons between runs we consider a simulation to be complete when the total throw on the fault is equivalent to the thickness of the brittle layer  $H$ , or when a new fault has spontaneously localized in the footwall or hanging wall of the initial fault.

#### **4.3.1. Fault-induced topography**

In our simulations, the relief associated with fault growth systematically features a short wavelength ( $\sim h$ ) component corresponding to the fault scarp, and a longer wavelength decay of topography away from the fault. In all the elasto-plastic cases, the latter component is well described as the flexure of a thin elastic plate under gravity [e.g., *Weissel and Karner, 1989; Olive and Behn, 2014*], with deflection that is anti-symmetric about the fault and small at distances  $> \sim 1.5$  flexural wavelengths away from the fault (Figure 4-2). In addition, in all elasto-plastic runs topography appears to be solely a function of the amount of horizontal extension ( $h$ ) accommodated on the fault, and is largely insensitive to the rate of extension. By contrast, in the visco-plastic simulations without elasticity, the long-wavelength topography is viscously supported but mimics flexure with a flexural wavelength that is strongly sensitive to the extension rate. To allow systematic comparisons among visco-plastic runs, we adopt the following convention. We consider the model width to adequately accommodate the flexural signal when the vertical displacement on the edges of the box is less than 7.5% of the fault throw. In practice, this means that the relief is able to sufficiently decay away from the fault scarp within the model domain. None of the visco-plastic simulations meet this criterion at small heaves (less than 1 km) or for  $U \geq 2$  cm/yr and  $\eta_L = 10^{24}$  Pa·s (Figure 4-2, panel C2 and C3). For these situations the topography is flat on either side of the fault, as if the fault was offsetting two rigid blocks. However, for all runs carried out at  $U \leq 0.2$  cm/yr, the footwall and hanging wall bend on progressively shorter length scales as

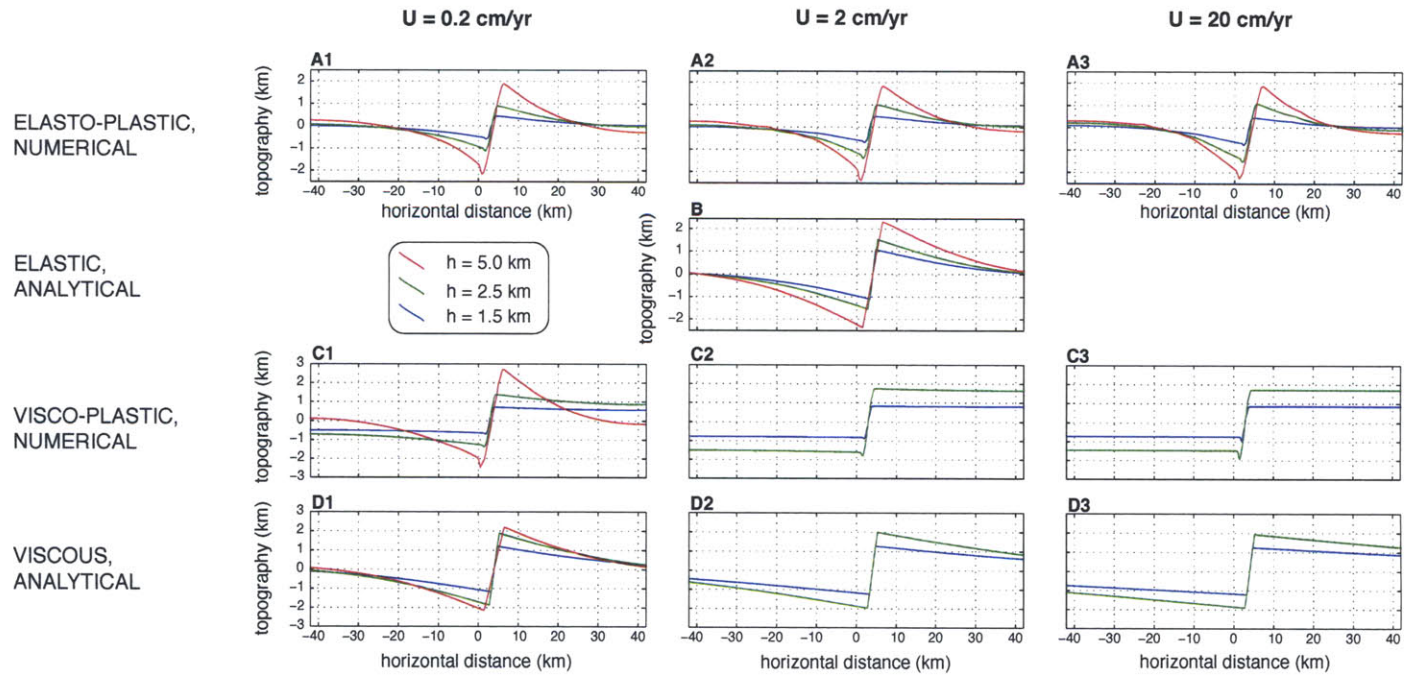


**Figure 4-2.** Topography induced by 1.5, 2.5, and 5 km of horizontal offset on a normal fault growing at different extension rates in a 10-km thick layer of varying rheology: (A) elasto-plastic (numerical model), (B) purely elastic (analytical, with a displacement discontinuity at the fault), (C) visco-plastic (numerical) and (D) purely viscous (analytical).

extension proceeds and the flexural signal is eventually accommodated within the model domain. This is particularly apparent in panel C1 of Figure 4-2, where the topography is flat on both sides of the fault scarp after 1.5 km of extension, but later develops significant curvature. After 5 km of extension the decay of topography away from the fault has become pronounced.

In the following, we refer to these two modes of deformation as "rigid block deformation" (RBD) and "progressively accommodated flexure" (PAF). Figure 4-3 highlights the transition between the two styles of deformation, which appears weakly sensitive to layer thickness. Specifically, the transition corresponds to a critical extension rate  $U_C$  between 0.2 and 2 cm/yr. When reducing the faulted layer viscosity by a factor of 10 ( $\eta_L = 10^{23}$  Pa·s), this critical rate appears to increase by an order of magnitude (between 2 and 20 cm/yr).

#### **4.3.2. Fault dip**

In the elasto-plastic cases, all faults are found to rotate rapidly to a shallower dip. To assess the effect of lithospheric rheology on rotation kinematics, we measured the evolving dip of the seeded fault throughout all the runs by visually fitting a line through the region of greatest accumulated plastic strain. In all elasto-plastic simulations, we measured faster rotation rates (i.e., change in angle per unit of accumulated heave) in the thinner brittle layers, which is consistent with the mechanical models presented in Chapters 2 and 3. However, for a given layer thickness, the rotation rate expressed in terms of total fault heave  $\partial\theta/\partial h$  does not change with extension rate  $U$  in a systematic manner (Figure 4-4A).

In visco-plastic layers, no significant fault rotation occurs at fast extension rates or higher lithosphere viscosity; the fault retains a steep angle while offsetting the rigid

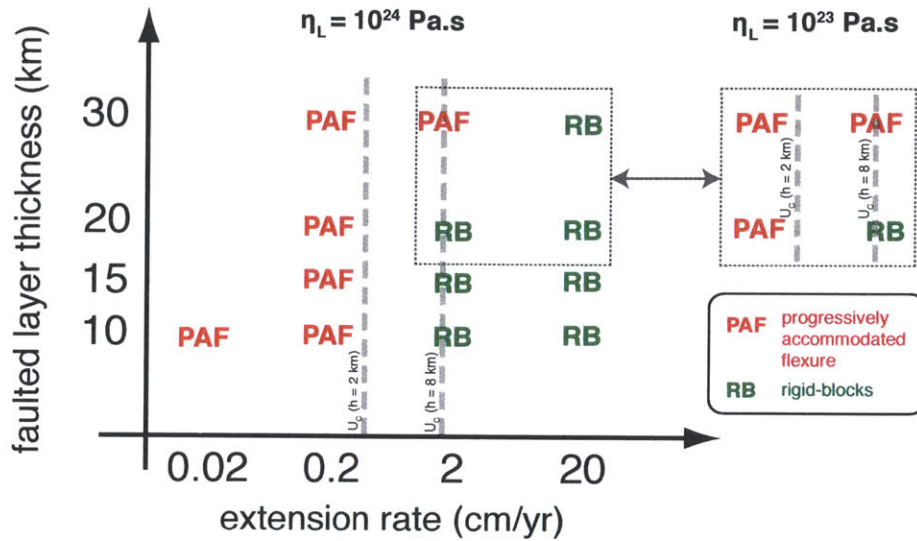


**Figure 4-3.** Summary of the modes of deformation observed in our numerical visco-plastic models, plotted as a function of faulted layer thickness  $H$  and full extension rate  $U$ . The "progressively accommodated flexure" (PAF) mode corresponds to cases where pronounced flexure-like topography develops either immediately or with time in the calculations such that the vertical displacement the model edge (measured from its initial position) becomes lower than 7.5% of the fault throw. By contrast, in "rigid block deformation" (RBD) mode, the footwall and hanging wall blocks are vertically offset with little to no internal deformation. The vertical dashed lines indicate the critical extension rates bounding the two modes as calculated using Equation (4.18) assuming fault heaves of 2 and 8 km. All runs correspond to a layer viscosity of  $\eta_L = 10^{24}$  Pa·s, except those shown in the inset, which are carried out with  $\eta_L = 10^{23}$  Pa·s.

footwall and hanging wall (e.g., cases with  $H = 10$  km and  $U \geq 2$  cm/yr in Figure 4-4B). An interesting transition occurs in simulations with slower extension rates. With  $H = 10$  km and  $U = 0.2$  cm/yr, the fault initially retains a steep dip of  $\sim 58^\circ$  over the first 2.5 km of horizontal extension. Then, rotation suddenly initiates at a rate of about  $5^\circ/\text{km}$  (Figure 4-4B). By contrast, in the  $U = 0.02$  cm/yr case, fault rotation starts immediately from the onset of fault growth ( $h \sim 0$ , Figure 4-4B) at a rate of about  $2.7^\circ/\text{km}$ . In summary, all visco-plastic simulations that evolved in the RBD mode featured no significant fault rotation, whereas those that evolved in the PAF mode saw an onset of fault rotation either immediately or at some time after the onset of extension.

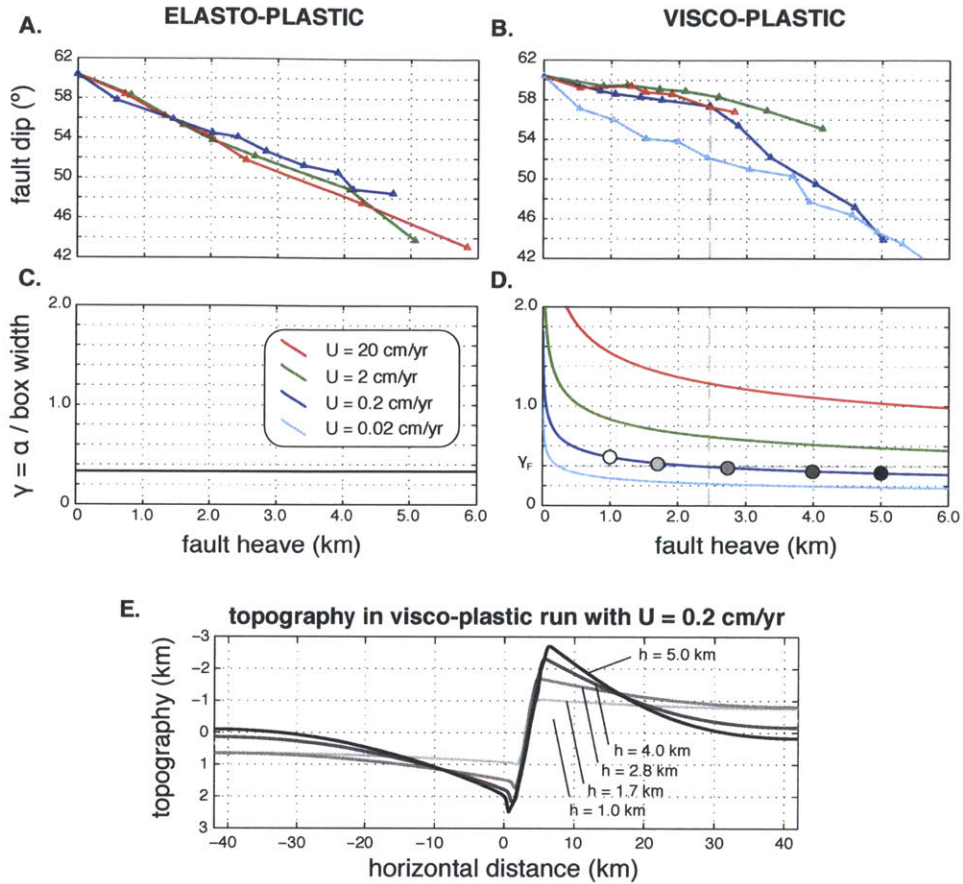


**Figure 4-4.** Kinematics of fault rotation in a 10 km-thick (A) elasto-plastic and (B) visco-plastic lithosphere for different extension rates (color code). Panels C and D show the flexural wavelength of the faulted layer normalized by the width of the box for a 10 km thick purely elastic (C) and purely viscous (D) layer, as predicted analytically (Equation 4.16). In visco-plastic numerical simulations, fault rotation begins when the ratio of the long-wavelength (flexural) topography and box width becomes lower than  $\gamma_F \sim 0.4$ . Panel E shows the topography from visco-plastic run V10slow (dark-blue curves in panels B and D) for different amounts of horizontal offset on the fault, indicated as circles on panel D (gray color code).

### 4.3.3. Fault life span

To characterize the long-term evolution of the faults, we define two fault life-span regimes following *Lavier et al.* [2000]: (1) a “prolonged slip” regime, in which the seeded fault remains active long enough to offset the brittle layer by its entire thickness  $H$

in the vertical direction, and (2) a “limited slip” regime, in which a new fault breaks the hanging wall or the footwall (“hanging wall / footwall snapping” in *Lavier et al.* [2000]). In these runs we keep track of the total amount of horizontal extension accommodated on the initial fault when the new fault forms, i.e., when accumulated plastic strain starts to heal on the initial fault and build up on the new fault.

In elasto-plastic layers, the transition between the life span regimes occurs at a brittle layer thickness  $H$  between 20 and 30 km and appears insensitive to extension rate (Figure 4-5). In layers thinner than 20 km, no second fault forms, but for  $H = 30$  km, a new normal fault systematically breaks through the footwall, starting from the base of the brittle layer, which flexes in tension. This result is consistent with findings of previous studies that larger offsets occur on an individual fault in thinner elasto-plastic layers [*Buck, 1993; Lavier et al., 2000; Lavier and Buck, 2002; Behn and Ito, 2008*].

The transition between the two life span regimes is more complex in the visco-plastic simulations (Figure 4-6). A striking observation is that whenever the lithosphere behaved as rigid blocks (Figure 4-3, as defined in Section 4.3.1) slip on the fault was prolonged, and no second fault initiated. In cases where the lithosphere deformed dynamically (and flexure was progressively accommodated), both life span regimes occurred. For example, in the visco-plastic run with  $H = 10$  km and  $U = 0.2$  cm/yr the long wavelength lithospheric flexure signal is accommodated within the model domain, but no new fault localizes. By contrast, when  $H = 15$  km and  $U = 0.2$  cm/yr the lithosphere deforms in the PAF mode, and we see a new fault develop in the footwall block after 5.2 km of extension on the initial fault (Figure 4-6 B1).

In all runs evolving in the PAF mode, thicker layers promote the formation of second faults, and thinner layers favor prolonged slip on the initial fault. The maximum offset achieved by the initial fault in the “limited slip” regime appears weakly sensitive to layer thickness, but strongly sensitive to extension rate, with larger offsets attained at faster extension rates. Most new faults initiate through footwall snapping, except in the fastest extension rate cases of the “limited slip” regime, where the initial fault was abandoned in favor of two new faults that broke simultaneously in the footwall and hanging wall (runs V30ref and V30fast\_23 in Table 4-2). Finally, we found that reducing the faulted layer viscosity by a factor of 10 ( $\eta_L = 10^{23}$  Pa-s) shifted the life span regime

transition toward faster extension rates (Figure 4-6), suggesting that decreasing  $\eta_L$  by an order of magnitude is equivalent to decreasing  $U$  by an order of magnitude.

To summarize our numerical results, we find that fault topography, dip evolution and life span in elasto-plastic layers are essentially insensitive to extension rate, and closely follow the predictions of previous studies [Lavier *et al.*, 2000; Behn and Ito, 2008; Olive and Behn, 2014]. By contrast, in simulations that treat the lithosphere as a visco-plastic solid, the wavelength of fault-induced dynamic topography decreases over time. Under certain conditions, a fast extension rate (and / or a high layer viscosity) produces no significant decay of topography away from the fault within the numerical domain. In these cases the initial fault: (1) offsets the lithosphere in two rigid blocks, (2) retains its initial dip, and (3) undergoes prolonged slip independent of brittle layer thickness. In the following section, we use a simple scaling approach to quantitatively explain the extension rate-dependence of the visco-plastic simulations. By doing so, we aim to determine what controls the style of deformation (PAF vs. RBD) and fault life span in simulations with a visco-plastic lithosphere.

#### 4.4. Semi-analytical approach: simple scalings to guide the interpretation of numerical simulations

##### 4.4.1 Fault-induced topography

In all our elasto-plastic simulations topography grew in a rate-independent manner, suggesting that topography is driven entirely by elastic flexure. The fault-induced, flexural topography  $w^T(x)$  is well-explained by the thin plate solution of *Weissel and Karner* [1989] and detailed in Chapter 2:

$$w^T(x, h) = \frac{1}{4} \alpha_E \tan \theta \left( f \left| \frac{x - h/2}{\alpha_E} \right| - \left( f \left| \frac{x + h/2}{\alpha_E} \right| \right) \right) \quad (4.14)$$

with  $f$  defined as

$$f(x) = e^{-x} (\sin x - \cos x) \quad (4.15)$$

In the numerical models the faulted layer bends on a wavelength equal to or shorter than  $\alpha_E$  (Figure 2B, Equation 4-12). Cases where the actual bending wavelength is less than  $\alpha_E$  are caused by diffuse plastic yielding of the plate.

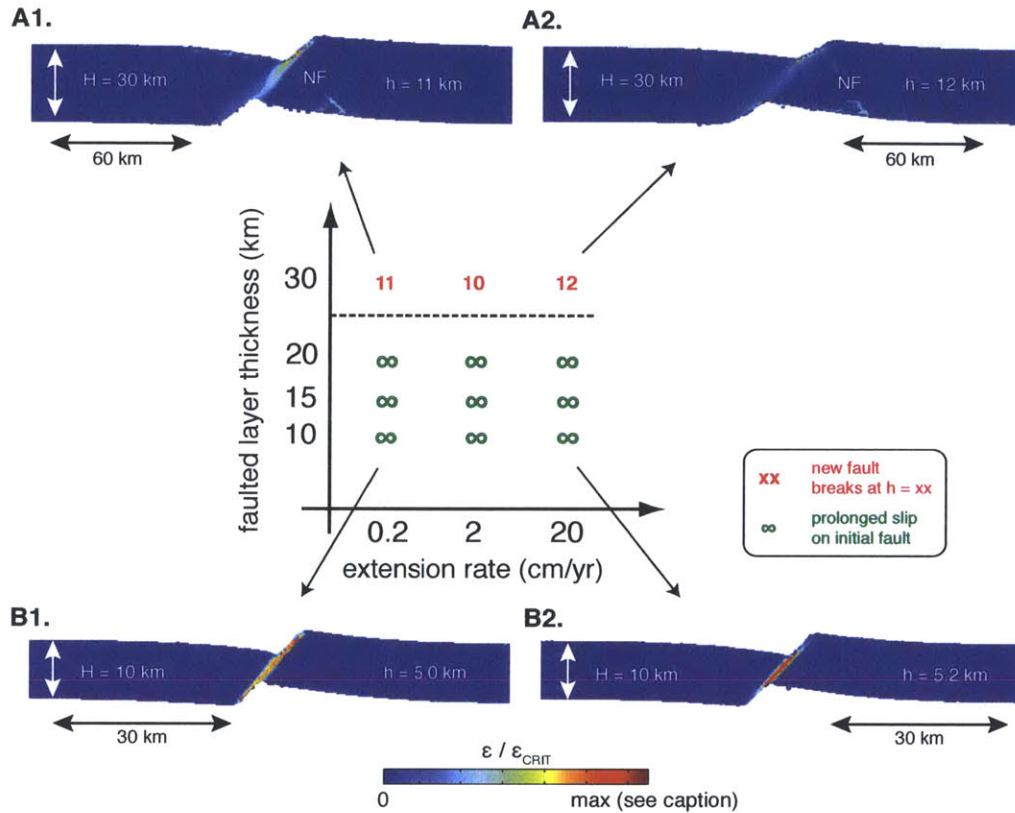


**Figure 4-5.** Regime diagram for the life span of normal faults in elasto-plastic lithosphere as a function of faulted layer thickness  $H$  and full extension rate  $U$ . The "prolonged-slip" regime describes the case in which the initially seeded fault accumulates enough extension to offset the entire lithosphere; the "limited slip" regime is when a second fault (NF) begins to form on the hanging wall or footwall of the first fault. Numbers denote the maximum horizontal extension accommodated on the initial fault. The black dashed line marks the approximate location of the regime transition. Insets A1, A2, B1 and B2 show model snapshots of accumulated plastic strain  $\epsilon_p$  normalized by the critical weakening strain  $\epsilon_{CRIT}$ . Maximum values of  $\epsilon_p / \epsilon_{CRIT}$  are (A1) 4.3, (A2) 4.0, (B1) 3.9, (B2) 26.2.

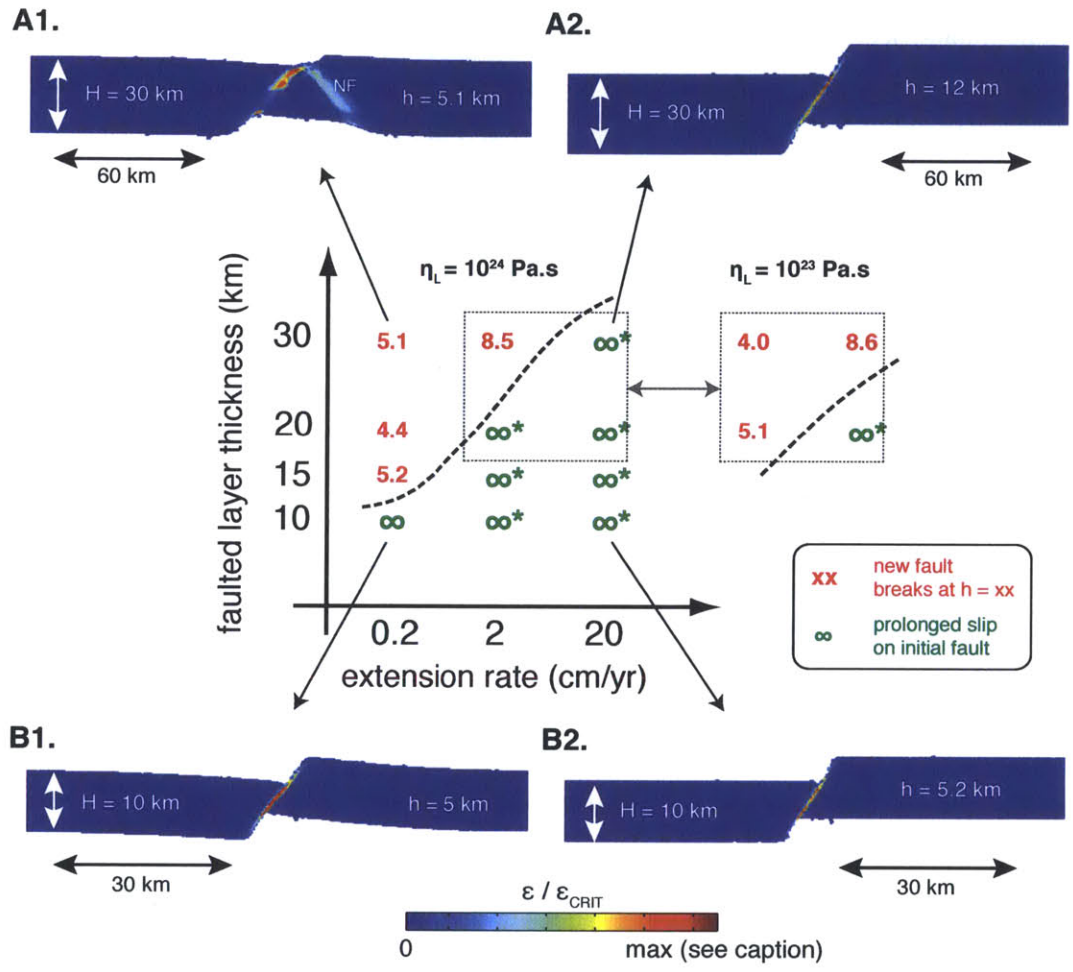


**Figure 4-6.** Same as Figure 4-5, but for a visco-plastic lithosphere. All runs correspond to a layer viscosity of  $\eta_L = 10^{24}$  Pa·s, except those shown in the inset to the right, which are performed with  $\eta_L = 10^{23}$  Pa·s. Maximum values of  $\epsilon_P / \epsilon_{CRIT}$  in the model snapshots are (A1) 15, (A2) 90, (B1) 38, (B2) 42. An asterisk near the infinity sign denotes a model run that evolved in the "rigid blocks deformation" mode (See Figure 4-3).

We note that in our numerical elasto-plastic models plastic yielding does not induce significant rate-dependent deformation.

Our numerical results indicate that in the visco-plastic simulations the length scale of topographic decay is not always accommodated within the numerical domain. In cases where the dynamic topography was too broad for the domain size, topography appeared flat on both sides of the fault, and the footwall and hanging wall effectively behaved as two rigid blocks. The flat topography is likely due to the free-slip boundary condition allowing free uplift / subsidence along the sides of the box. However, a no-slip boundary condition is not preferable, because pinning the edges of the layer often results in spurious strain localization along the sides of the model domain. In simulations carried out at a lower extension rate, topography initially appears flat but eventually starts to decay away from the fault scarp. In this "progressively accommodated flexure" mode of deformation the characteristic length scale of topographic decay appears to decrease with time or increasing extension, as illustrated in panel E of Figure 4-4.

To understand the transition between the deformation accommodated by "progressively accommodated flexure" versus "rigid block deformation" (Figure 4-3), we derive an analytical solution for fault growth in a thin viscous plate. This is effectively a re-derivation of the classic *Weissel and Karner* [1989] model with a viscous (Newtonian) rheology [*Biot*, 1961; *Turcotte and Schubert*, 2002] and is detailed in Appendix 4.1. The key result is that flexure in a viscous plate is well described by an elastic model (Equation 4.14) with an effective flexural wavelength  $\alpha_v$  that decreases over time (i.e., with increasing fault heave) and depends on extension rate:

$$\alpha_v(h) = \left( \frac{\eta_L U H^3}{\Delta \rho g h} \right)^{\frac{1}{4}} \quad (4.16)$$

The flexural wavelength corresponds to the length scale of topographic decay away from the fault scarp. The analytical result of a decreasing  $\alpha_v$  with increasing extension is in agreement with the observation of topographic decay becoming more and more pronounced throughout the PAF runs. We postulate that runs that show "rigid block deformation" have parameters such that  $\alpha_v$  is never fully accommodated within the horizontal extent of the domain during the simulation.

To quantify this assumption, we introduce a parameter  $\gamma$ , which defines the ratio of the flexural wavelength of the faulted layer to the width of the numerical domain. This ratio systematically decreases with increasing extension in a viscous plate (Figure 4-4D). It is therefore possible that a visco-plastic run would start with too large a  $\gamma$  ratio to feature topographic decay, but would develop it if  $\gamma$  has time to become sufficiently small during the simulation (as seen in Figure 4-4E). We next define a critical ratio  $\gamma_F$  below which flexure is accommodated and attempt to estimate it. For example, a critical ratio  $\gamma_F = 0.5$  means that one flexural wavelength must be accommodated on each side of the fault within our model domain. In all our elasto-plastic simulations the domain width is set to  $3\alpha_E$ , though as noted above, diffuse plasticity can locally decrease the effective flexural wavelength resulting in  $\gamma \leq 1/3$  (Figure 4-4C). Elastic flexure is well expressed in all our elasto-plastic simulations, therefore  $\gamma_F$  is likely greater or equal to  $1/3$ . For simplicity we will assume  $\gamma_F = 0.5$  in the rest of Section 4.4.1, but will improve our estimate in Section 4.4.2. The condition for accommodating flexure in our visco-plastic simulations can be written

$$\alpha_v \leq \gamma_F L \quad (4.17)$$

Using Equations (4.12), (4.16), and the fact that  $L = 3\alpha_E$ , we can rewrite Equation (4.17) as:

$$U \leq (3\gamma_F)^4 \frac{Eh}{3\eta_L(1-\nu^2)} = U_C \quad (4.18)$$

This relation shows that for a given fault heave,  $h$ , viscous flexure can only be accommodated within the numerical domain if the extension rate is less than a critical rate  $U_C$ , which does not depend on the faulted layer thickness.

Equation (4.18) can be used to predict the transition between models that deform by PAF versus RBD. For a faulted layer of viscosity  $\eta_L = 10^{24}$  Pa·s, Equation (4.18) predicts the critical extension rate to be 0.4 cm/yr and 1.7 cm/yr assuming a fault heave of 2 and 8 km, respectively, and  $\gamma_F = 0.5$  (vertical dashed lines in Figure 4-3). These predictions are consistent with the numerical results, which yielded a critical rate between 0.2 and 2 cm/yr for fault heaves less than 10 km. Further, Equation (4.18) readily explains the increase in the critical rate  $U_C$  by an order of magnitude when the layer viscosity is decreased by an order of magnitude ( $\eta_L = 10^{23}$  Pa·s inset in Figure 4-3).

However, numerical experiments carried out with a 30 km thick brittle layer yielded a greater  $U_C$  (between 2 and 20 cm/yr) than simulations with thinner layers (Figure 4-3), even though according to Equation (4.18), lithospheric thickness,  $H$ , should have no effect on  $U_C$ . We attribute this to the fact that if no new fault is to develop in a thick layer, the original fault will be able to accumulate more heave, further decreasing the viscous flexural wavelength (Equation 4.16), and eventually allowing the flexural wavelength to be accommodated in the model domain.

We can also use the scalings above to determine the minimum box size required to fully accommodate viscous flexure for a given set of extension parameters. To demonstrate this we take four simulations that produced rigid block deformation with the original domain size and re-run them in a wider domain (runs ending in "23LB" in Table 4-2). We set the model width to two viscous flexural wavelengths (Equation 4.16) calculated at a fault heave of 100 m, which is the critical slip required to fully weaken the fault zone (see Section 4.2.3). If  $\gamma_F$  is equal to 0.5, the model width should be sufficient to ensure that a simulation will evolve in the "progressively accommodated flexure" mode. More precisely, bending should be accommodated by the time the fault has fully localized. To avoid very large domain sizes, we choose a faulted layer viscosity  $\eta_L = 10^{23}$  Pa·s and use wider boxes for runs carried out at faster extension rates (Table 4-2). In these simulations, the height of the box is no longer set to half of the width, but is chosen such that the ocean layer, rock layer and asthenosphere are of commensurate thickness. All these runs produce a well-expressed decay of topography away from the fault scarp, (i.e., evolve in the PAF mode) and therefore support (1) the relevance of our analytical scalings, and (2) the assumption that  $\gamma_F = 0.5$ . As an example, Figure 4-7 shows the difference in topography between two identical visco-plastic runs ( $U = 20$  cm/yr,  $H = 20$  km) after 5 km of extension, except one simulates a 140 km-wide box and the other a 436 km-wide box (with  $L$  chosen based on the scalings above). Pronounced flexure in the wider-box runs produces smaller fault throws for the same amount of heave. Models of adequate width also show fault rotation, which is discussed in detail below.

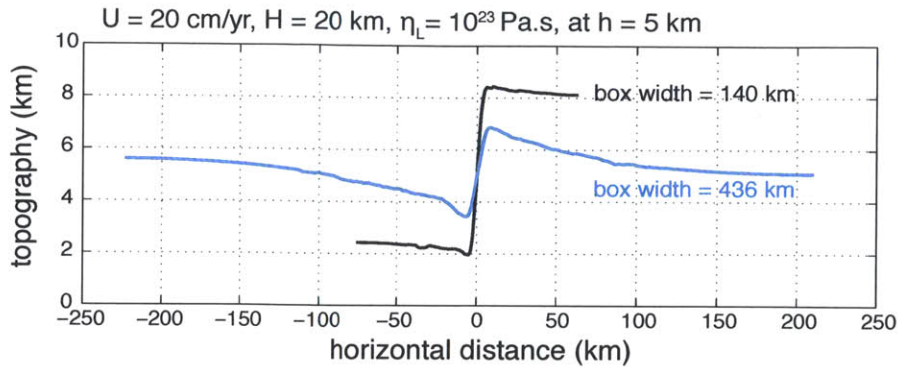


**Figure 4-7.** Model topography obtained in visco-plastic simulations V20fast\_23 and V20fast\_23LB (Table 4-2) after 5 km of extension at 20 cm/yr in a 20 km-thick layer with  $\eta_L = 10^{23}$  Pa·s. Simulations were performed in a 140 km-wide box (black curve) and a 436 km-wide box (blue curve). The wider box can fully accommodate the decay of viscously supported topography away from the fault.

#### 4.4.2 Fault rotation

In all elasto-plastic simulations, the initially steep fault rotates rapidly towards a shallower dip in the 30–45° range (Figure 4-8A). We interpret this behavior as passive advection of the fault plane in the displacement field induced by flexure of the footwall and hanging wall, which simultaneously acts to minimize the total work done by the system, as proposed in Chapters 2. In Chapter 3, we demonstrated that with this mechanism, the fault rotation rate ( $\partial\theta/\partial h$ , in degrees per unit of accumulated extension) scales as the inverse of the flexural wavelength of the faulted layer. This model thus accounts for the lack of fault rotation in runs where visco-plastic lithosphere behaves as rigid-blocks (i.e., very large flexural wavelength leading to very slow rotation rates). However, as soon as the flexural wavelength decreases with heave such that it becomes accommodated within the model domain, rotation can proceed. This is well illustrated by visco-plastic simulation V10slow, with  $H = 10$  km and  $U = 0.2$  cm/yr (Table 4-2). In this simulation, the onset of rotation occurs after 2.5 km of extension, which is roughly the time when topography starts to feature significant off-fault decay (Figure 4-4E). This is also consistent with the offset at which  $\gamma$  decreases below 0.4 based on our analytical scalings (Figure 4-4D).

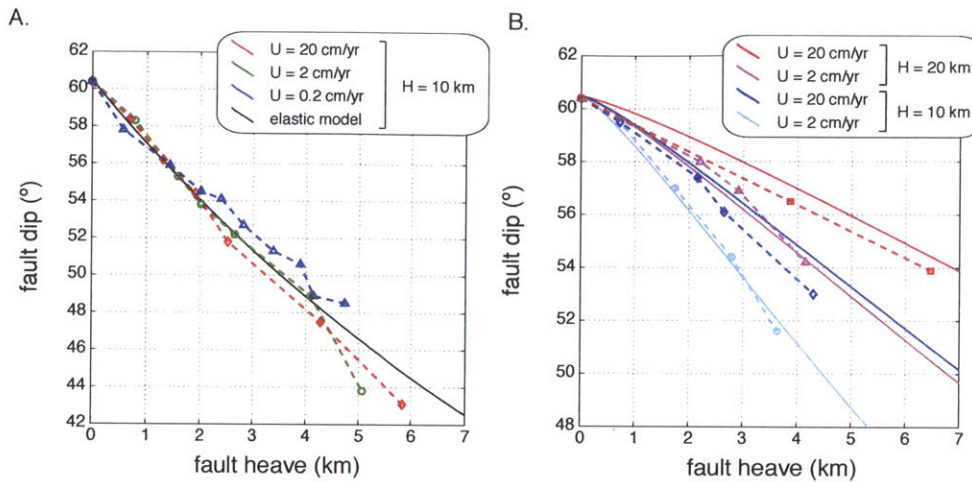


**Figure 4-8.** Kinematics of fault rotation in (A) elasto-plastic and (B) visco-plastic layers where the box width encompasses the flexural wavelength (Table 4-2, visco-plastic runs ending in "23LB"). The dots and dashed lines indicate numerical results and the solid lines refer to analytical models (Section 4.4.2). The color code corresponds to varying extension  $U$  rates and faulted layer thicknesses  $H$ .

Interestingly, in the V10veryslow simulation with  $U = 0.02$  cm/yr,  $\gamma$  becomes smaller than 0.4 after only  $\sim 200$  m of extension (Figure 4-4D). In this simulation, fault rotation immediately follows the onset of extension ( $h \sim 0$ , Figure 4-4B), suggesting that the value of  $\gamma_F = 0.4$  may be appropriate over a range of extension rates.

For a more quantitative understanding of rotation kinematics in a viscous faulted layer, we focus on the four simulations carried out in wide boxes (Table 4-2). In these runs, the onset of fault rotation is immediate, and the kinematics of rotation depend on the extension rate, with faster extension and thicker faulted layers coinciding with slower rotation rate per unit heave (Figure 4-8B). To explain this observation, we incorporate the time-dependent flexural wavelength derived in Appendix 4.1 into the kinematic fault rotation model of Chapter 3. As described in Appendix 3.1, the fault rotation rate in degrees per unit time should roughly scale with the average rotation rate of the near-fault displacement field,  $\dot{\Omega}$ :

$$\frac{\partial \theta}{\partial t} \sim -\dot{\Omega} \quad (4.19)$$

To first order, the main source of rotation in the flexural displacement field is the lateral gradient of vertical motion, which is maximal at the fault (equal to  $0.5U \tan \theta$ ), and becomes negligible a fraction ( $\Phi$ ) of the flexural wavelength  $\alpha$  away from the fault.  $\Phi \alpha$  can thus be thought of as the lever arm involved in the rotation of the fault. We therefore write

$$\dot{\Omega} \sim \frac{1}{2} \frac{\partial v_z}{\partial x} \sim \frac{1}{4} \frac{U \tan \theta}{\Phi \alpha} \quad (4.20)$$

Plugging Equation (4.20) into Equation (4.19) with the constraint  $h = U t$  yields

$$\frac{\partial \theta}{\partial h} = -\frac{\tan \theta}{4\Phi \alpha} \quad (4.21)$$

which can be integrated to yield

$$\theta = \sin^{-1} \left( \sin \theta_0 \exp \left( -\frac{1}{4\Phi} \int_0^h \frac{dh}{\alpha(h)} \right) \right) \quad (4.22)$$

With these assumptions, we can predict the evolution of fault dip as a function of heave for a given extension rate. In a purely elastic lithosphere, the flexural wavelength is a constant given by Equation (4.12), and Equation (4.22) simplifies to

$$\theta = \sin^{-1} \left( \sin \theta_0 \exp \left( -\frac{h}{4\Phi \alpha_E} \right) \right) \quad (4.23)$$

By contrast, for a purely viscous lithosphere, we substitute Equation (4.16) into Equation (4.22) to yield

$$\theta = \sin^{-1} \left( \sin \theta_0 \exp \left( -\frac{1}{5\Phi} \left( \frac{\Delta \rho g}{\eta_L U H^3} \right)^{\frac{1}{4}} h^{\frac{5}{4}} \right) \right) \quad (4.24)$$

Following the approach of Chapter 3, we assume a scaling factor  $\Phi = 0.25$ , which was empirically found to accurately predict fault rotation rates in elasto-plastic simulations across a range of faulted layer thicknesses. A value of 0.25 means that the lever arm associated with fault rotation corresponds to about a fourth of the effective flexural wavelength of the faulted layer (Equation 4.20). Figure 4-8 shows the comparison

between our analytical prediction of fault rotation and numerical results. The rate-independent rotation observed in elasto-plastic runs is well explained by our simple elastic model (Figure 4-8A); it also indicates that the diffuse plasticity outside of the fault zone does not significantly influence fault rotation. The analytical model for fault rotation in viscous layers also does an excellent job predicting the rotations in visco-plastic models that were wide enough to encompass the flexural wavelengths. The analytic model captures the slower rotation with heave associated with thicker layers and faster extension, both of which produce larger flexural wavelengths. This agreement between the numerical and analytical models strongly supports our initial assumption that fault rotation is driven primarily by the flexural displacement field, and therefore becomes extension rate-dependent when the lithosphere is assigned a visco-plastic rheology.

#### **4.4.3 Fault life span**

The control of layer thickness  $H$  on fault life span in elasto-plastic layers is well explained by the build-up of elastic (rate-independent) stresses associated with lithospheric flexure and topographic growth [Forsyth, 1992; Buck, 1993; Lavier *et al.*, 2000; Olive and Behn, 2014; Olive *et al.*, 2014b]. Stresses accumulate more rapidly with fault offset in thicker layers, and trigger earlier initiation of new faults in the adjacent lithosphere. Interestingly, while plasticity limits the build-up of stresses and allows infinite fault growth in thin layers, it does not produce significant extension rate-dependence of our numerical results, even though diffusely yielded portions of the lithosphere locally behave viscously.

The tendency of faster extension rates to promote prolonged slip in visco-plastic cases may seem counter-intuitive given that faster extension and higher  $\eta_L$  produce greater flexural stresses within the faulted layer (Equation 4.7). We interpret this to be a consequence of the model domain not adequately encompassing the flexural wavelength, given that  $\alpha_v$  is greater in rapidly extending, high-viscosity layers. When the footwall and hanging wall blocks are rigidly offset they do not develop significant flexural stresses due to the lack of bending, which would otherwise promote the formation of new faults. However, in visco-plastic simulations carried out with wide boxes (Table 4-2, runs ending in "23LB"), a new fault broke in all the 20 km-thick lithosphere cases regardless

of extension rate. This suggests that if the numerical domain is sufficiently wide to encompass the viscous flexural wavelength, the regime transition is less sensitive to extension rate, and more closely resembles the elasto-plastic cases. We note, however, that within the "limited slip" regime, faster extension rates result in a longer life span of the initial fault both in narrow (Figure 4-6) and wide box simulations (Table 4-2). One possible explanation is that the viscous flexural wavelength will always be larger than the model domain at the beginning of a simulation when  $h = 0$  km (Equation 4-16; Figure 4-4D). This could delay or hinder the build-up of flexural stresses and artificially prolong fault life span, even though more rapid extension tends to generate higher viscous stresses. In short, the complex transition between the "prolonged slip" and "limited slip" regimes in visco-plastic layers (Figure 4-6) can be thought of as the convolution of (1) the lithospheric thickness control characteristic of both elasto-plastic and visco-plastic cases, and (2) spurious effects arising when the model domain cannot fully accommodate the evolving wavelength of viscous flexure.

#### **4.5. Concluding remarks**

This study addresses the differences between numerical simulations of tectonic rifting in an elasto-plastic vs. a visco-plastic lithosphere. We focus on the long-term evolution of individual normal faults, which constitute the building blocks of extensional plate boundaries. We have shown that elasticity promotes rate-independent deformation resulting in rift geometries (topography and fault rotation) that only depend on the total amount of extension and not on the extension rate. Specifically, fault life span, and therefore the style of extensional faulting (multiple short-offset faults vs. long-lived detachments) are also unaffected by extension rate in elasto-plastic simulations, however they are strongly controlled by lithospheric thickness.

We have shown that under certain conditions, a visco-plastic rheology can reproduce the qualitative behavior of elasto-plastic simulations, i.e., faults that rotate rapidly after they localize and remain active longer in thinner layers. This occurs when the numerical domain is wide enough to accommodate 2 to 2.5 times ( $\gamma_F = 0.4-0.5$ ) the flexural wavelength of the viscous layer at fault heaves equal to the amount of slip necessary to fully weaken the fault. However, we find that fault rotation rate (Figure 4-8)

and life span (Table 4-2) depends on the extension rate applied to the visco-plastic simulations, even when viscous flexure is fully accommodated in the domain. This rate-dependence is never observed in the elasto-plastic runs.

The elasto-plastic prediction of rate-independent fault evolution is most relevant to real continental rift and mid-ocean ridge settings, given that the characteristic topographic signature of elastic flexure is found near normal faults over a wide range of spreading rates [e.g., *Weissel and Karner*, 1989; *King et al.*, 1988; *Armijo et al.*, 1996; *Schouten et al.*, 2010]. Further, the differences in rift morphology across spreading rates are generally well explained by rheological factors (i.e., lithospheric thickness) and external controls such as magmatism [*Buck et al.*, 2005; *Behn and Ito*, 2008; *Ito and Behn*, 2008] and surface processes [*Olive et al.*, 2014b].

Some authors have proposed that extension rate itself may exert a rheological control on mid-ocean ridge morphology and the development of transform faults [*Gerya*, 2010b; 2013; *Püthe and Gerya*, 2013]. However, this suggestion is supported by numerical models that do not include elasticity, and should therefore be examined in light of our new results and scalings. In the case of the *Püthe and Gerya* [2013] study, the moderate viscosity ( $\sim 10^{22}$  Pa·s) and thickness ( $\sim 10$  km) of the lithosphere guarantees that the viscous flexural wavelength of the lithosphere be rapidly accommodated within the model domain ( $\sim 100$  km). These simulations can therefore produce topography that qualitatively resembles elastic flexure, yet the results of the present study raise questions as to what extent the prediction of spreading rate-dependent ridge morphology results from the use of a visco-plastic approximation to the natural rheology of oceanic plates.

In a broad sense, the analogies between elasto-plastic and visco-plastic models result from mathematical similarities between linear elasticity (stress proportional to strain) and Newtonian viscosity (stress proportional to strain rate). However, these similarities are at risk of breaking down in a problem-dependent manner when key parameters such as lithospheric thickness or velocity boundary conditions are changed. Further, the incorporation of elasticity in a numerical model can significantly affect the spatial and temporal evolution of deviatoric stresses, which in turn control the onset of strain localization. Elasticity is therefore especially important in long-term geodynamic simulations that involve faults forming in a sequence and significantly deforming the

surrounding lithosphere. Happily, visco-elasto-plastic codes are becoming widely available to the long-term tectonics community [e.g., *Cundall*, 1989 (FLAC); *Gerya and Yuen*, 2003; 2007; *Gerya*, 2010a (I2ELVIS and I3ELVIS); *Moresi et al.*, 2007 (Underworld); *Choi et al.*, 2008 (SNAC); *Choi et al.*, 2013 (DynEarthSol2D); and Chapter 6 of this thesis (HiPStER). Possible improvements to these codes include the routine incorporation of compressible elasticity and the development of new schemes to keep track of the stress history of the lithosphere, potentially accounting for a "memory" of past deformation events [e.g., *Bercovici and Ricard*, 2014].

#### Appendix 4.1. Fault-induced topography in a viscous lithosphere

The plate deflection resulting from slip on a fault is modeled by adding the contribution of (a) rigid motion of the hanging wall and footwall blocks along the fault and (b) flexure of the footwall and hanging wall blocks in response to gravity [Weissel and Karner, 1989]. If  $w^*(x,t)$  denotes the topography resulting from step (a) alone, the deflection  $w(x,t)$  corresponding to step (b) can be calculated as the flexural response to the load exerted by  $w^*(x,t)$ . In a viscous faulted layer,  $w(x,t)$  is a solution to the thin viscous plate equation [Biot, 1961; Turcotte and Schubert, 2002]

$$F \frac{\partial^4 w}{\partial x^4} + \Delta \rho g w = -\Delta \rho g w^* \quad (4.S1)$$

where  $F$  denotes the viscous equivalent to the elastic flexural rigidity  $D$  (Equation 4.13)

$$F = \frac{1}{6} \eta_L H^3 \quad (4.S2)$$

and  $w^*(x,t)$  is

$$w^*(x,t) = \begin{cases} -\frac{Ut}{2} \tan \theta, & \forall x \leq -\frac{Ut}{2} \\ x \tan \theta, & \forall x \in \left[ -\frac{Ut}{2}, +\frac{Ut}{2} \right] \\ +\frac{Ut}{2} \tan \theta, & \forall x \geq +\frac{Ut}{2} \end{cases} \quad (4.S3)$$

The resulting, fault-induced topography  $w^T(x,t)$  is then obtained by adding increments of  $w^*(x,t)$  and  $w(x,t)$ , following

$$\frac{\partial w^T}{\partial t} = \frac{\partial w}{\partial t} + \frac{\partial w^*}{\partial t} \quad (4.S4)$$

In the following, we outline a semi-analytical method to solve (4.S1)–(4.S4) using Laplace and Fourier transforms. The problem is reduced to the calculation of an inverse Fourier transform, which can be estimated numerically. We then propose an approximate solution that captures the behavior of the exact solution and is easier to implement in simple scaling models.

For any function  $f(x,t)$  we write  $\hat{f}(k,t)$  its Fourier transform defined as

$$\hat{f}(k,t) = \frac{1}{\sqrt{2\pi}} \int_{-\infty}^{+\infty} f(x,t) e^{ikx} dx \quad (4.S5)$$

In addition, the inverse Fourier transform is defined by

$$f(x,t) = \frac{1}{\sqrt{2\pi}} \int_{-\infty}^{+\infty} \hat{f}(k,t) e^{-ikx} dk \quad (4.S6)$$

The Laplace transform  $\tilde{f}(x,s)$  is defined as

$$\tilde{f}(x,s) = \int_0^{+\infty} f(x,t) e^{-st} dt \quad (4.S7)$$

Taking the Laplace and Fourier transforms, successively, of Equation (4.S1) yields

$$\hat{\tilde{w}} = \frac{-\Delta\rho g}{k^4 F s + \Delta\rho g} \hat{\tilde{w}}^* \quad (4.S8)$$

In order to calculate the Laplace transform of  $w^*(x,t)$  (Equation 4.S3), we rewrite it as an explicit function of time:

$$w^*(x,t) = \begin{cases} \operatorname{sgn}(x) \frac{Ut}{2} \tan\theta, & \forall t \leq \left| \frac{2x}{U} \right| \\ x \tan\theta, & \forall t \geq \left| \frac{2x}{U} \right| \end{cases} \quad (4.S9)$$

Piece-wise integration yields

$$\tilde{w}^*(x,s) = \frac{U}{2s^2} \tan\theta \left( 1 - e^{-\left| \frac{2xs}{U} \right|} \right) \times \operatorname{sgn}\left( \frac{2xs}{U} \right) \quad (4.S10)$$

Finally, the Fourier transform of Equation (4.S10) is found to be

$$\hat{\tilde{w}}^*(k,s) = \frac{Ui \tan\theta}{k\sqrt{2\pi}} \times \frac{1}{\left( s + i \frac{Uk}{2} \right) \left( s - i \frac{Uk}{2} \right)} \quad (4.S11)$$

Using Equation (4.S8), we can now write  $\hat{\tilde{w}}(k,s)$

$$\hat{\tilde{w}}(k,s) = -\frac{iU\Delta\rho g \tan\theta}{k^5 F \sqrt{2\pi}} \times \frac{1}{\left( s + \frac{\Delta\rho g}{k^4 F} \right) \left( s + i \frac{Uk}{2} \right) \left( s - i \frac{Uk}{2} \right)} \quad (4.S12)$$

We note that the  $s$ -dependence of Equation (4.S12) is a rational fraction that we can expand into a sum of partial fractions. We can then identify a sum of tabulated Laplace

transforms, which are readily inverted into time domain. By applying the inverse Fourier transform formula (Equation 4.S6), we can reduce the calculation of  $w(x,t)$  to the estimation of an integral, which can be performed numerically.

$$w(x,t) = -\frac{iU\Delta\rho g \tan\theta}{2\pi F} \times \int_{-\infty}^{\infty} \frac{1}{k^5} \left( \frac{1}{iUk \left( A(k) + \frac{iUk}{2} \right)} e^{\frac{iUk}{2}} - \frac{1}{iUk \left( A(k) - \frac{iUk}{2} \right)} e^{-\frac{iUk}{2}} + B(k) \right) e^{-ikx} dk \quad (4.S13)$$

with

$$A(k) = \frac{\Delta\rho g}{k^4 F} \quad (4.S14)$$

and

$$B(k) = \frac{1}{\left( A(k) + \frac{iUk}{2} \right) \left( A(k) - \frac{iUk}{2} \right)} e^{-A(k)t} \quad (4.S15)$$

We note that the use of the Laplace transform makes this derivation very similar to the case of an elastic thin plate, which would be characterized by the following flexure equation:

$$D \frac{\partial^4 w}{\partial x^4} + \Delta\rho g w = -\Delta\rho g w^* \quad (4.S16)$$

which can be expressed in Fourier domain:

$$\hat{w} = \frac{-\Delta\rho g}{k^4 D + \Delta\rho g} \hat{w}^* \quad (4.S17)$$

Equation (4.S17) has the same form as Equation (4.S8) provided  $D$  is replaced by  $F_s$ . This suggests that the elastic solution with a time-dependent flexural rigidity is a good approximation for the viscous problem. From dimensional analysis, we propose an equivalent viscous rigidity of the form

$$D_v(t) = \frac{F}{t} = \frac{\eta_L H^3}{6t} \quad (4.S18)$$

By analogy, we define a time-dependent viscous bending wavelength as

$$\alpha_v = \left( \frac{\zeta F}{\Delta\rho g t} \right)^{\frac{1}{4}} \quad (4.S19)$$

where  $\zeta$  is a scaling factor. We next recall the elastic solution to Equation (4.S17) outlined in Chapter 2:

$$w^T(x) = \frac{1}{4} \alpha_E \tan \theta \left( f \left| \frac{x-h/2}{\alpha_E} \right| - \left( f \left| \frac{x+h/2}{\alpha_E} \right| \right) \right) \quad (4.S20)$$

with  $f$  defined as

$$f(x) = e^{-x} (\sin x - \cos x) \quad (4.S21)$$

We compare our exact solution (4.S13) to the elastic solution using the time-dependent wavelength  $\alpha_V$  defined in Equation (4.S19) instead of the elastic wavelength  $\alpha_E$ . We find that equation (4.S20) provides the best approximation for the exact solution when  $\alpha_V$  is calculated with a scaling factor  $\zeta \approx 6$  (Figure 4-S1). We therefore propose the following definition for the viscous bending wavelength, which is used throughout the main text:

$$\alpha_V = \left( \frac{\eta_L H^3}{\Delta \rho g t} \right)^{\frac{1}{4}} \quad (4.S22)$$

Finally, because fault heave ( $h$ ) is more useful than time to describe experiments carried out at different extension rates, we rewrite (4.S22) as

$$\alpha_V = \left( \frac{\eta_L U H^3}{\Delta \rho g h} \right)^{\frac{1}{4}} \quad (4.S23)$$

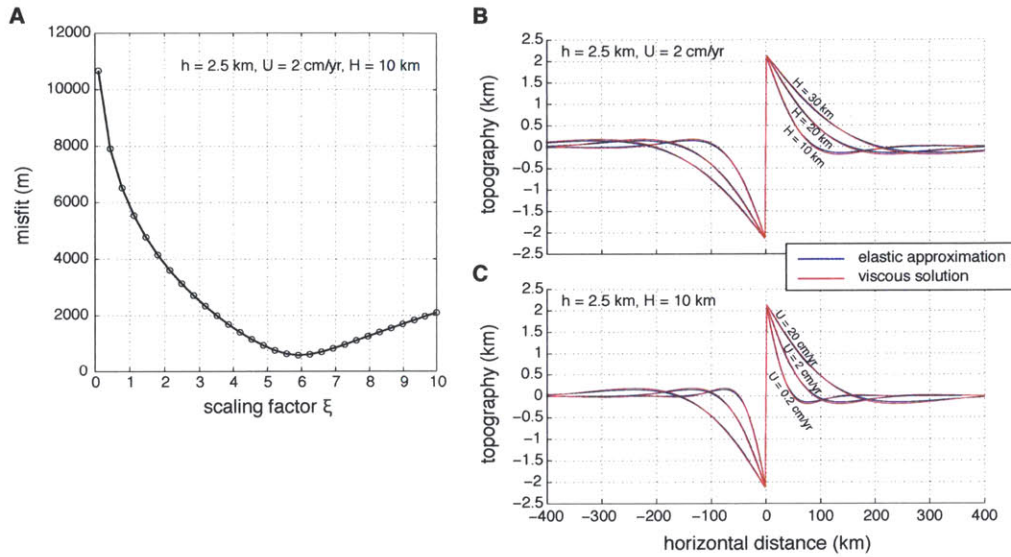


**Figure 4-S1.** (A) Illustrative RMS misfit between the exact solution to the viscous faulting problem (calculated from Equation 4.S13 through numerical integration) and the approximate solution (Equation 4.S20 using the viscous flexural wavelength  $\alpha_V$  from Equation 4.S19 instead of  $\alpha_E$ ) using various scaling factors  $\xi$ . This example corresponds to a fault heave of 2.5 km in a 10 k-thick layer with a viscosity of  $10^{24}$  Pa·s extended at a full rate of 2 cm/yr. (B) and (C) Topographies predicted by the exact solution (red) and the approximate solution using  $\xi = 6$  (blue) for a range of layer thicknesses  $H$  and extension rates  $U$ .





## **Chapter 5:**

# **Oceanic core complex structure controlled by the depth distribution of magma emplacement<sup>3</sup>**

### **Abstract**

Recent modeling studies suggest that long-lived ( $\geq 1-2$  Myr) detachment faults form oceanic core complexes (OCCs) at mid-ocean ridges when magma is supplied to the spreading axis within a restricted 'window' of intrusion rates equal to about 30–50% of the total plate separation. This is paradoxical when considered in the context of field observations, which show that detachments exhume rock types ranging from extensive tracts of mantle peridotite (i.e., entirely amagmatic conditions) to exclusively intrusive gabbroic bodies (i.e., fully magmatic conditions). Here we show that the magmatic window required to drive detachment fault growth can be reconciled with this extreme range of magmatism by allowing different rates of magma intrusion above and below the brittle-ductile transition. We find that while the rate of magma intrusion in the brittle layer controls fault evolution, the rate of intrusion below the brittle-ductile transition has no influence on fault development. Further, although magma accretion in the brittle layer is focused to the opposite side of the ridge axis from the detachment, magma emplacement in the ductile layer is symmetric about the ridge axis, and the emplacement rate below the brittle-ductile transition controls the volume of gabbro exhumed in OCCs.

---

<sup>3</sup> Published as: Olive, J.-A., Behn, M. D., and B. E. Tucholke (2010), The structure of oceanic core complexes controlled by the depth-distribution of magma emplacement, *Nature Geoscience*, 3, 491-495.

## 5.1. Introduction

Mid-ocean ridges (MORs) are divergent plate boundaries representing the surface expression of large-scale upwellings in the convecting mantle of the Earth, where adiabatic decompression triggers partial melting over wide areas. As buoyant melt ascends within the asthenosphere, it is collected and focused toward the ridge axis, where it is eventually emplaced as new oceanic crust. Magmatic heat drives vigorous hydrothermal circulation that cools the ridge axis forming a rigid layer of oceanic lithosphere, where normal faults develop in response to tensional stresses.

It has long been acknowledged that fault styles and ridge morphology are highly dependent of spreading rate [Small, 1998]. At fast-spreading ridges such as the East Pacific Rise, where magmatic input is elevated, most of the extension in the shallow lithosphere is accommodated by intrusion of basaltic dikes, and faulting is limited [MacDonald and Fox, 1988]. At slow-spreading ridges such as the Mid-Atlantic Ridge (MAR), the colder thermal regime results in spatially and temporally variable, but overall limited magmatic input [Lin *et al.*, 1990; Tucholke *et al.*, 1997]. In those settings, faulting generally contributes to a higher percentage of extension.

Along the MAR, first-order segment centers are often characterized by an axial valley bounded by symmetric, high-angle normal faults [Tapponnier and Francheteau, 1978]. This mode of spreading has long been envisioned as dominant at slow-spreading ridges. Recent evidence, however, points to the existence of a fundamentally distinct mode of spreading involving long-lived, low-angle normal faults termed "detachments" that accommodate most of the extension asymmetrically, on one side of the ridge axis [Escartin *et al.*, 2008].

The observation of large tracts of serpentinized mantle and various lower-crustal units directly exposed at the seafloor first led Dick *et al.* [1981] to infer the existence of low-angle normal faults exhuming deep lithologies in the vicinity of ridge-transform intersections. Since then, many authors have reported the exposure of such lithologies within dome-shaped, corrugated massifs termed oceanic core complexes (OCCs), which were interpreted as the exposed footwalls of fully developed detachment faults (Figure 5-1) [Cann *et al.*, 1997; Tucholke *et al.*, 1998]. While OCCs were first thought to form in purely amagmatic conditions [Tucholke and Lin, 1994], geologic studies involving direct

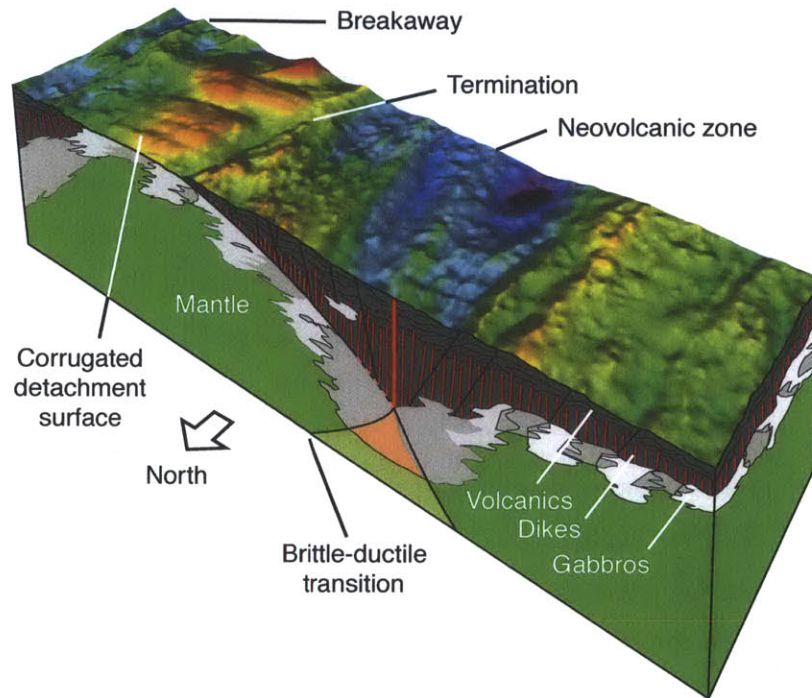


**Figure 5-1.** Morphology of the Mid-Atlantic Ridge axis at 26.6°N, looking to the southeast. Dante's Domes OCC is at left, showing domed structure, flowline-parallel surface corrugations, and other structural features characteristic of OCCs formed by long-lived detachment faults. The box is 60 km across-axis, 17 km along-axis and about 8 km deep. Distribution of crustal lithologies and mantle is shown schematically in cross section. The distribution assumes that the detachment initiated in response to a reduction in melt supply to the brittle lithosphere ( $M_B$  reduced to  $\sim 0.5-0.3$ ) and that melt input was variable within this range during fault growth. The detachment appears to no longer be active, and may have been terminated because of an increase in melt supply as indicated by thickened crust at the ridge axis. Figure courtesy of B. Tucholke, bathymetry data from *Wang et al.* [submitted].

observation, sampling at the fault surface and drilling in the footwall later established that plutonic rocks were being emplaced as the detachment was actively growing [Dick *et al.*, 2000; MacLeod *et al.*, 2002; Ildefonse *et al.*, 2007; Dick *et al.*, 2008]. Furthermore, Tucholke *et al.* [1998] reported that OCCs were most commonly found within a narrow range of spreading rates and were virtually absent from magma-starved ultraslow spreading centers. They therefore proposed that magmatic processes play an essential role in sustaining the growth of a detachment fault over long periods of time.

Numerical models have recently established that the amount of melt supplied to a MOR spreading segment is a key control on the development of normal faults [Buck *et al.*, 2005; Behn and Ito, 2008; Tucholke *et al.*, 2008]. Maintaining slip on a normal fault involves continuously bending the lithosphere and sustaining the build-up of topography, both of which require a greater tensional force when the lithosphere is thicker [Forsyth, 1992; Buck, 1993; Lavier *et al.*, 2000]. The amount of extension accommodated by diking at the ridge axis (expressed as a fraction  $M$  of the total spreading rate) controls the rate at which an active fault migrates off-axis and encounters thicker and thicker lithosphere. For example, elevated rates of diking at the ridge axis (e.g.,  $M > 0.6$ ) lead to rapid fault migration toward thick off-axis lithosphere, where sustaining slip quickly becomes less favorable than breaking a new fault at the axis. This simple kinematic effect leads to an inverse correlation between fault life span and the magmatic fraction  $M$ .

As  $M$  decreases toward a critical value of 0.5, faults can accumulate more and more offset. They then have to undergo flexural rotation to maintain isostatic equilibrium, resulting in the formation of a dome-shaped footwall [Lavier *et al.*, 1999]. Models that incorporate the magmatic component of spreading predict the occurrence of OCCs within a limited range of magmatic budgets ( $M \sim 0.3-0.5$ ) [Tucholke *et al.*, 2008]. However, a major shortcoming of these models is that they only account for diking in the shallow lithosphere and can therefore not explain the high variability in the volume of plutonic rocks exposed in OCCs.

At the apparently magmatic end of the spectrum, Atlantis Bank on the Southwest Indian Ridge exposes a continuous gabbro section that extends  $\geq 10$  km along plate flow lines and is  $\geq 1.5$  km thick [Dick *et al.*, 2000]. By contrast, extensive exposures of mantle peridotite with a few imbedded gabbro plutons occur in OCCs on the Mid-

Atlantic Ridge (Figure 5-1), suggesting reduced and/or more intermittent magma supply [Blackman *et al.*, 2002; MacLeod *et al.*, 2002; Dick *et al.*, 2008; Xu *et al.*, 2009]. Further, although hanging-walls of OCCs have been poorly studied, they seem to show little structural/morphologic variation, which suggests that they may have relatively uniform composition compared to variations in the OCC footwalls. These features suggest not only that melt supply to detachment footwalls is strongly four-dimensional, but also that melt may be partitioned differently above and below the brittle-ductile transition (BDT).

The aim of this study is to incorporate magmatic injection below the brittle lithosphere in a numerical model of mid-ocean ridge faulting, in order to assess whether the wide range of magmatic inputs documented by OCCs can be reconciled with the idea that detachment faults form within a narrow window of melt supply to the brittle lithosphere.

## **5.2. Numerical simulations of melt emplacement near a growing fault**

We use the Fast Lagrangian Analysis of Continua (FLAC), an explicit inertial technique, to solve for conservation of mass, momentum, and heat [Cundall, 1989; Poliakov and Buck, 1998; Lavier and Buck, 2002] in a 60 km wide by 20 km deep domain representing a vertical cross-section of a mid-ocean ridge that is spreading symmetrically at a half-rate  $U_S = 2.5$  cm/yr (Figure 5-2). Top and bottom boundaries are stress-free and hydrostatic, respectively.

Material deforms following a dry diabase rheology [Mackwell *et al.*, 1998], which is effectively elastic-plastic above the 600°C isotherm (equivalent to the BDT) and visco-elastic below. Plastic yielding occurs in the brittle layer wherever a Mohr-Coulomb criterion is met. Cohesion is rapidly reduced in the corresponding elements as plastic strain accumulates, which allows the development of localized shear bands (faults).

The FLAC method employs a lagrangian description of the deformation field. This results in the distortion of model elements as they accumulate strain due to faulting or magma injection, and causes a loss of numerical accuracy. To circumvent this problem, we regrid the model domain whenever the distortion of an element reaches a critical threshold. All variables of interest are then linearly interpolated from the old (deformed) grid to the new (undeformed) grid. This process is illustrated in Figure 5-3.

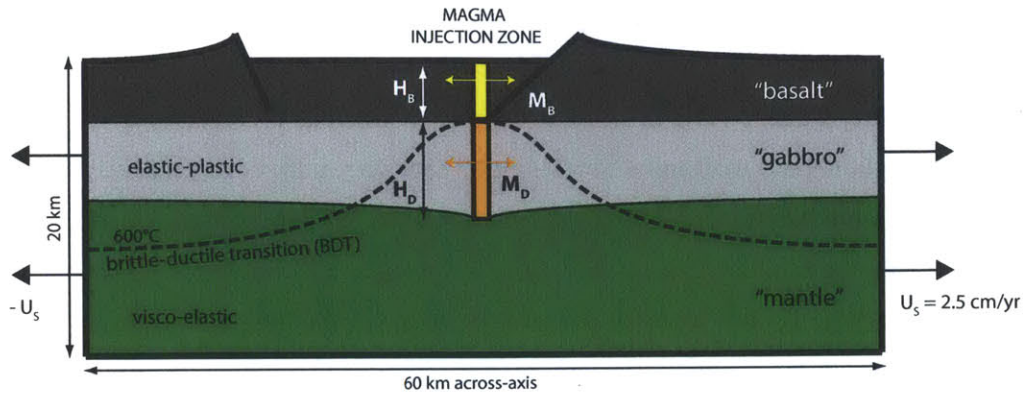


**Figure 5-2.** Synthetic model geometry. Symmetric stretching is applied on the sides of the domain. The brittle-ductile transition (600°C isotherm) separates a visco-elastic (ductile) asthenosphere from an elastic-plastic (brittle) lithosphere where faults can initiate spontaneously. New materials are continuously being added to the model space from a central, fixed injection zone. The brittle portion of the injection zone (yellow) replaces brittle-injected crust (BIC) at a rate  $M_B$  over a height  $H_B$ , while its ductile portion (orange) replaces ductile-injected crust (DIC) at a rate  $M_D$  over a height  $H_D$ . Both crustal lithologies (and the upwelling mantle) are tracked as they are advected off-axis.

Magma injection is modeled by applying an elastic stress perturbation on a fixed central column of elements over one numerical time step [Behn and Ito, 2008]. Heat is simultaneously added to the ridge axis, accounting for both the injection temperature of the magma (1200°C) and the latent heat of crystallization. No heat diffusion is allowed through the sides. Temperature along the bottom boundary is taken from a half-space cooling model at the corresponding depth, with a maximum temperature of 1300°C. The top of the model space is set to 0°C. Thermal diffusivity is enhanced by a Nusselt number ( $Nu$ , typically 2-10) within the first 8 km below seafloor, in order to model efficient heat extraction by hydrothermal circulation, and to provide some control on the thermal structure (higher  $Nu$  produces thicker lithosphere).

The effective "magmatic spreading" can be regarded as the relaxation of the quantum elastic perturbation, which results in net horizontal widening of the column, pushing on the surrounding material at a rate proportional to the spreading half-rate. Above the BDT, "brittle-injected crust" (BIC) is added at a rate  $U_B = 2 M_B U_s$ , while

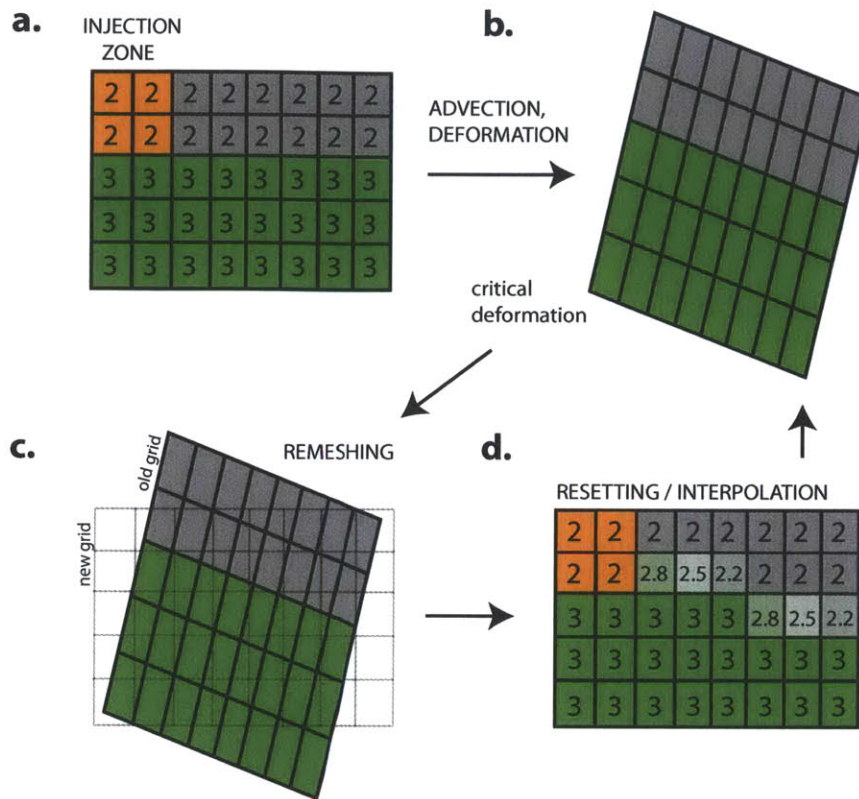


**Figure 5-3.** Numerical procedure for continuously injecting new materials and tracking them throughout a model run. Each element is assigned an identity number (1 = BIC, 2 = DIC, 3 = mantle). As materials are advected off-axis, they tend to distort (a-b) until a critical threshold is met (when the smallest angle of a quadrilateral element becomes  $\leq 5^\circ$ ). All variables of interest - including the identity number - are then linearly interpolated (c-d) from the old (deformed) grid to a new orthogonal grid. During each regridding, the identity numbers are automatically reset to 1 and 2 within the brittle- and ductile- portions of the injection zone, respectively. Regriddings are frequent enough that this results in continuous BIC and DIC injection.

"ductile-injected crust" (DIC) is added below at a rate  $U_D = 2 M_D U_S$ . The total height of the injection zone ( $H = H_B + H_D$ ) is defined for each model run, but the relative heights of the brittle ( $H_B$ ) and ductile ( $H_D$ ) injection evolve with the thermal structure. Magma injection is therefore fully described by a set of four independent parameters, namely the vertical height and rate of brittle ( $H_B$  and  $M_B$ ) and ductile ( $H_D$  and  $M_D$ ) injection (see Figure 5-2 and Fig. 5-4 a-b). We consider that the BIC is representative of upper-crustal

volcanics and sheeted dikes, while the DIC represents gabbroic plutons intruded beneath the BDT. This simplified formulation takes into account the mechanical and thermal effects of gabbro intrusion, and as such may represent a wide range of potential lower-crust emplacement mechanisms.

To effectively track lithologies throughout a model run and investigate the crustal emplacement patterns, we assign an identity number (Figure 5-3) to new materials at each location where they enter the model space: (1) BIC, (2) DIC and (3) new mantle, which upwells through the base of the domain.

### 5.3. Results

A series of simulations was performed with different combinations of injection parameters ( $H_B$ ,  $M_B$ ,  $H_D$  and  $M_D$ ). Consistent with previous studies, we find that OCCs develop by detachment faulting in simulations where  $M_B \sim 0.3-0.5$ . At  $M_B = 0.5$ , OCC formation results in a systematic pattern of crustal emplacement in which BIC is accreted solely on the conjugate side, leaving a remnant BIC hanging-wall block adjacent to the seafloor trace of the detachment fault that forms the OCC (Figure 5-4). DIC, however, is distributed equally between the OCC side, where it is exhumed in the footwall of the detachment, and the conjugate side, where it is emplaced below the BIC. Numerical smearing associated with regriding produces the artifact of a thin ( $\sim 2$  element size) carapace of BIC on the footwall of long-lived faults (visible in Figure 5-4). Imposing a sudden change in  $M_B$  to a value  $\neq 0.5$ , whether higher or smaller results instantaneously disrupts the growth of the detachment fault.

Detachment fault growth is not affected by the imposed value of  $M_D$ , (Figure 5-4 a-b) or by changes in  $M_D$  through time (Figure 5-4c). However, changes in  $M_D$  directly control the amount of DIC that is exhumed in the OCC and emplaced in the ductile layer on the conjugate side. Similarly, changing only  $H_D$  (not shown) affects the thickness of the DIC layer in the OCC as well as the ratio of BIC versus DIC emplaced on the conjugate side, but it does not change the overall pattern of faulting.

We quantified our results over a range of injection parameters (e.g.,  $H_B$ ,  $M_D$ , and  $H_D$ ) by comparing the total crustal thickness (BIC + DIC) 10 km off-axis on the detachment ( $t_d$ ) and conjugate ( $t_c$ ) sides of the ridge axis for a series of model runs with

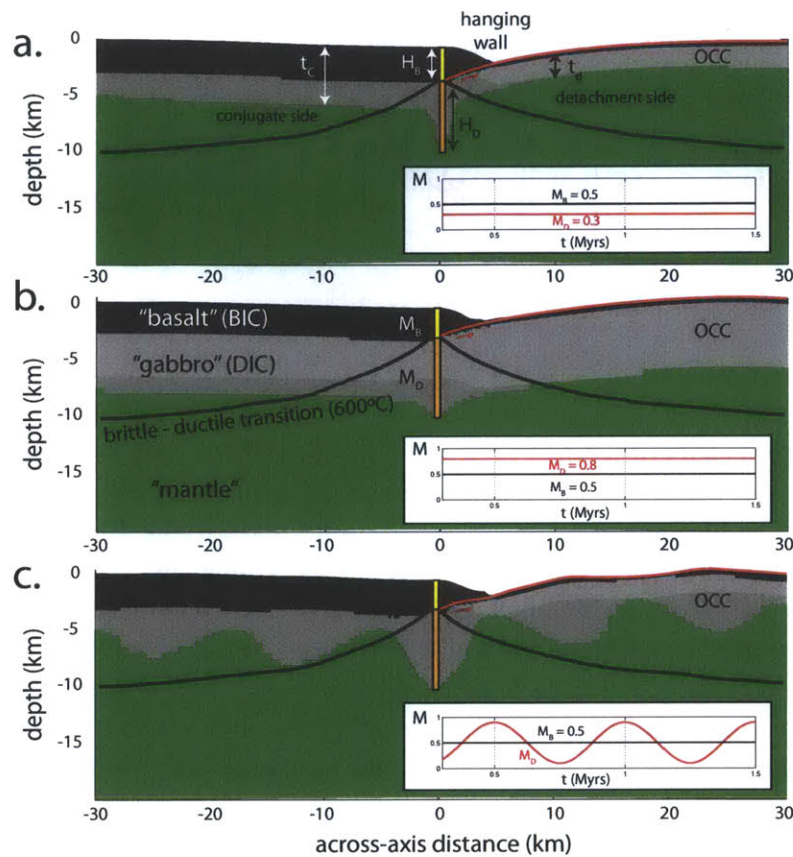


**Figure 5-4.** Modeled faulting and partitioning of volcanic, plutonic, and mantle materials during OCC growth. Distribution of brittle-injected crust (BIC, black), ductile-injected crust (DIC, gray), and mantle (green) lithologies after 1.5 Myrs of spreading in cases where  $M_B = 0.5$  and a detachment fault develops continuously.  $M_D$  varies from (a) 0.3 to (b) 0.8, and in (c) it oscillates between 0.1 and 0.9 with a period of 0.5 Myrs. In these runs,  $H_B + H_D = 10$  km, with  $H_B \sim 3$  km. The BDT separating BIC and DIC (yellow and orange parts of the central dike, respectively) corresponds to the 600°C isotherm (thick black line).

$M_B$  held fixed at 0.5 (Figure 5-4a). A simple mass balance calculation is used to predict crustal thickness variations across an OCC as a function of  $H_B$ ,  $M_D$ , and  $H_D$ . Assuming symmetric spreading about the ridge axis, the total thickness of BIC and DIC emplaced within the injection zone will be  $2 M_B H_B$  and  $2 M_D H_D$ , respectively. However, because the hanging wall of the detachment does not grow, the BIC must accrete solely on the

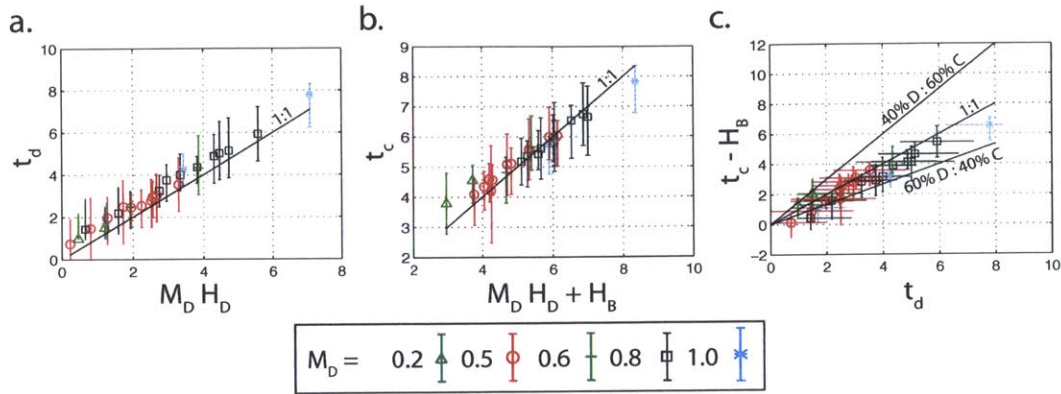


**Figure 5-5.** Predicted crustal thicknesses as a function of the injection parameters. Total crustal thickness (BIC + DIC) on the detachment ( $t_d$ ) and conjugate ( $t_c$ ) sides of the ridge axis from a suite of model runs with fixed  $M_B = 0.5$  and varying  $M_D$  (0.2-1.0),  $H_B$  (1-3 km) and  $H_D$  (1-7 km). Panels (a) and (b) illustrate the scaling laws (1:1 line) predicting  $t_d$  and  $t_c$ , while (c) compares DIC thickness in the footwall of the detachment (D) vs. the conjugate side (C). The 1:1 line corresponds to symmetric DIC emplacement while the other two lines show 40% and 60% asymmetry on either side, respectively. Error bars measure uncertainties associated with numerical smoothing when assigning material identities to the elements, and are typically 1 or  $2 \times$  element-size.

conjugate side, while the DIC is equally partitioned across the ridge axis. Thus, for  $M_B = 0.5$  the crustal thickness expected on the detachment side is

$$t_d = M_D H_D \quad (5.1)$$

while on the conjugate side

$$t_c = H_B + M_D H_D \quad (5.2)$$

These simple mass balance relations do an excellent job of predicting the numerical results over a wide range of  $H_B$ ,  $M_D$ , and  $H_D$ . (Figure 5-5).

We also investigated several cases where  $M_B \neq 0.5$  (Figure 5-6). For simplicity, we fixed  $M_B = M_D = M$  in these simulations, but we note that emplacement may be more complex when  $M_B \neq M_D$ . For  $M_B = 0.4$ , a long-lived detachment forms, but the detachment surface is dissected by steep, mostly outward-dipping normal faults that offset both the BIC and DIC layers (Figure 5-6b). Total crustal thickness on each plate remains fairly constant through time, but a portion of BIC that normally would accrete on

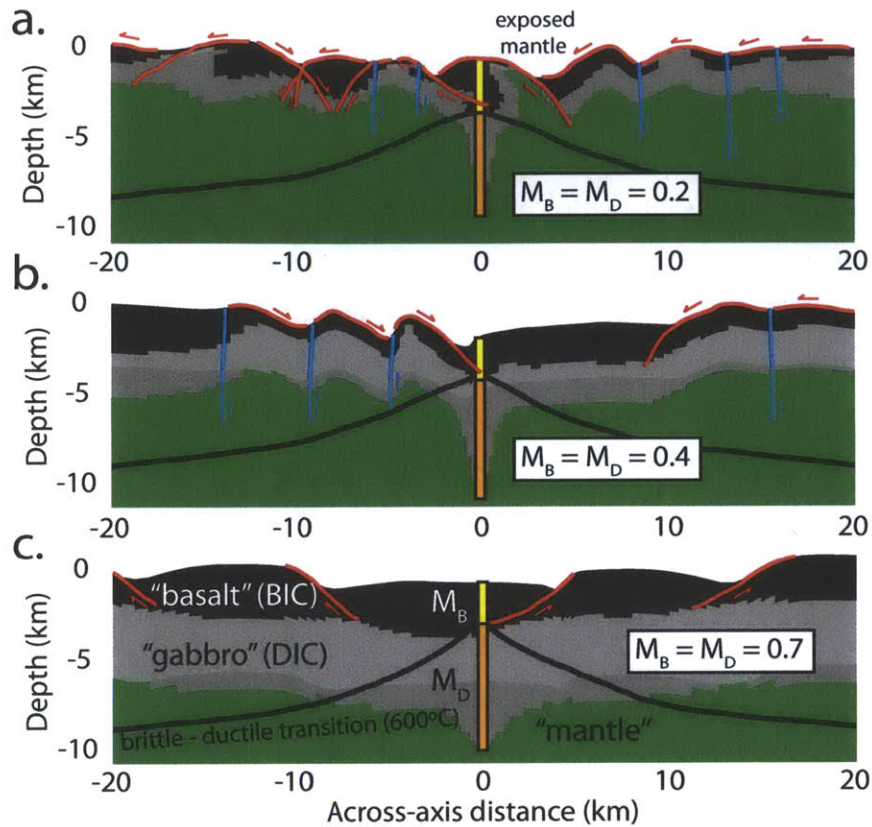


**Figure 5-6.** Modeled faulting and partitioning of volcanic, plutonic and mantle materials as a function of melt supply. Model snapshots are at 1.5 Myrs for cases where  $M_B = M_D$  = (a) 0.2, (b) 0.4, and (c) 0.7. In these runs,  $H_B + H_D = 9$  km, with  $H_B \sim 2-3$  km. First- and second-generation fault surfaces are shown in red and blue, respectively. Other conventions are indicated in the caption of Figure 5-4.

the conjugate is transferred to the OCC. This is apparently caused by the detachment migrating toward the axis and crossing the injection zone where it takes up, by tectonic extension, the accretion deficit on the conjugate side. As  $M_B$  decreases further to 0.2 (Figure 5-6a), random on-, off-, and cross-axis faulting becomes the normal style of extension, both DIC and BIC are transferred irregularly between plates, and mantle can be exhumed. This results in a very complex structure and distribution of lithologies. By contrast, when  $M_B$  is  $> 0.5$ , a continuous crustal layer is produced on both plates. In this

case, the thickness of the DIC layer is essentially constant but the BIC is thinned by faults that alternate back and forth across the ridge axis (Figure 5-6c).

#### 5.4. Discussion

The key finding in this study is that differing rates of magma intrusion in the brittle and ductile regimes control both the patterns of faulting and the distribution of igneous lithologies at mid-ocean ridges in a systematic manner. Specifically, we show that the entire range of synkinematic DIC intrusion rates ( $M_D = 0-1$ ) is compatible with detachment fault growth, provided that BIC intrusion rates are in the critical range ( $M_{B\text{ CRIT}}$ ) of 0.5 to  $\sim 0.3$ . Introducing a depth-variable rate of magma intrusion reconciles the intermediate rate of diking needed to allow detachment faulting in the lithosphere with either amagmatic exhumation of large tracts of mantle ( $M_D \sim 0$ ) or synkinematic emplacement of gabbroic bodies at virtually any scale ( $M_D = f(t) > 0$ ) in the footwalls of OCCs. A corollary to this result is that emplacement of a large gabbro body will trigger OCC termination only if it results in increased rates of diking ( $M_B > 0.5$ ) in the brittle lithosphere. It also suggests that (1) an OCC may terminate solely by vertical redistribution of a constant melt supply, e.g. if a larger portion of the total melt input is erupted in the brittle lithosphere, and (2) that a sudden increase in magma supply may be initially accommodated by the ductile asthenosphere, which would delay the disruption of the detachment fault, as suggested by *MacLeod et al.* [2009].

We propose two end-member scenarios that could lead to variations in magma injection with depth (Figure 5-7). In the first, shown Figure 5-7a, dike intrusion in the brittle lithosphere occurs by along-axis propagation from a magma-rich segment center toward the segment end [*Fialko and Rubin, 1998*]. In this scenario,  $M_B$  declines into the detachment-forming range,  $M_{B\text{ CRIT}}$ , toward segment ends, where most OCCs are found [*Tucholke et al., 1998*]. Dikes above the detachment are not fed from below because the colder thermal regime inferred in these areas favors melt crystallization at depth rather than eruption [*Cannat, 1996*]. As a consequence, primarily mantle is exhumed by a detachment fault that is located at the dike/mantle transition. This kind of structural / lithological relationship has been interpreted at the Kane OCC on the MAR [*Dick et al., 2008*].

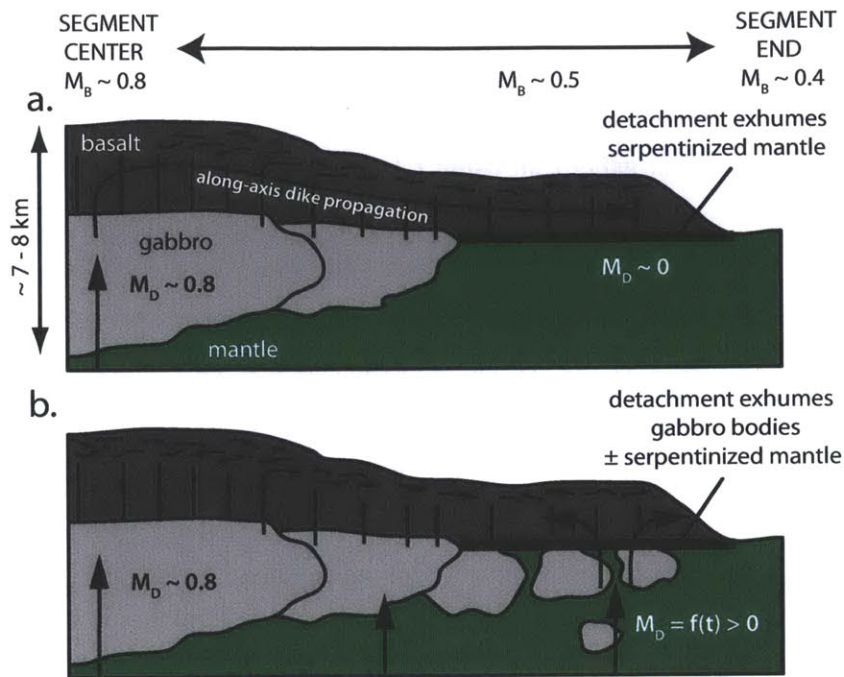


**Figure 5-7.** End-member models for detachment faulting and melt distribution at the segment scale. In these along-axis scenarios, a long-lived detachment fault (bold line) forms at the along-axis position where melt supply to the brittle layer is in the critical range ( $M_{B\ CRIT} = 0.5$  to  $\sim 0.3$ ) needed for detachment faulting. In (a), melt is supplied entirely by along-axis dike propagation from the segment center, little or no melt is derived from below the detachment, and mantle is exhumed along a dike/mantle contact. In (b),  $M_{B\ CRIT}$  is achieved by melt derived from intrusions below the detachment, and gabbro plutons are exhumed in the OCC along a dike-gabbro contact.

In the second scenario, dikes are fed from underlying gabbro intrusions (Figure 5-7b).  $M_{B\ CRIT}$  could be satisfied anywhere within the segment, but is more likely to be achieved away from the more magmatically robust segment center, and thus toward the segment end. Of course  $M_{B\ CRIT}$  could also be achieved by some combination of lateral and vertical diking represented by these two end members. It is noteworthy that this spectrum of scenarios accommodates a wide variety of temperature and intrusion conditions in the detachment footwall, which may explain why very different kinds of temperature/deformation histories have been documented in different OCCs [Dick *et al.*, 2008; Escartin *et al.*, 2003].

Although our simulations involve continuous crustal layers, OCCs tend to exhume discrete gabbro bodies surrounded by serpentinized peridotite [Blackman *et al.*, 2002; Dick *et al.*, 2008]. This likely reflects both spatial (along-axis) and temporal (across-axis) variations in gabbro intrusion rates. Along-axis variations in gabbro layer thickness can be accounted for in our simulations by variations in either  $M_D$  (reflecting differences in melt supply) or  $H_D$  (reflecting variations in axial thermal structure, which will in turn be influenced by magma supply and/or the efficiency of hydrothermal cooling). Our model also predicts that gabbro exhumed in an OCC should be matched by an equal volume of gabbro in the conjugate plate, below volcanics and sheeted dikes of the upper crust, provided that far-field extension is symmetric about the ridge axis, which may not be the case for all OCCs. This prediction can be tested by detailed seismic and gravity studies across both an OCC and its conjugate hanging wall [e.g., Planert *et al.*, 2010], which are still rare at the moment.

Temporal variability in melt supply in slow-spreading crust is well established. Cycling between relatively magmatic and amagmatic conditions often appears to occur on the Mid-Atlantic Ridge at periods of ~ 2-4 Myr [Bonatti *et al.*, 2003; Tucholke *et al.*, 1997] possibly reflecting heterogeneities in mantle fertility. Interestingly, most fully-matured OCCs have developed over about 1-2 Myr [Tucholke *et al.*, 1998], which may suggest that  $M_{B\text{ CRIT}}$  is achieved over about half the duration of long-period magmatic cycles. Shorter-period magmatic cyclicity also occurs on time scales down to 80-160 kyrs [Canales *et al.*, 2000] and may be associated with the dynamics of magma ascent, storage, and eruption. These fluctuations are likely responsible for the development of discrete gabbro bodies within OCCs, as illustrated by the model in Figure 5-4c. Our model predicts that a detachment formed under these fluctuating conditions will display small oscillations in OCC footwall topography, as seen in panel c of Figure 5-4, because of the density contrast between the gabbro plutons and the surrounding mantle. Modeled oscillations are on the order of 150 m for 4-km variations in gabbro layer thickness, when one would expect ~500 m from full isostatic compensation. This argues for a strong flexural component in the compensation. Even though there seems to be no correlation between topography and lithology at the Kane OCC [Dick *et al.*, 2008], it is plausible that

the flexural stresses associated with gabbro emplacement may contribute to high-angle off-axis faulting of the footwall, which is often observed [Tucholke *et al.*, 1998].

If OCCs are indeed representative of a unique "asymmetric" mode of seafloor spreading [Escartin *et al.*, 2008], then our modeling may shed new light on the segment-scale interrelations between tectonic, magmatic, and hydrothermal processes that favor one mode of faulting over another. Symmetric spreading is well accounted for by robust magmatic injection in the lithosphere, keeping normal faults short-lived and closely spaced (Figure 5-6c). In our framework, asymmetric spreading does not require a significantly different magmatic input, but rather a different vertical distribution of melt emplacement, with more magma being trapped at depth and less injected within the lithosphere. This could result from an overall colder thermal regime that inhibits crystal-liquid separation within plutonic bodies and limits their eruptibility [MacLeod *et al.*, 2009].

Our model predicts a symmetric pattern of emplacement for all lithologies intruded below the BDT in asymmetric settings. However, an increasing body of evidence points to systematically faster extension on the OCC side than on the conjugate side [Baines *et al.*, 2008; Dick *et al.*, 2008; MacLeod *et al.*, 2009], which should be a major focus of future modeling studies. Symmetric emplacement of the lower-crust in our model is a direct consequence of two assumptions that will have to be relaxed in future studies. First, the symmetric stretching applied on the sides of our model generates a symmetric corner flow extending into the OCC footwall (the detachment fault acts as a kinematic upper-boundary condition) and below the conjugate upper-crust. We expect that asymmetric spreading should result in a systematic migration of the ridge axis toward the OCC side relative to the underlying mantle. This would add a lateral component to the corner flow away from the OCC, and would then advect more plutonic rocks to the conjugate side, a prediction again testable by seismic and gravity studies. The second assumption lies within the choice of our rheological parameters, and specifically of our fault-weakening law. This law only allows localization of deformation within the lithosphere, but the recovery of mylonites and ultramylonites from OCC footwalls argues for localization of deformation within the ductile regime. If that is the case, then detachments may root deeper than the BDT at the axis, and possibly cross-cut the ridge

axis, exhuming a volume of plutonics not necessarily matching that emplaced on the conjugate side. This is testable by incorporating new weakening laws (e.g. melt-assisted strain localization) into our model.

### **5.5. Conclusions and perspectives**

Our modeling results provide a new conceptual framework for interpreting relations between magmatism and faulting at slow- to intermediate-spreading MORs. Specifically, we argue that fault style is primarily controlled by the rate of diking in the brittle lithosphere, while lithological variations in both the brittle lithosphere and in the underlying ductile asthenosphere are controlled separately by intrusion rates that are unique to each layer. Our results allow us to interpret OCC formation in the context of both rate and location of melt supply at the segment scale and in a four-dimensional framework. The model could be made more relevant to MOR settings by incorporating more coupling between thermal structure and melt emplacement. For instance, instead of being fixed at the center of the domain, the injection zone could be allowed to move freely across the model domain, spontaneously localizing above the shallowest point of the melting region. It would therefore be sensitive to lateral shifts in the thermal structure driven by asymmetric extension. Furthermore, one could introduce some degree of coupling between the  $M$  parameter and the volume of melt predicted from the ridge thermal structure. The thermal structure could also be used to infer how much melt should be trapped and emplaced in the ductile asthenosphere vs. in the brittle lithosphere.

Finally, the next major step in numerical modeling of MOR tectonics will be the development of three-dimensional thermo-mechanical models, which has only recently been made possible by advances in computing power [Gerya, 2010b]. Such a model would enable us to investigate: (1) the 3D geometry of normal faults and their interactions at the segment-scale, (2) their response to along-axis variations in the rates of magma intrusion, lithospheric thickness, rate of off-axis lithospheric thickening, and (3) the effect of a transform boundary condition on the development of detachment faults and inside-corner highs.





## **Chapter 6:**

### **The effect of lithospheric thickness variations on the three-dimensional growth of normal faults**

#### **Abstract**

Normal faulting at extensional plate boundaries is by essence a three-dimensional process that is modulated by spatial variations in lithospheric properties and magmatic activity. This chapter presents simulations of three-dimensional normal fault growth in a lithosphere that thickens along- and across-axis at variable rates. These simulations are carried out using HiPStER (Highly-Parallel Stokes with Exotic Rheologies), a newly developed particle-in-cell finite-difference code that solves for incompressible flow with spontaneous localization of deformation in a 3-D visco-elasto-plastic continuum. We explore the effect of lithospheric geometry on fault development by varying (1) the average along-axis thickness of the lithosphere, (2) the gradient of along-axis lithospheric thickening, and (3) the gradient of across-axis thickening. For all lithospheric geometries with off-axis thickening, we find that strain first localizes onto two inward facing normal faults. These faults define an axial valley that gets wider as the lithosphere thickens toward the segment ends. However, in cases where the average lithospheric thickness is  $< 15$  km, extension is also accommodated on two additional inward-facing faults at the thin segment center. These auxiliary faults then propagate toward the segment ends at a rate that correlates negatively with the gradient of along-axis lithospheric thickening. In the simulation characterized by the highest relative along-axis thickening (thickness increasing from 6 to 14 km over 40 km), faults nucleate in both the thin and the thick part of the segment, but do not link with one another. Deformation is relayed along-axis through a complex *en échelon* structure. In light of these new results, we discuss the applicability of 2-D scalings to three-dimensional systems, and outline the future work toward realistic 3-D models of tectono-magmatic interactions at mid ocean ridge and continental rift segments.

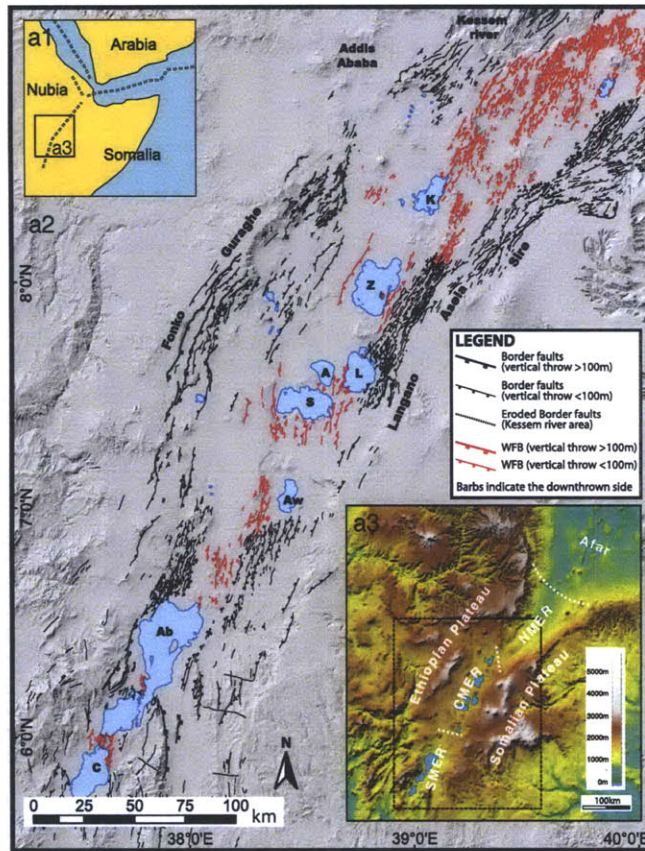
## 6.1. Introduction

Extensional plate boundaries are linear features that span distances much greater than their characteristic width (10–100 km). For several decades, this characteristic has warranted the use of 2-D cross-axis numerical models to elucidate the first-order mechanics of rifting. However, over such distances ( $10^3$  km) the lithosphere often displays variability in its properties and 3-D geometry on a variety of scales.

A spectacular manifestation of intermediate-scale variability ( $\sim 10^2$  km) is the along-axis segmentation of mid-ocean ridges (MORs) [Searle and Laughton, 1977; Macdonald *et al.*, 1984; 1988; 1991; Tucholke and Lin, 1994] and continental rifts [Mohr and Wood, 1976; Bosworth, 1985; Morley *et al.*, 1990; Hayward and Ebinger, 1996]. At young, magma-poor portions of continental rifts (e.g., southern and central Main Ethiopian Rift), segmentation is defined by along-axis discontinuities in the traces of the major rift-bounding faults (Figure 6-1) [Hayward and Ebinger, 1996], and there is limited lateral offset between segments. At more magmatically robust rifts and MORs, discrete rift or ridge segments are laterally offset from one another by a zone of shear deformation. Discontinuities between MOR segments can take the form of either a transform fault bounding first-order segments or a non-transform offset bounding higher-order segments [Macdonald *et al.*, 1991] (Figures 6-1b and 6-2). While the origin of these segment-bounding offset zones is debated, short wavelength (10– $10^2$  km) variability in lithospheric thickness at the segment scale is well documented, especially at slow-spreading MORs [e.g., Kuo and Forsyth, 1988; Tolstoy *et al.*, 1993; Cannat, 1996]. Such short wavelengths are commensurate with the characteristic across-axis length scales of individual normal faults, i.e., the flexural wavelength of the lithosphere. Extensional faulting at the segment scale is therefore a three-dimensional process that is likely modulated by along-axis gradients in lithospheric properties, as well as gradients in the activity of geological processes such as magmatism or hydrothermal cooling [Shaw and Lin, 1996].

The example of slow-spreading MOR segments perfectly illustrates the need for 3-D models of fault evolution (Figure 6-2). A defining characteristic of slow-spreading MOR segments is their strong along-axis variability in morphology and fault style, with wider axial valleys and more widely spaced, longer-lived faults close to segment ends

a.



b.

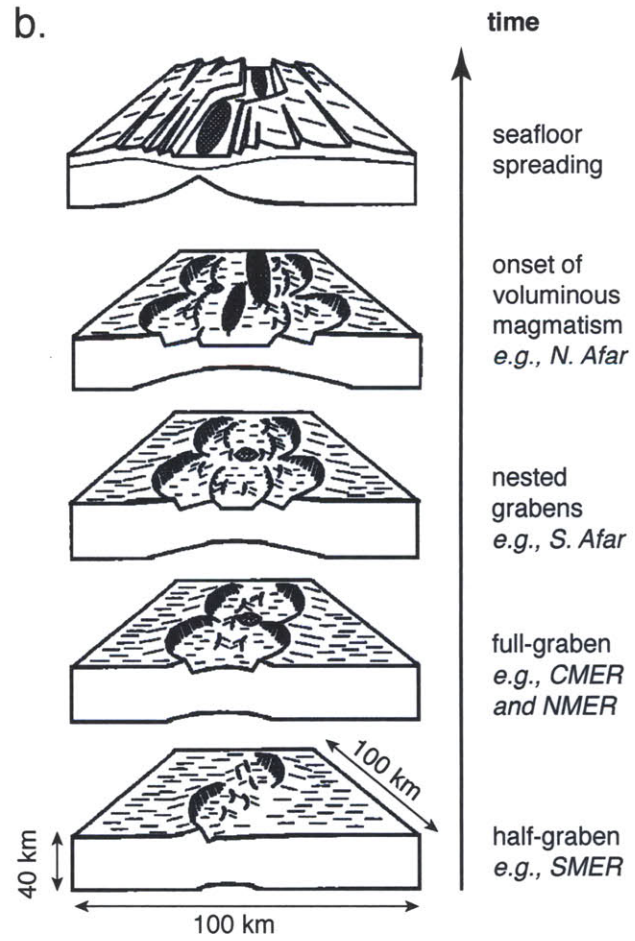


**Figure 6-1.** a. Tectonic map of the Main Ethiopian Rift (MER), modified from Agostini et al. [2011]. (a1) Major plate boundaries in the vicinity of the Afar Triple Junction. (a2) Fault pattern of the MER superimposed on a digital elevation model (Shuttle Radar Topography Mission (SRTM) data). Border faults are shown in black and the Wonji Fault Belt (WFB, a set of faults affecting the rift floor) in red. A, Lake Abijata; Ab, Lake Abaya; Aw, Lake Awasa; C, Lake Chamo; K, Lake Koka; L, Lake Langano; S, Lake Shala; Z, Lake Ziway. (a3) Digital elevation model (SRTM data) of the Ethiopian Rift showing the main rift sectors (from south to north): southern Main Ethiopian Rift (SMER), central Main Ethiopian Rift (CMER), northern Main Ethiopian Rift (NMER), Afar. b. Schematic bloc diagrams of the evolution of rift segmentation in the sectors of the Main Ethiopian Rift and Afar rift system from south to north (bottom to top), with a slow-spreading mid-ocean ridge case (seafloor spreading) for comparison. Reproduced from *Hayward and Ebinger* [1996].

[e.g., *Tucholke and Lin*, 1994; *Rabain et al.*, 2001]. These features have been linked to segment-scale variations in lithospheric properties and thermal regime, as inferred from residual gravity anomalies [*Kuo and Forsyth* 1988; *Lin et al.*, 1990; *Detrick et al.*, 1995], seismic velocity structure [*Tolstoy et al.*, 1993; *Hooff et al.*, 2000], and microseismicity [*Kong et al.*, 1992; *Barclay et al.*, 2001]. Specifically, segment centers are typically characterized by thicker magmatic crust and a hotter thermal regime leading to thinner lithosphere [*Phipps Morgan and Forsyth*, 1988], while segment ends are characterized by large tracts of exhumed serpentinitized mantle and thicker lithosphere [*Cannat*, 1996]. *Shaw and Lin* [1993]; *Shaw and Lin* [1996], *Escartin et al.* [1997] and *Behn et al.* [2002a] used mechanical models to relate along-axis changes in fault styles to changes in lithospheric thickness, lithologies and strength. This problem was also addressed with 2-D numerical models that spontaneously localize deformation [*Poliakov and Buck*, 1998; *Behn et al.*, 2004]. This class of models became particularly successful at predicting fault spacing and offset when the effects of magmatic injection at the ridge axis were considered [*Buck et al.*, 2005; *Tucholke et al.*, 2008; *Behn and Ito*, 2008; *Ito and Behn*, 2008]. These studies suggest that the main effect of magmatism is to set the rate at which normal faults migrate off-axis through thicker lithosphere where it becomes mechanically difficult to sustain slip. Consequently, as detailed in Chapter 5 of this thesis, elevated rates of melt injection above the brittle-ductile transition favor the growth of numerous

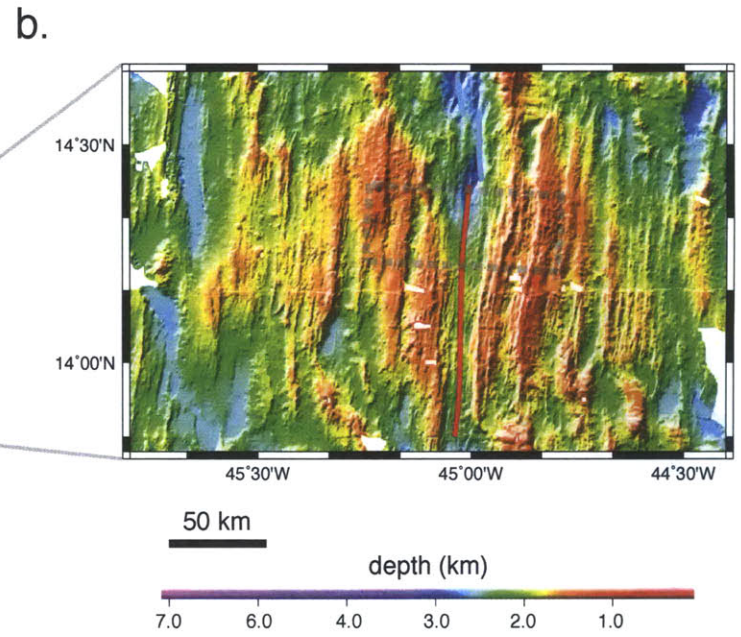
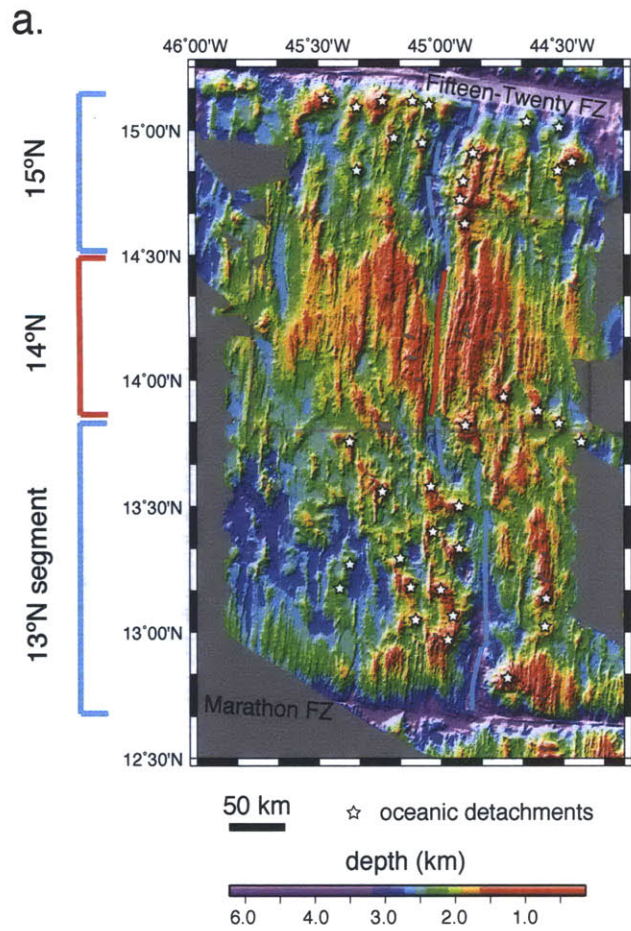


**Figure 6-2.** a. Bathymetry of the Mid-Atlantic Ridge between the Fifteen-Twenty and Marathon Fracture Zones, which consists of three segments outlined by brackets on the left side of the map. The colored lines indicate the ridge axis. Following the classification of *Escartin et al.* [2008], a red line denotes a portion of the ridge characterized by symmetric accretion, and a blue line indicates asymmetric accretion along multiple detachment faults (white stars). b. Close up on the 14°N symmetric segment, which features a typical hourglass shape with multiple closely spaced faults near the shallow segment center. The dashed black box indicates the horizontal extent of the numerical models presented in this chapter (~ half a segment).

short-lived faults near the segment center, while moderate rates of melt emplacement close to segment ends enable the formation of long-lived detachments. However, the mechanism by which extensional deformation is relayed along-axis between these two end-member fault styles is still unknown, as it cannot be addressed with 2-D models. One possibility is that long-lived detachments have a limited along-axis extent, and do not link with steeper, short-offset faults that span greater along-axis distances. This scenario could explain why mature detachments form isolated oceanic core complexes that have a finite extent along-axis and a characteristic spacing of ~20 km (Figure 6-2a). Such a model would require very steep along-axis gradients in fault offset along detachment faults, and complex relay structures. An alternative scenario, put forward by *Reston and Ranero* [2011], proposes that low-angle detachments have a large along-axis extent, and underlie steep short-offset faults characteristic of segment centers. While a long-lived detachment cutting through the entire segment constitutes a straightforward geometry for along-axis fault linkage, 2-D models suggest that sustaining the growth of a detachment while accommodating more than 60% of the full spreading rate by magmatic injection at segment centers is mechanically difficult.

Computational geodynamic modeling provides a means to assess the mechanical feasibility of these different scenarios, however to date a fully consistent 3-D numerical model of faulting at the segment scale is still lacking. The reason for this is that modeling the evolution of normal faults in 3-D is a computationally challenging endeavor. To date, only a handful of codes have been developed to model extension in three dimensions. Early efforts consisted of visco-elastic models that did not allow strain

localization along discrete faults [e.g., *van Wijk and Blackman*, 2005]. Since then, most codes have focused on large-scale ( $\geq 10^2$  km) processes such as rift segmentation, interaction among individual segments, and the growth of transform faults [e.g., *Beutel*, 2005; *Choi et al.*, 2008; *Gerya*, 2010b; *Püthe and Gerya*, 2013]. Due to their large-scale approach, these models could not properly resolve individual near-axis normal faults. *Allken et al.* [2011; 2013] considered lower-scale systems and successfully modeled the interactions between individual rift-bounding normal faults. However, *Allken et al.* [2011; 2013] approximated the brittle faulted layer as a visco-plastic medium, which raises questions regarding the geological applicability of their results, as detailed in Chapter 4 of this thesis. Finally *Le Pourhiet et al.* [2012], also using a visco-plastic approximation, studied the 3D geometry of deformation around a continental detachment fault, but did not focus on fault interactions in 3D, and instead localized detachment fault growth along-axis by imposing varying rates of extension.

In this chapter we are concerned with three-dimensional normal fault growth and the degree of along-axis continuity of faults at the scale of an individual extensional segment ( $\leq 10^2$  km), which is characterized by both along- and across-axis variations in lithospheric properties. We start by presenting our numerical approach to modeling 3-D flow in a visco-elasto-plastic continuum, and apply our models to an elasto-plastic lithosphere of varying along-axis thickness that undergoes axis-perpendicular extension. We interpret these models in terms of the resulting patterns of strain localization and along-axis fault growth. Finally, we discuss the applicability of our results to real ridge systems, and outline future steps toward fully consistent 3-D models of tectonic faulting at slow MORs and continental rifts.

## **6.2. Numerical methodology: the HiPStER approach**

Modeling Stokes flow with visco-elasto-plastic rheologies is the central problem in computational geodynamics, and poses numerous challenges. In general, to reach reasonable resolution,  $\sim 50$  elements are needed in each direction, with (ideally) more elements in regions of highly localized deformation (faults). This means that four equations (Continuity and Stokes in 3 directions) must be discretized and solved on  $\sim 10^5$  grid points, which places strong memory requirements on the hardware and requires

parallel computation. Further, such large problems render the use of direct solvers commonly used for 2-D models (e.g., LU decomposition) highly impractical due to their limited scalability. Iterative solvers therefore constitute the method of choice. However, the efficacy of a given method is highly problem-dependent, and identifying solvers that are well suited for the discretized Stokes flow equations is an active area of research [e.g., *May and Moresi, 2008*]. Here we outline our choice of discretization method (finite difference with Lagrangian markers), rheological parameterization, and iterative solvers (Krylov method with field splitting-based preconditioning).

### 6.2.1. Governing equations and discretization

Our simulations were carried out using HiPStER (Highly-Parallel Stokes with Exotic Rheologies), a 3-D finite-difference / particle-in-cell code [*Harlow and Welch, 1965; Gerya and Yuen, 2003; 2007*] that was developed based on the methodology of *Gerya* [2010a] and relies heavily on the PETSc (Portable Extensible Toolkit for Scientific computing) computational library [*Balay et al., 1997*]. HiPStER solves for conservation of mass and momentum in a 3-D continuum assuming material incompressibility. The corresponding (Stokes) equations are written:

$$\frac{\partial v_i}{\partial x_i} = 0 \quad (6.1)$$

$$\frac{\partial \sigma'_{ij}}{\partial x_j} - \frac{\partial P}{\partial x_i} + \rho g_i = 0 \quad (6.2)$$

where  $v_i$ ,  $\sigma'_{ij}$ , and  $P$  denote velocities, deviatoric stresses, and pressure, respectively, and repeated indices imply summation from  $i = 1$  to  $i = 3$ .

We treat the material as an incompressible Maxwell visco-elastic solid of viscosity  $\eta$  and shear modulus  $G$ . Following the procedure outlined in Section 4.2.2 of Chapter 4, we discretize the Eulerian component of the deviatoric stress change involved in the expression of the total strain rate (Equation 4.4), over a visco-elastic time step  $\Delta t$ . Stress advection and rotation is handled by markers. This approach yields the following stress-strain relation:

$$\sigma'_{ij} = 2\eta Z \dot{\epsilon}_{ij} + (1-Z)\sigma'_{ij}(t-\Delta t) \quad (6.3)$$

where  $Z$  denotes a visco-elastic ratio:

$$Z = \frac{G\Delta t}{G\Delta t + \eta} \quad (6.4)$$

The visco-elastic time step  $\Delta t$  can be chosen such that certain portions of the domain behave elastically ( $\Delta t \ll$  Maxwell time scale;  $Z = 0$ ) or viscously ( $\Delta t \gg$  Maxwell time scale;  $Z = 1$ ).

Plasticity is implemented by weakening the material viscosity wherever the second invariant of the deviatoric stresses exceeds a yield stress. The failure law is a smooth approximation of the Mohr-Coulomb criterion where cohesion decreases with accumulated plastic strain. A healing mechanism favors the build-up of plastic strain in localized shear zones as opposed to broad regions of yielding [*Poliakov and Buck, 1998*]. The detailed implementation of plasticity is described in Section 4.2.3 of Chapter 4.

Upon inserting Equation (6.3) into Equation (6.2), conservation of momentum can be expressed as

$$\frac{\partial}{\partial x_j} \left( \eta Z \left( \frac{\partial v_i}{\partial x_j} + \frac{\partial v_j}{\partial x_i} \right) \right) - \frac{\partial P}{\partial x_i} + \rho g_i = - \frac{\partial}{\partial x_j} \left( (1-Z)\sigma'_{ij}(t-\Delta t) \right) \quad (6.5)$$

It should be noted that under geological conditions, the numerical values of the unknowns ( $v_i, P$ ) expressed in S.I. units likely differ by many orders of magnitude (e.g.,  $v_i \sim 10^{-10}$  m/s compared to  $P \sim 10^8$  Pa). Further, the coefficients multiplying the unknowns in Equations (6.5) and (6.1) scale either as the inverse of a length or as a viscosity over a length squared, and thus can also differ by many orders of magnitude. These properties typically result in poor conditioning of the linear systems involved in solving Equations (6.1) and (6.2) numerically, and make it difficult to assess errors with norms that involve the entire solution vector  $X = [v_i, P]^T$ . To prevent such problems, we rewrite Equations (6.1) and (6.2) in non-dimensional form adopting the conventions listed in Table 6-1.

Parameter	Scale
Length	$H_0$ , height of domain
Viscosity	$\eta_0$ , highest viscosity in domain
Density	$\rho_0$ , highest density in domain
Velocity	$V_0$ , representative velocity boundary condition
Pressure, stresses, and elastic moduli	$\eta_0 V_0 / H_0$ , viscous stress scale
Time	$H_0 / V_0$

**Table 6-1.** Characteristic scales chosen to non-dimensionalize the Stokes and continuity equations.

The system of equations to be solved becomes:

$$\frac{\partial \tilde{v}_i}{\partial \tilde{x}_i} = 0 \quad (6.6)$$

and

$$\frac{\partial}{\partial \tilde{x}_j} \left( \tilde{\eta} Z \left( \frac{\partial \tilde{v}_i}{\partial \tilde{x}_j} + \frac{\partial \tilde{v}_j}{\partial \tilde{x}_i} \right) \right) - \frac{\partial \tilde{P}}{\partial \tilde{x}_i} + St \tilde{\rho} = - \frac{\partial}{\partial \tilde{x}_j} \left( (1-Z) \tilde{\sigma}'_{ij}(\tilde{r}-\Delta \tilde{r}) \right) \quad (6.7)$$

where the tilde denotes variables that are non-dimensional and  $St$  denotes the ratio of the characteristic Stokes velocity to the chosen velocity scale:

$$St = \frac{\rho_0 g H_0^2}{\eta_0 V_0} \quad (6.8)$$

Equations (6.6) and (6.7) are discretized using a conservative finite difference scheme on a three-dimensional staggered grid [Gerya, 2010a]. However, rather than assembling a matrix of coefficients as in the 2-D method employed in Chapters 2-4, we make use of the PETSc framework and write our discrete system in the form:

$$F(X) = 0 \quad (6.9)$$

where  $F$  is a residual function and  $X$  the solution vector containing the velocity and pressure values attached to all grid points. In the present version of HiPStER, the effective viscosity ( $\tilde{\eta}$ ) that appears in Equation (6.7) is calculated outside the residual

function and then supplied to  $F$  prior to solving Equation (6.9). This approach consists of performing several "Picard iterations" on viscosity ( $\tilde{\eta}$ ) within a single time step.

Each Picard iteration consists of solving Equation (6.9), and using the velocity and pressure solution to calculate the corresponding strain rate and stress fields. These are used to update the viscosity field following the appropriate creep / plasticity laws. This updated viscosity field is then fed to the residual function in order to generate the next solution, and so on. After several of these Picard iterations the system converges to a solution where stresses, viscosities and strain rates are consistent with one another. For the class of problems presented in this paper, we found that performing three Picard iterations per time step was sufficient to allow consistent solutions.

While the residual function  $F$  changes with each new Picard iteration (due to the updated viscosity field), it remains a first-order polynomial function of the discrete unknowns through the entire process. Consequently, each Picard solve can be carried out with a single iteration of Newton's method with a zero initial guess. This amounts to solving the linear system

$$JX = F(0) \quad (6.10)$$

where  $J$  refers to the Jacobian of  $F$

$$J_{ij} = \frac{\partial F_i(X^{(k)})}{\partial X_j^{(k)}} \quad (6.11)$$

The Jacobian is calculated exactly via finite difference, given the linearity of  $F$ . While conceptually this approach is no different than the matrix approach of Chapters 2-4, the residual formulation enables (1) the use of matrix-free operators, which are more computationally efficient when dealing with large systems, and (2) a straightforward implementation of a non-linear residual to be solved with a full Newton's method for future applications. This can all be done within PETSc's SNES (Scalable Nonlinear Equations Solver) framework.

The detailed numerical strategy to solve the linear system in Equation (6.10) is presented in Section 6.2.2. Once enough Picard iterations have been performed and an acceptable solution has been obtained, stresses and plastic strain are updated on Lagrangian particles (markers). The new velocity field is used to advect the markers with a simple first-order Euler scheme over an advection time step  $\Delta t_m$ , which serves as the

actual step for time evolution in the model.  $\Delta t_m$  is set so that markers do not travel further than 60% of the smallest cell size at each advection step. Finally, the advected marker properties are interpolated back to the grid to prepare for the next time step solve [Gerya, 2010a].

### 6.2.2. Numerical strategy for solving the linear system

In order to solve the large sparse linear system in Equation (6.10) we rely on the GMRES algorithm, which is a Krylov subspace method well suited for iteratively solving non-symmetric systems using matrix-vector multiplications only. The rate of convergence and, ultimately, the success of a Krylov method is largely dependent on the spectral properties of the matrix  $J$ . Broadly speaking, Krylov methods work best on matrices whose eigenvalues do not differ by many orders of magnitude. Such matrices are termed "well conditioned". A common strategy to improve the conditioning of a matrix is to apply a preconditioning operator to the system. The idea is to multiply both sides of Equation (6.10) by a preconditioner  $P_C$  and solve

$$(P_C J)X = P_C F(0) \quad (6.12)$$

with  $P_C$  carefully chosen so that  $(P_C J)$  is better conditioned (and is therefore easier to invert with a Krylov method) than  $J$ . Ideally  $P_C$  should resemble  $J^l$ .

To assemble an efficient preconditioner for Equation (6.10), we take a closer look at the structure of  $J$ , which represents a saddle-point Stokes system of the form:

$$JX = \begin{pmatrix} K & G \\ G^T & 0 \end{pmatrix} \begin{pmatrix} v \\ P \end{pmatrix} = \begin{pmatrix} rhs \\ 0 \end{pmatrix} \quad (6.13)$$

where  $K$ ,  $G$ , and  $G^T$  are blocks representing the discrete stress divergence, gradient and divergence operators, respectively. Following the methodology of *May and Moresi* [2008], we precondition  $J$  by applying a Schur complement approach, which rearranges  $J$  as an upper-triangular matrix

$$\hat{J} = \begin{pmatrix} K & G \\ 0 & S \end{pmatrix} \quad (6.14)$$

where the Schur complement block  $S$  writes

$$S = -G^T K^{-1} G \quad (6.15)$$

We note that the calculation of  $S$  requires inverting the  $K$  block. However, once this is done, the only remaining task to fully invert  $\hat{J}$  is to invert  $S$ . This is because upon inverting  $S$ , the pressure solution can be substituted into the first row of  $\hat{J}$ , and the velocity solution can be obtained by applying  $K^{-1}$ , which has already been calculated to obtain  $S$ . We make use of PETSc's fieldsplit preconditioner [Brown *et al.*, 2012] to target the various blocks of  $J$  individually. Specifically, we obtain  $K^{-1}$  by applying the GMRES algorithm on  $K$  preconditioned by the Jacobi iterative method. We then invert the Schur complement  $S$  via another application of GMRES, this time preconditioned by a least-squares commutator (LSC), which is known to perform well with Stokes problems involving spatially variable viscosity with sharp contrasts [Elman *et al.*, 2006; May and Moresi, 2008]. The basic idea of LSC preconditioning is that a good approximation of  $S^{-1}$  can be obtained from

$$\hat{S}^{-1} = (G^T G)^{-1} G^T K G (G^T G)^{-1} \quad (6.16)$$

For viscous incompressible flow problems,  $L = G^T G$  is a discrete Laplacian operator. A low-accuracy estimate of  $(G^T G)^{-1}$  is obtained with the Jacobi method.

The succession of operations outlined above enables us to assemble a preconditioner  $P_C$  that approximates  $J^{-1}$ . Once this is done, the preconditioned system (Equation 6.12) is solved with a GMRES method, which we refer to as "outer GMRES" to distinguish it from the two "inner GMRES" necessary to assemble  $P_C$ .

### 6.3. Numerical experiments of fault evolution in a brittle layer of varying thickness

To investigate the initiation and growth of normal faults in a lithosphere of varying thickness, we conducted 6 simulations of faulting in a 3-D box (Figure 6-3) spanning 100 km along the extension direction ( $x$ -direction, divided into 100 cells) axis, 40 km perpendicular to the extension ( $y$ -direction, 30 cells), and 40 km vertically ( $z$ -direction, 40 cells). It should be noted that while the code operates on non-dimensional quantities, for clarity we shall refer to the various simulation parameters in their dimensional form through the rest of this chapter.

Our model lithosphere is a brittle incompressible elasto-plastic layer of density  $3300 \text{ kg}\cdot\text{m}^{-3}$ , viscosity  $10^{24} \text{ Pa}\cdot\text{s}$  and shear modulus 33 GPa (the visco-elastic time step is

set so that  $Z \sim 0$  in this layer, see Equation 6.4). Its initial thickness  $H(x,y)$  varies spatially, but is systematically thinnest along an extension-perpendicular line in the middle of the domain, which defines the ridge axis. The lithosphere is sandwiched between two weak ( $10^{21}$  Pa·s) viscous layers: a 10 km-thick ocean (density  $1000 \text{ kg}\cdot\text{m}^{-3}$ ) and an underlying asthenosphere (density  $3300 \text{ kg}\cdot\text{m}^{-3}$ ). Incorporating a weak viscous ocean layer is an indirect way to model a stress-free seafloor, as detailed by *Crameri et al.* [2012]. Symmetric extension in the  $x$ -direction is applied orthogonally to the axis-parallel boundaries at a half-rate of  $1 \text{ cm}\cdot\text{yr}^{-1}$ . The axis-normal sides of the box are free-slip. A prescribed inflow of material through the top and bottom boundaries (also free-slip) compensates the outflow of ocean and rock through the sides.

Contrary to Chapters 2–4, we do not seed a weak fault in the lithosphere at the beginning of each run. Instead, we let deformation localize spontaneously along narrow shear bands within the first few time steps. In our formulation of plasticity, intact lithosphere has 100 MPa of cohesion, and cohesion decreases linearly with accumulated plastic strain  $\varepsilon_p$ . When  $\varepsilon_p$  has reached a critical value of 0.01 (roughly equivalent to a few tens of meters of slip on a shear zone with a width of a few elements), cohesion is reduced to 1 MPa. Such rapid weakening favors the spontaneous localization of many faults, which facilitates the study of fault interaction. Finally, a healing mechanism is implemented to reduce  $\varepsilon_p$  over a characteristic time scale of  $\sim 3000$  years in regions where it is not sustained by localized deformation [*Poliakov and Buck, 1998*]. This favors localized over diffuse yielding. Currently, we have not implemented any mechanism that would counteract the tectonic thinning of the lithosphere, such as conductive / hydrothermal cooling, or magma emplacement. The simulations are therefore conducted until the axial lithosphere has thinned such that individual shear zones can no longer be properly resolved. This typically occurs after  $\sim 25$  km of total extension for an average initial lithospheric thickness of 10 km along the axis. Each simulation is performed using 18 processors on WHOI's high performance computing cluster "Scylla", and takes  $\sim 1.5$  hours per time step (equivalent to  $\sim 1$  km of extension).

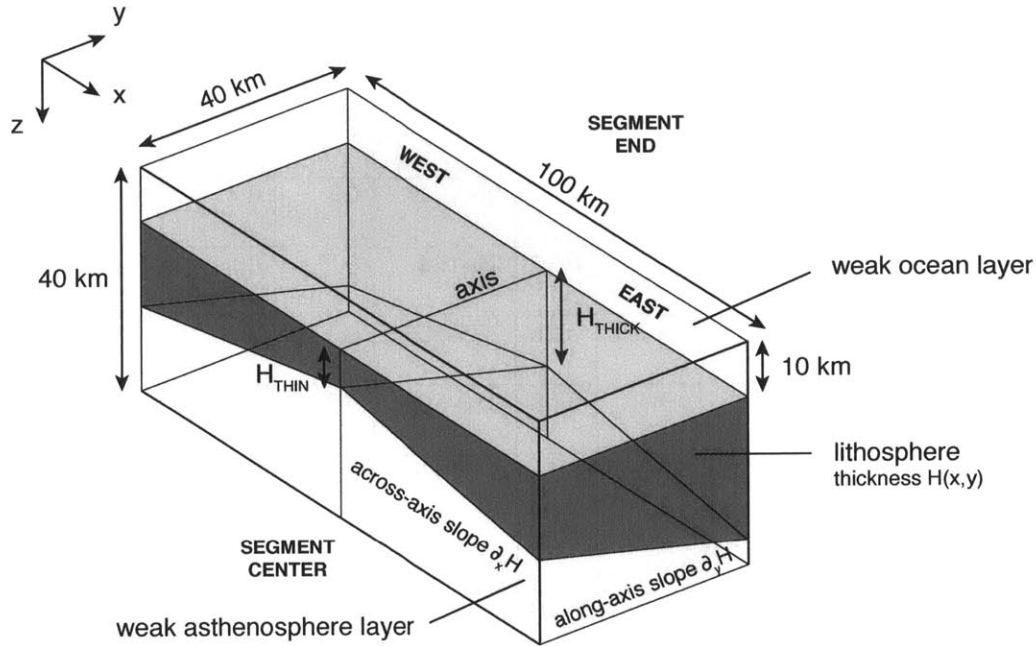


**Figure 6-3.** Schematic setup of our numerical simulations. Extension is applied in the  $x$ -direction on both sides of the domain, symmetrically. Compensating inflow of ocean and rocks is applied through the top and bottom. All boundaries are free-slip.

Our simulations investigate the effect of changing the rates of off-axis and along-axis lithospheric thickening ( $\partial_x H$  and  $\partial_y H$ , respectively), as well as the average lithospheric thickness along the axis ( $\bar{H}$ ). A summary of our run parameters is given in Table 6-2. Most of our simulations investigate the first-order geometry of half of an extensional segment, where the axial lithosphere is thinner at the center ( $H = H_{THIN}$  at  $y = 0$ ) and thicker at the end ( $H = H_{THICK}$  at  $y = 40$  km). In one simulation (*NOTCH*), the geometry is defined for a full 40 km-long extension segment, where the axial lithosphere is thinnest at  $y = 20$  km. A reference run (*FLAT*) features no variation in lithospheric geometry along axis. Our analysis of the model results focuses on (1) the geometry of the first faults that localize at the axis, (2) the sequence of faulting and degree of along-axis continuity of the various faults, and (3) the amount of curvature developed on individual faults.

Run Title	$H_{\text{THIN}}$ (km)	$H_{\text{THICK}}$ (km)	$\bar{H}$ (km)	$\partial_x H$	$L_D$ (km)	$\partial_y H$	RAT	Faults continuous along-axis?
<i>FLAT</i>	10	10	10	0.17	118	0	0	Yes
<i>SS</i>	8	12	10	0.17	94-141	0.1	0.4	Yes
<i>LS</i>	6	14	10	0.17	70-164	0.2	0.8	No
<i>SST</i>	15	20	17.5	0.08	375-500	0.125	0.29	Yes
<i>LST</i>	10	20	15	0.08	250-500	0.25	0.67	Yes
<i>NOTCH</i>	8, at center of box	12, on sides of box	10	0.17	94-141	0.2	0.4	Yes

**Table 6-2.** Summary of simulation parameters and results.  $L_D$  is the across-axis distance over which the lithosphere doubles its thickness from the axial value. RAT is the relative along-axis thickening, as defined in Section 6.5.2.

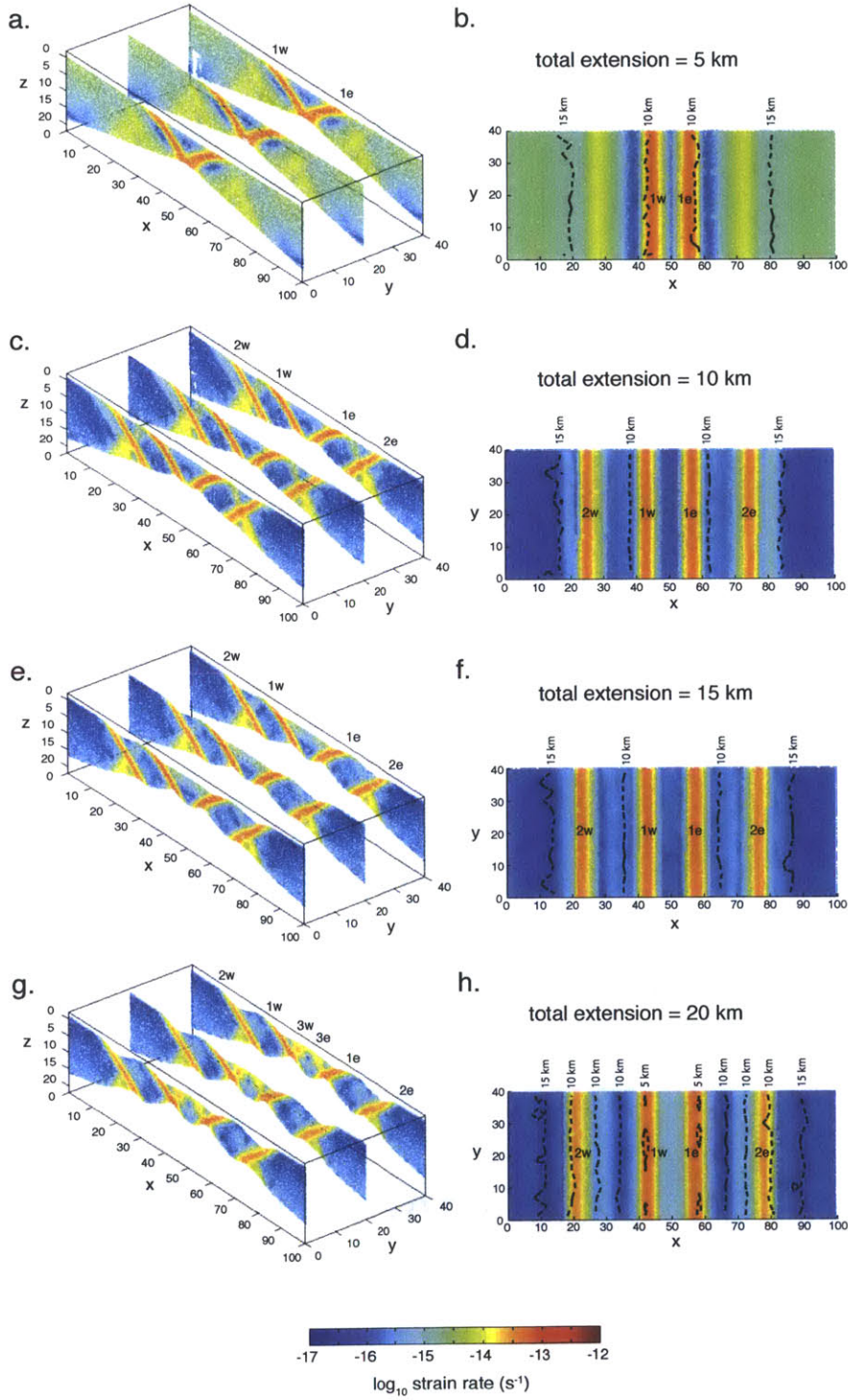
#### 6.4. Results

The results of our numerical simulations are presented in the form of strain rate maps highlighting strain localization (i.e., fault development) as a function of total extension (Figures 6-4 to 6-9). Interpretative maps showing the sequence of fault development in each simulation are presented in Figures 6-10 and 6-11. In the following, we number faults by their order of nucleation, with "w" and "e" referring to their location on the west or east side of the axis (Figure 6-3), corresponding to  $x < 50$  km and  $x > 50$  km, respectively.

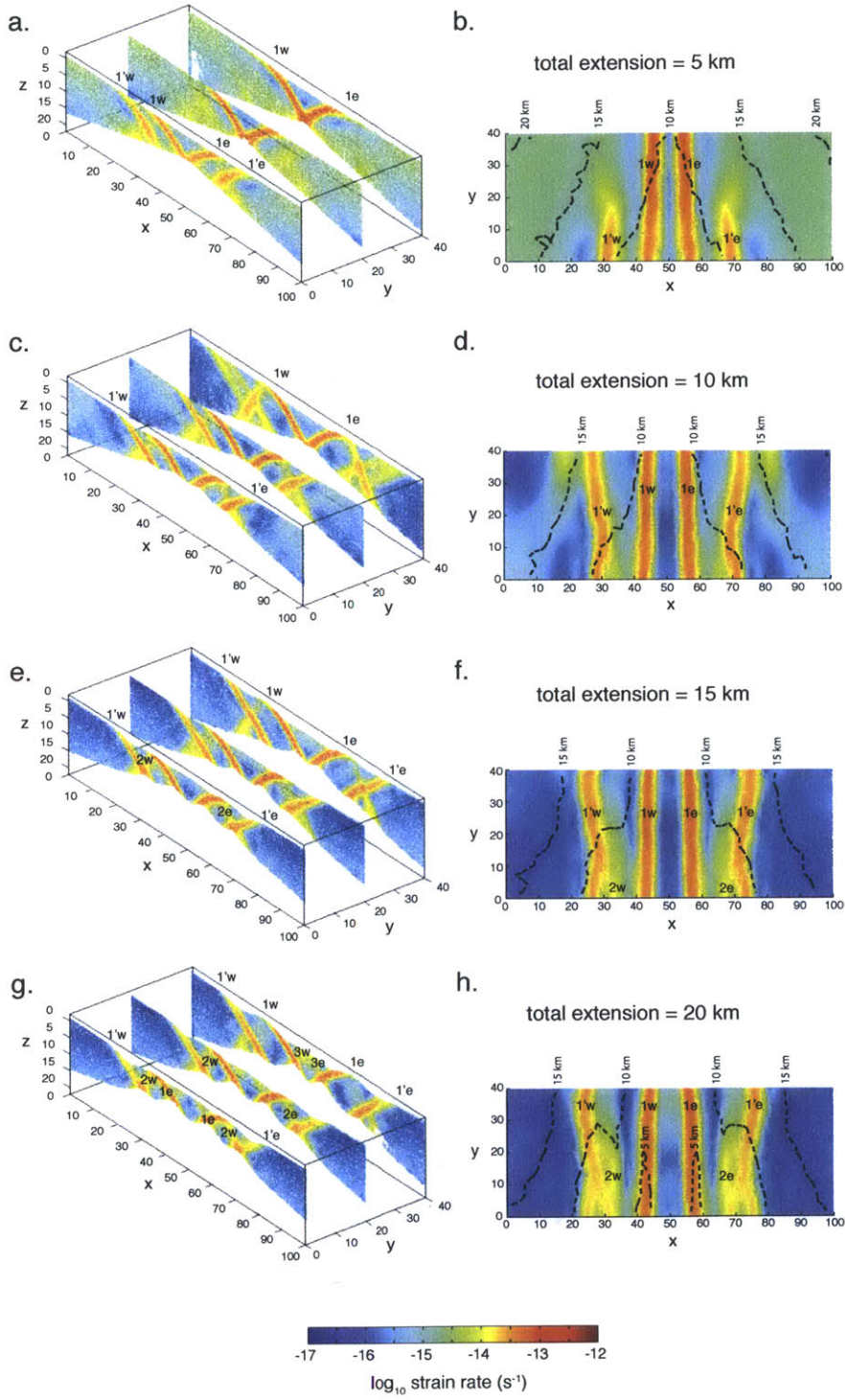
##### 6.4.1. Variations in along-axis slope with constant average lithospheric thickness

We first report the results from simulations with the same average lithospheric thickness along-axis ( $\bar{H} = 10$  km) and rate of across-axis thickening ( $\partial_x H = 0.17$ ), but increasing along-axis lithospheric slopes (*FLAT*, *SS*, *LS*; Table 6-2). The *FLAT* run has a constant axial lithospheric thickness of 10 km and features no variability in the along-axis direction.

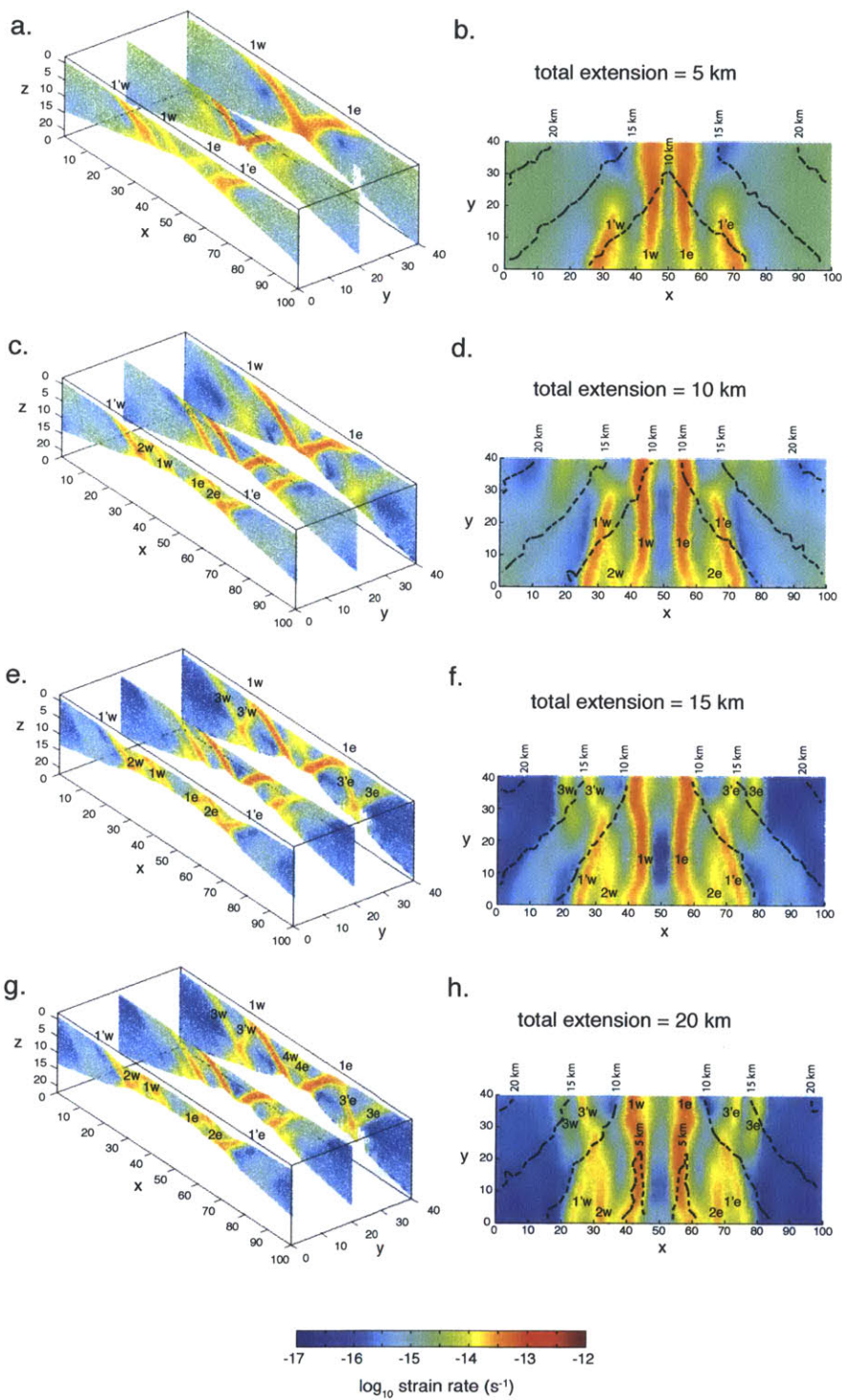
# FLAT



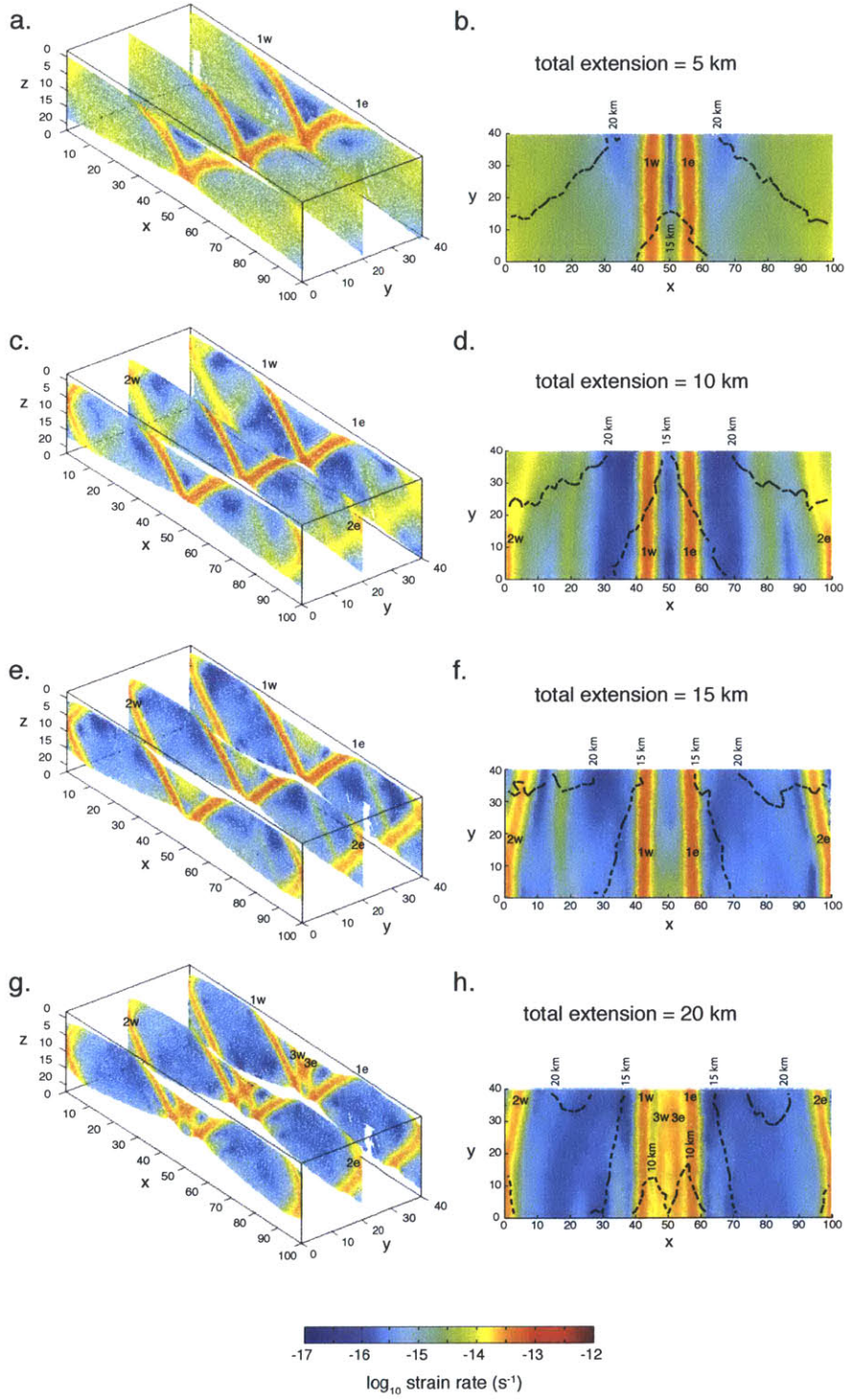
## Small Slope (SS)



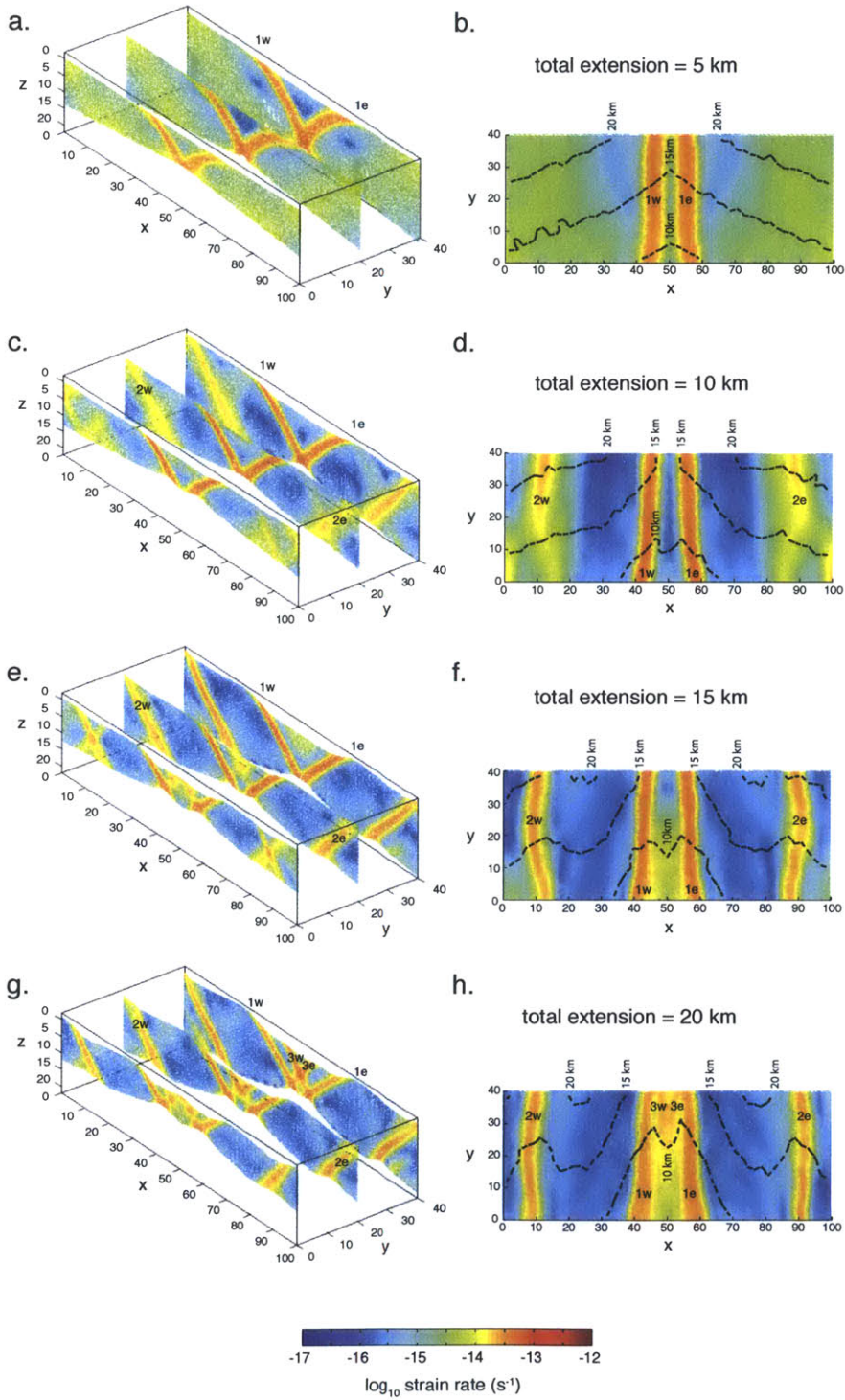
## Large Slope (LS)



## Small Slope, Thick lithosphere (SST)



## Large Slope, Thick lithosphere (LST)



# NOTCH

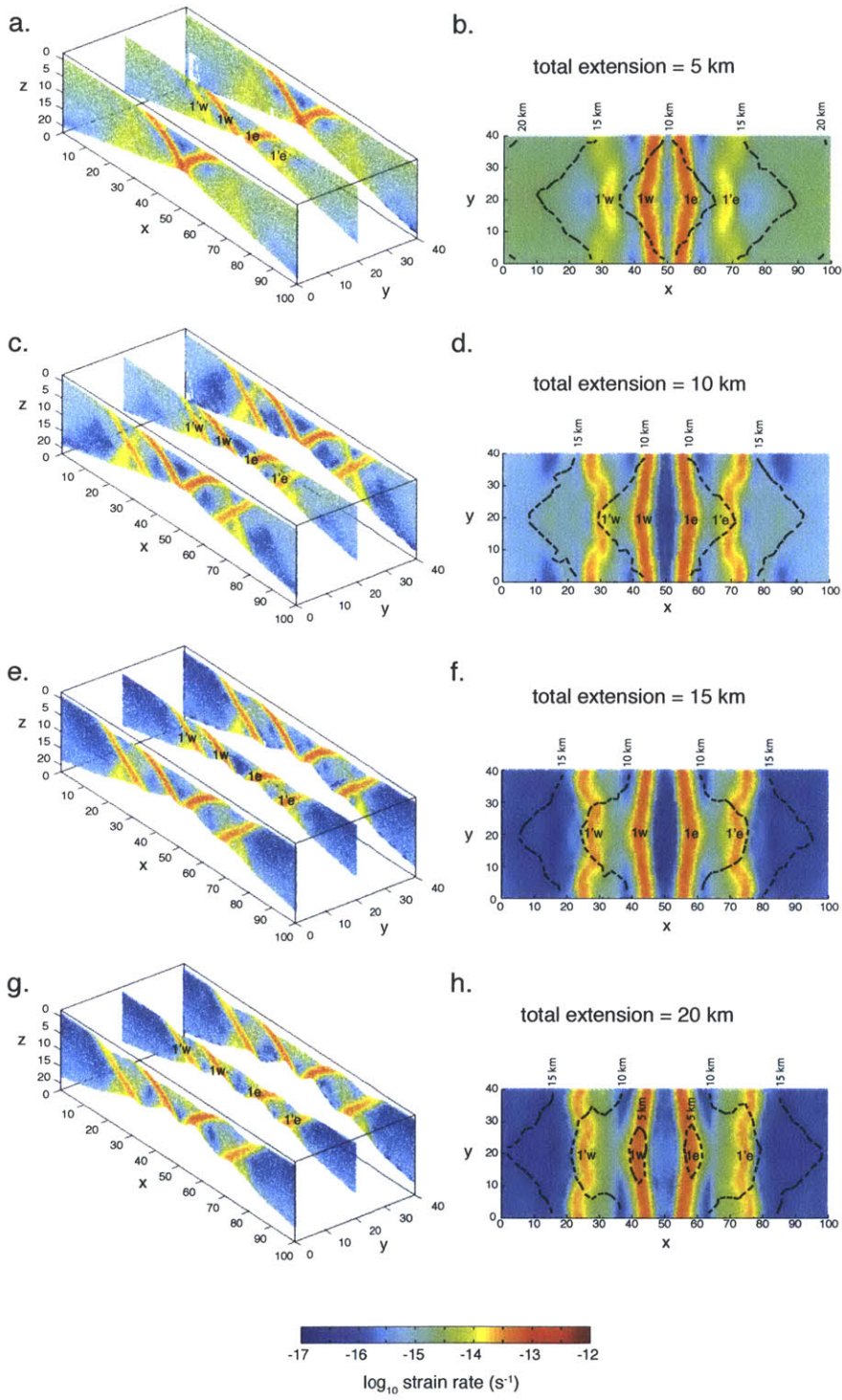


**Figure 6-4.** (p. 147) Snapshots of the strain rate field at 5, 10, 15 and 20 km of total extension in the  $x$ -direction from run *FLAT* (Table 6-2). In this run the axial lithosphere retains a 10 km thickness along the entire segment. The left column (a, c, e, g) shows strain rate plotted on markers selected along three vertical cross-axis slices at  $y = 0, 20$  and 40 km. In the right column (b, d, f, h) strain rate is plotted along a sloping plane cutting the sloping axial lithosphere at mid-level. The black dashed lines indicate contours of equal lithospheric thickness. Faults are numbered according to the chronology of their localization; "w" and "e" refer to the eastern and western side of the domain, respectively. All distances are in km.

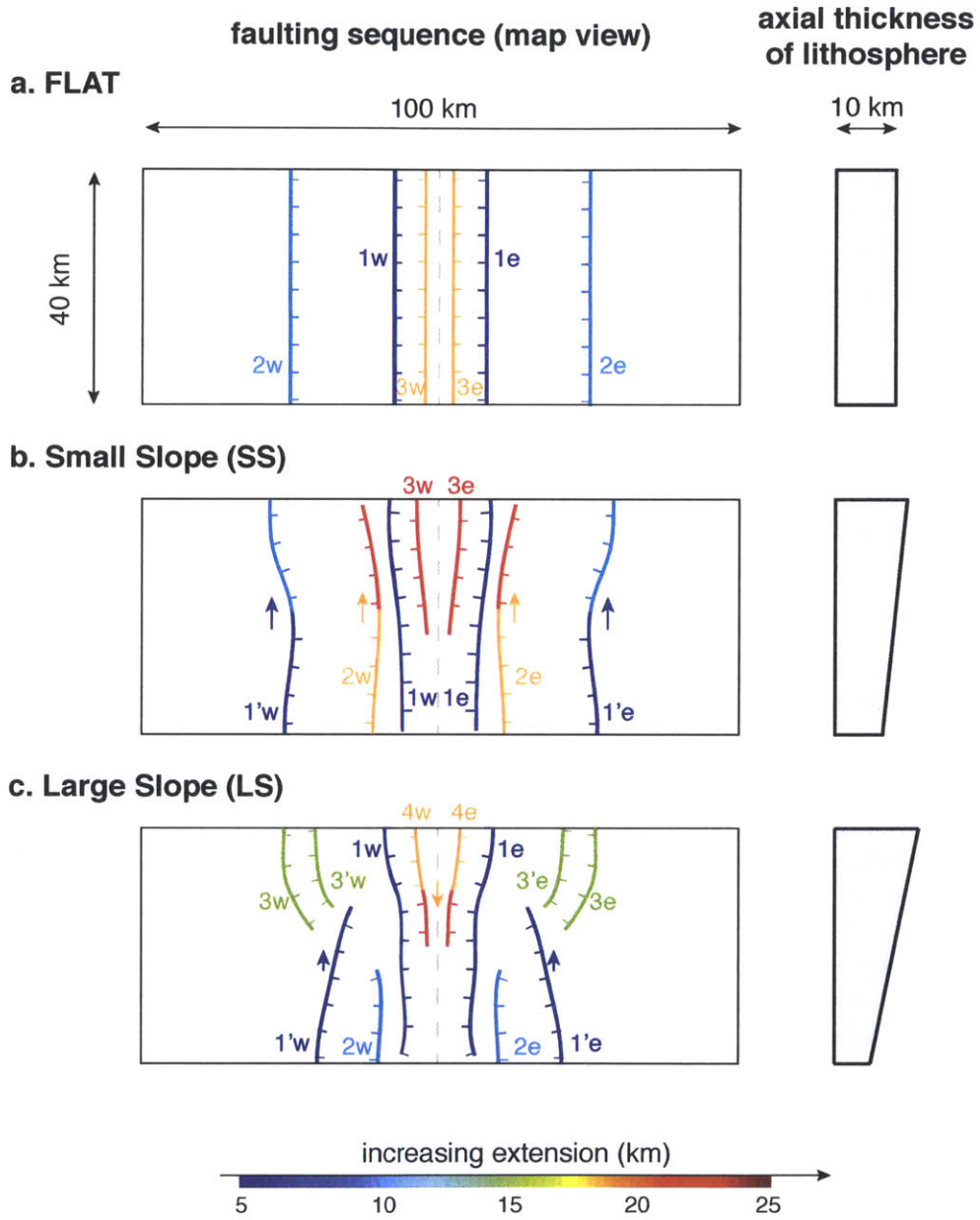
**Figure 6-5.** (p. 148) Snapshots of the evolving strain rate field from run *SS* (Table 6-2), where the axial lithosphere thickens from 8 to 12 km over 40 km along-axis. See caption of Figure 6-4 for details.

**Figure 6-6.** (p. 149) Snapshots of the evolving strain rate field from run *LS* (Table 6-2), where the axial lithosphere thickens from 6 to 14 km over 40 km along-axis. See caption of Figure 6-4 for details.

**Figure 6-7.** (p. 150) Snapshots of the evolving strain rate field from run *SST* (Table 6-2), where the axial lithosphere thickens from 15 to 20 km over 40 km along-axis. See caption of Figure 6-4 for details.

**Figure 6-8.** (p. 151) Snapshots of the evolving strain rate field from run *LST* (Table 6-2), where the axial lithosphere thickens from 10 to 20 km over 40 km along-axis. See caption of Figure 6-4 for details.

**Figure 6-9.** (p. 152) Snapshots of the evolving strain rate field from run *NOTCH* (Table 6-2), where the axial lithosphere is thinnest (8 km) in the middle of the box and thickens toward the sides (up to 12 km). See caption of Figure 6-4 for details.



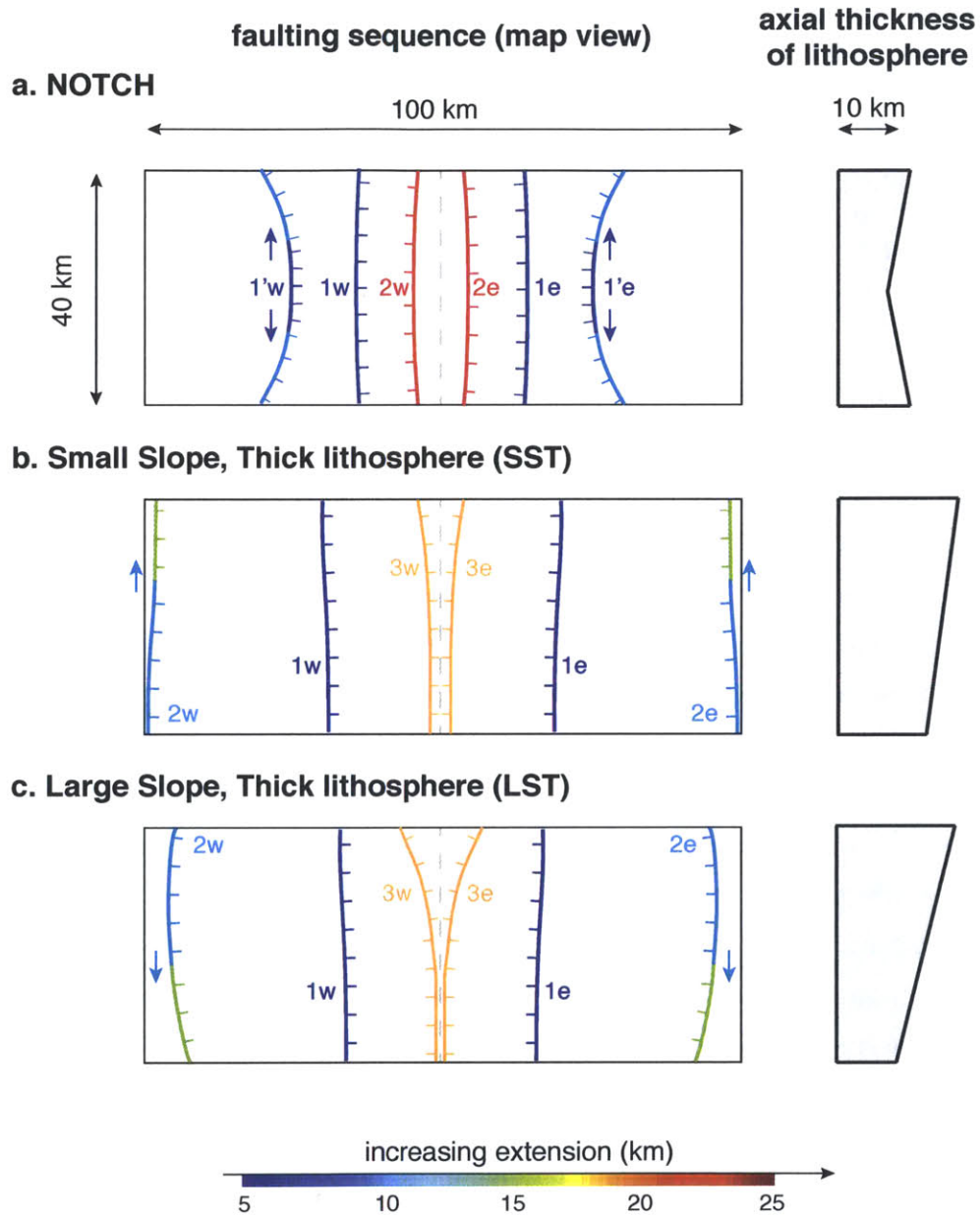


**Figure 6-10.** (p. 154) Interpretative maps showing the sequence of normal faulting in runs (a) *FLAT*, (b) *SS*, and (c) *LS* (see Table 6-2). Faults are indicated as colored lines, with barbs indicating the downthrow side. The color code corresponds to increasing amounts of total extension applied on the box, and indicates the chronology of fault development. Arrows indicate along-axis fault propagation that took place over more than 5 km of total extension. The axial profile of the initial lithosphere is shown on the side of each map.

**Figure 6-11.** (p. 155) Interpretative maps showing the sequence of normal faulting in runs (a) *NOTCH*, (b) *SST*, and (c) *LST* (Table 6-2). See caption of Figure 6-10 for details.

At the onset of extension deformation spontaneously localizes along two inward-dipping conjugate faults (faults 1w and 1e, Figure 6-4a, b). After ~10 km of extension a second pair of inward-dipping normal faults localizes 25 km off-axis (2w and 2e, Figure 6-4c, d). This does not result in the abandonment of the initial fault pair, but instead partitions the extensional strain onto 4 faults, which significantly thin the axial lithosphere down to ~6 km over a 15 km wide zone on either side of the axis. After 20 km of extension, a set of symmetric outward-dipping faults breaks through the thinned axial region (3w and 3e, Figure 6-4g). In all fault sets, the east and west faults localize synchronously along-axis, and are perfectly aligned in the extension-perpendicular direction (Figure 6-10a).

Next, we consider a case with a small along-axis lithospheric slope (Model *SS*,  $\partial_y H = 0.1$ ), which results in a lithospheric thickness that initially varies from 8 km at the segment center to 12 km at the segment end. In this simulation, strain partitioning varies along-axis from the onset of extension. Extension is initially accommodated on two conjugate inward-dipping faults that extend along the entire segment (1e and 1w). These central faults define a V-shaped axial valley that widens toward the segment end. At the segment end extension is accommodated entirely on the V-shaped faults. By contrast, at the center of the segment where the lithosphere is thinnest, two-inward dipping conjugate faults emerge ~25 km off-axis and take up the remainder of the extension not accommodated on the V-shaped faults (1'w and 1'e, Figure 6-5a, b). Initially, these additional faults extend only along the central half of the segment strike, but eventually propagate toward the thick end and break through the entire domain after 10 km of total

extension (Figure 6-5c, d). This corresponds to an along-strike fault propagation rate of  $\sim 4$  km per kilometer of extension. This pattern then holds through 20 km of total extension, when a new pair of outward-dipping faults (2w and 2e) forms at the segment center and propagates along-axis toward the segment end. These faults form immediately outboard of the central V-shaped faults that bound the axis (Figure 6-5g, h). Finally, after 25 km of total extension, an outward-dipping pair of faults (3w and 3e) starts to form at the end of the segment (where the axial lithosphere has been thinned to  $< 10$  km). These faults slowly propagate toward the segment center (Figure 6-10b).

The third scenario we consider incorporates an even larger along-axis lithospheric slope (Model *LS*,  $\partial_y H = 0.2$ ), which results in a lithospheric thickness that initially varies from 6 km at the segment center to 14 km at the segment end. The initial pattern of strain localization is similar to run *SS*, but with a more pronounced decrease in strain accommodation on the central V-shaped faults (1w and 1e) from segment end to segment center (Figure 6-6a, b). The outer set of inward dipping faults that initially localize at the segment center (1'w and 1'e) therefore accommodate more strain than their counterparts in Model *SS*. Faults 1'w and 1'e also propagate toward the thick end, but at a comparatively slower rate of  $\sim 2$  km per kilometer of extension. Their propagation is accompanied by the localization of two outward dipping faults 2w and 2e close to the segment center. Interestingly, the propagation of 1'w and 1'e is not axis-parallel, but slightly axis-ward as they break further toward the segment end (Figure 6-6d, f). The key difference between Models *LS* and *SS* occurs next. Before the slowly propagating 1'w and 1'e faults can reach the segment center, corresponding to  $\sim 15$  km of total extension, two pairs of conjugate faults (3w, 3e, 3'w, and 3'e) break symmetrically  $\sim 30$  km off-axis at the segment end (Figure 6-6e, f). Rather than linking with faults 1'w and 1'e, these two pairs of faults grow independently, and after 20 km of total extension the tips of faults 1', 3, and 3' (and their symmetrical counterparts on the conjugate side) overlap near  $y = 30$  km (Figure 6-6h). This is particularly evident from a plot of the extension parallel velocity field halfway through the lithosphere (Figure 6-12), which illustrates how extensional deformation is relayed near the fault tips (see Section 6.5.3 for discussion). This pattern continues over the next 5 km of extension, and we do not observe any linkage between the three faults.

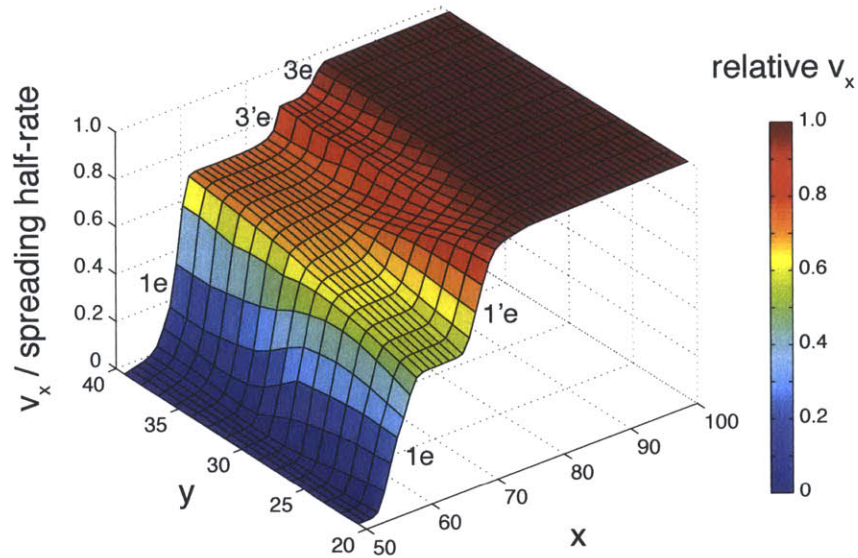


**Figure 6-12.** Rightward velocity ( $v_x$ ) of run *LS* after 20 km of extension on the right side of the axis ( $x > 50$  km) along a horizontal slice cutting through the thick half of the lithosphere ( $y > 20$  km) at  $\sim 4$  km below seafloor. The velocity is normalized by the spreading half rate. Faults correspond to sharp jumps in the velocity field and are numbered consistently with Figure 6-6 and 6-10c. Note that in the thick segment end ( $y = 40$  km) extension is taken up on 3 faults (1e, 3'e, and 3e) on the right side of the axis whereas closer to the segment center ( $y = 20$  km) extension is only taken up on faults 1e and 1'e. Regions of constant  $v_x$  represent rigid blocks bounded by faults.

#### 6.4.2. Variations in average lithospheric thickness

We next investigate the effect of increasing the average lithospheric thickness on fault behavior. Model *SST* ( $\bar{H} = 17.5$  km,  $\partial_y H = 0.125$ ,  $\partial_x H = 0.08$ ) considers a case where the lithospheric thickness increases slowly from 15 km to 20 km over 40 km along-axis. In run *LST* ( $\bar{H} = 15$  km,  $\partial_y H = 0.25$ ,  $\partial_x H = 0.08$ ), it increases from 10 km to 20 km. Models *LST* and *SST* produced comparable faulting patterns, with a few notable differences, compared to Models *SS* and *LS*. The first key difference is that strain localization at the onset of extension in runs *SST* and *LST* occurs along a single pair of inward-dipping faults (1w and 1e, Figures 6-7 and 6-8) that accommodate the same amount of strain along the entire segment. By contrast, in runs *LS* and *SS*, faults 1w and

1e take up less extension in the segment center as they are complemented by faults 1'w and 1'e. In run *LS*, faults 1'w and 1'e localize simultaneously with 1w and 1e, while in runs *LST* and *SST* it takes another 5 km of extension for inward dipping faults (2w and 2e) to localize after the nucleation of faults 1w and 1e. These secondary faults appear far off-axis (~45 km), right next to the outer boundaries of the model domain. This fault geometry holds for another 10 km of extension, until a new pair of faults (3w and 3e) breaks at the axis, within the axial valley bounded by the primary faults 1w and 1e. In Model *SST*, faults 3w and 3e are relatively well-defined inward dipping faults running throughout the segment. Faults 3w and 3e root deeper in the lithosphere and therefore emerge further from each other at the thick end of the segment (Figure 6-7g, h). By contrast in Model *LST*, the along-axis continuity of faults 3w and 3e is ambiguous (Figure 6-8g, h and Figure 6-11c). At the segment end they are clearly inward dipping whereas at the segment center they are outward dipping. As one moves closer to the segment center, we find that the inward dipping faults cross at a shallower and shallower level, until they transition into outward dipping structures. In short, large along-axis slopes generate contrasting fault behavior from the center to the end of the segment. However, runs involving a greater average lithosphere thickness do not produce the same patterns of discontinuous faulting seen in Model *LS*.

#### **6.4.3. Fault evolution around an along-axis notch**

Finally, we investigated a “notched” case with an average lithospheric thickness of 10 km, but with the thinnest lithosphere placed in the middle of the extensional segment, and lithospheric thickening imposed on either side with a strong gradient of  $\partial_y H = 0.2$  (Model *NOTCH*). The initial faulting pattern resembles that of runs *SS* and *LS*, with two inward dipping conjugate faults (1w and 1e) defining an hourglass-shaped axial valley at the segment scale (Figure 6-9a, b). These faults are accompanied by two small inward dipping faults (1'w and 1'e), which form at the segment center and immediately propagate toward the thicker lithosphere at the segment ends at a rate of at least ~3 km per kilometer of extension (Figure 6-9c, d). Once both sets of primary faults cut through the entire segment, a stable pattern establishes itself where extension is distributed on the four faults, with faults 1'w and 1'e outlining an hourglass shape. As deformation

proceeds, thinning of the axial lithosphere is more rapid at the segment center (as indicated by the lines of equal lithospheric thickness on panels b, d, f and h of Figure 6-9), and this differential stretching reverses the curvature of faults 1w and 1e. This mechanism also affects faults 1'w and 1'e, but only locally, near the segment center. At the segment scale, faults 1'w and 1'e retain their initial curvature and the fault surfaces develop a pronounced downward concavity.

## 6.5. Discussion

### 6.5.1. Patterns of initial strain localization

In all simulations, most, if not all, of the deformation initially localizes along two inward dipping conjugate faults that root at the base of the layer where the lithosphere is thinnest, and outline an axial valley. This pattern is similar to that of many 2-D simulations [e.g., *Behn et al.* 2002b; *Behn et al.*, 2004; *Behn and Ito*, 2008], in which greater across-axis gradients in lithospheric thickness favor the focusing of a few faults near the axis as opposed to distributed faulting extending far off-axis. Intriguingly, the 3-D cases where initial faulting was least focused (*NOTCH*, *SS*, and *LS*) were characterized by the highest rates of across-axis thickening ( $\partial_x H$ ). However, these cases also had the lowest average on-axis lithospheric thickness (Table 6-2). It is therefore possible that the degree of initial fault focusing results from a competition between on-axis lithospheric thickness (with thinner lithosphere promoting distributed faulting) and the fast rate of off-axis thickening (with faster rates promoting focused deformation). To better quantify these competing effects, we introduce a length scale  $L_D$  corresponding to the across-axis distance over which the lithospheric thickness doubles from its axial value (Table 6-2). Since it is mechanically favorable for faults to form in regions of thinnest lithosphere, we envision that  $L_D$  could act as a proxy for the width of the region where faults can easily form. A lower  $L_D$  would therefore result in more focused faulting. Surprisingly, Models *NOTCH*, *SS* and *LS*, which all feature distributed initial deformation correspond to the lowest  $L_D$ . Our runs seem to indicate the opposite correlation (Table 6-2).

This being said, distributed initial deformation in runs *NOTCH*, *LS*, and *SS* was only observed in the thin segment center, where strain was partitioned onto 4 faults (1w,

1e, 1w, and 1e), while extension at the segment end was accommodated on 2 faults (1w and 1e). This suggests that three-dimensional effects may be a key control on the degree of focusing, and that the intuition developed from 2-D models may not be applicable here.

We note that each segment sees a variation in  $L_D$  from  $L_D^{THIN} = 2H_{THIN}/\partial_x H$  to  $L_D^{THICK} = 2H_{THICK}/\partial_x H$  from segment center to segment end. Since our runs assume constant  $\partial_x H$  along-segment, the variation in  $L_D$  directly reflects the along-axis variation in axial thickness. Models *SS*, *LS* and *NOTCH* are therefore characterized by the largest relative along-axis change in  $L_D$ , which may be the key to differing degrees of focusing along segment. Testing this hypothesis will require a more systematic exploration of parameter space. Further, by studying the degree of focusing in 2-D simulations with  $L_D$  characteristic of the segment center and segment end, we should be able to decipher the effect of across-axis lithospheric slopes from three-dimensional effects.

It should be noted that as extension proceeds, the lithosphere thins and the rates of across-axis thickening diminish near the axial region (see for example the evolution of the lines of equal lithospheric thickness in panels b, d, f, and h of Figure 6-4). Both of these effects act jointly to defocus the deformation, and lead to extensive faulting reaching tens of km off-axis in all our simulations.

Lithospheric thickness is also a direct control on the width of the axial valley outlined by the central V-shaped faults (1w and 1e). Earlier studies have attempted to quantitatively relate rift half-width to the rheology of the lithosphere, which is controlled by its compositional layering and geothermal gradient [*Shaw and Lin* 1996; *Behn et al.* 2002a; 2004]. In the present study the lithosphere is treated as a uniform brittle layer of varying thickness, and we find a similar correlation between the width of the axial valley and the thickness of the axial lithosphere. This relation is straightforwardly explained by the fact that the primary faults 1w and 1e in all simulations root along the location of thinnest lithosphere, and do not show significant change in dip along-axis. A good illustration is provided in Figure 6-8a and b (Model *LST*). The traces of the primary faults 1w and 1e form two parallel straight lines at depth, but emerge at the seafloor with a wider spacing on the thick end of the domain. This may contribute to the classic hourglass shape of axial valleys observed at many slow mid-ocean ridge segments

(Figure 6-2). The class of 3-D models presented here could therefore be applied in future studies to quantitatively relate along-axis variations in axial valley width to variations in lithospheric properties.

### 6.5.2. Continuity of faults along an extension segment

In this section we focus on the parameters controlling the along-axis continuity of individual faults along an individual extension segment. We specifically examine the conditions that favor the growth of faults that do not propagate along the entire segment and interact with each other in complex deformation relay zones (Figure 6-12). Hereafter, we refer to this faulting regime as "discontinuous". From the results of Models *FLAT*, *SS*, and *LS* (Figure 6-10), it appears that large along-axis slopes in the brittle-ductile transition favor discontinuous faulting, as seen in Model *LS* ( $\partial_y H = 0.2$ ). However, Model *LST*, which involved a greater average lithospheric thickness, produced continuous faults along-axis, despite having the largest along-axis slope of all our simulations ( $\partial_y H = 0.25$ ). This suggests that fault continuity is not controlled by  $\partial_y H$  alone, but rather the absolute change in lithospheric thickness from segment center to segment end ( $\partial_y H$  multiplied by the segment half-length) normalized by the average thickness  $\bar{H}$ . We call this ratio the relative along-axis thickening (RAT), which is zero in the *FLAT* case, and asymptotes 2 for very large values of  $\partial_y H$  or very long segments. In Figure 6-13, we map each simulation in a diagram of RAT versus the horizontal length scale over which the axial lithospheric thickness doubles ( $L_D$ ), which characterizes the relative rate of across-axis thickening.

We find that the simulation that produced discontinuous faulting (Model *LS*) is associated with the highest RAT. A high-RAT configuration corresponds to an overall thin lithosphere that thickens rapidly along-axis. These two characteristics act successively in the development of discontinuous fault populations in the segment center vs. segment end. As seen in Section 6.5.1, the small average lithospheric thickness of Model *LS* compared to Models *LST* and *SST* does not favor strong focusing of the deformation near the axis. Instead, it leads to partitioning the extension onto 4 faults (1w, 1e, 1'w, and 1'e) at the segment center, while runs with higher  $\bar{H}$  (*SST*, *LST*) see the

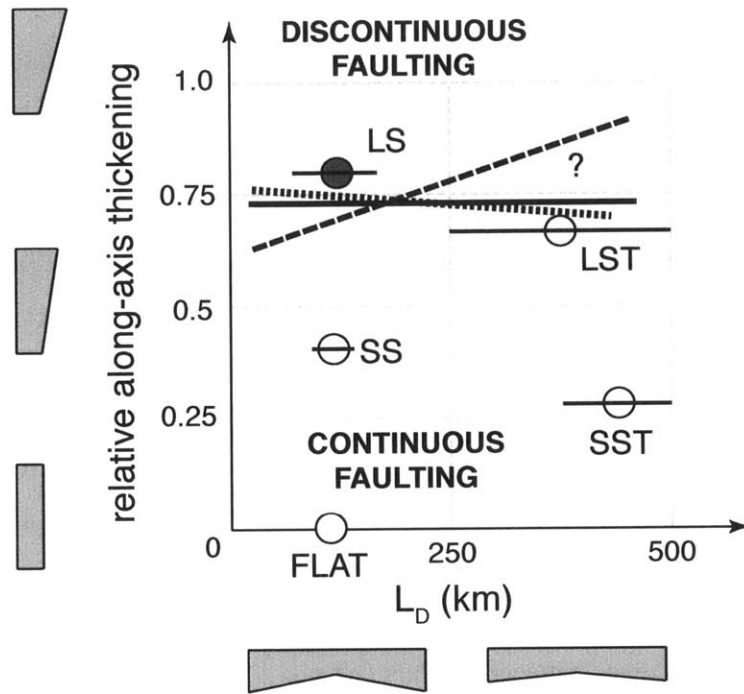


**Figure 6-13.** Regime diagram highlighting the combination of parameters that favor discontinuous faulting at the segment scale. The rate of along-axis thickening (RAT) is the absolute change in the thickness of the axial lithosphere from segment center to segment end normalized by the average thickness.  $L_D$  is the across-axis distance over which the lithosphere thickness doubles from its axial value. Runs that produced continuous and discontinuous faulting are plotted as white and gray circles, respectively. The horizontal bars crossing the circles indicate the full range of  $L_D$  from segment center to segment end. The solid, dotted, and dashed black lines indicate possible regime transitions, which are discussed in Section 6.5.2.

extension partition onto two faults throughout the segment. The onset of discontinuous faulting then depends on whether faults 1'w and 1'e can reach the end of the segment before a new fault nucleates there. This is achieved in Model SS, where faults 1'w and 1'e propagate at  $\sim 4$  times the extension rate. In Model LS, which features twice the along-axis slope of Model SS, propagation is  $\sim 2$  times slower and faults 1'w and 1'e never reach the thick side, where extension is partly accommodated on tertiary faults 3w and 3e. The

strong along-axis slope therefore causes discontinuous faulting by delaying the propagation of auxiliary faults 1'w and 1'e. By contrast, a low-RAT configuration characterized by thicker average lithosphere immediately focuses the deformation onto two faults. No auxiliary fault can therefore form and propagate, which enables along-axis continuity.

The relative rate of across-axis thickening may also affect fault continuity. Unfortunately, our exploration of parameter space remains too sparse to map a clear transition between a continuous and discontinuous faulting regime in RAT vs.  $L_D$  space. Specifically, it remains unclear how  $L_D$  may affect along-axis continuity. Intuitively, it is possible that rapid across-axis thickening favors fault continuity by forcing most of the faults to remain close to the axis, as discussed in Section 6.5.1. Doing so would limit the possibility of developing along-axis offsets between faults and / or force along-axis fault linkage. This scenario corresponds to a regime transition with a negative slope (dotted line in Figure 6-13). However, this negative slope would have to be small in order to accommodate the difference between Models *LST* and *LS*. On the other hand it is possible that the rates of across-axis thickening used in this study are so high that changing them does not significantly affect the run behavior. This would produce a horizontal regime transition (solid line in Figure 6-13). Finally, while the available data points appear compatible with a regime transition that has a positive slope (dashed line in Figure 6-13), it seems mechanically difficult to explain why faster off-axis thickening would favor discontinuous faulting. The solution may have to involve three-dimensional effects related to the relative changes in  $L_D$  along segment, as discussed in Section 6.5.1 for the degree of initial fault focusing. Future work will begin with refining our exploration of parameter space to clearly outline the regime transition.

If the strongest control on along-axis fault continuity is the RAT parameter, what prediction can we make for faulting at typical continental rift or slow MOR segments? Conversely, can we infer lithospheric properties from faulting patterns? The geometry of fault discontinuities and deformation relays obtained in run *LS* are surprisingly similar to the conceptual model of *Hayward and Ebinger* [1996] in which the segmentation of the Main Ethiopian Rift is set by the finite along-rift extent of graben-bounding faults (Figure 6-1). If the along-rift extent is set by variability in lithospheric thickness as suggested by

our numerical models, then the Main Ethiopian Rift should be characterized by an elevated RAT  $> \sim 0.75$ . Therefore, if we assume a representative faulted layer thickness of  $\sim 15$  km as inferred from the thickness of the seismogenic layer [Chen and Molnar, 1983], our models would require oscillations in thickness to the order of 11 km over the length scale characteristic of segmentation ( $\sim 50$ – $100$  km).

At slow-spreading MORs, the maximum depth of microseismicity used as a proxy for lithospheric thickness predicts a systematic increase from  $\sim 4$  km at segment centers to  $\sim 8$  km at segment ends [Kong *et al.*, 1992; Barclay *et al.*, 2001]. This yields a RAT value of 0.6, which on Figure 6-13 would plot in the "continuous faulting" regime. However small uncertainties (1 km) on these estimates place large uncertainties on the RAT value (between  $\sim 0.4$  and  $\sim 0.9$ ), which could potentially overlap into the "discontinuous faulting" regime. Our initial results are therefore ambiguous in terms of whether distinct fault populations are predicted to develop at the segment center versus the ends of slow-spreading ridge segments. We expect, however, that at slow-spreading MORs, along-segment variability in fault characteristics should be strongly controlled by the fraction  $M$  of total extension that is accommodated by magmatic emplacement at the axis [Buck *et al.*, 2005; Behn and Ito, 2008].

We are currently developing a numerical methodology to impose dike injection as an internal boundary condition in the finite difference / marker-in-cell framework. Our goal is to impose a variable rate of magma injection along-axis in order to model the scenarios shown in Figure 5-7. By pushing faults off-axis through thicker lithosphere, dike injection should simplify the sequence of faulting and force new faults to break systematically axis-ward of the earlier faults. It may also inhibit the growth of outward-dipping faults by sustaining steep across-axis thermal gradients that will focus faulting near the axis. It is possible that the segment center and segment end will behave in a similar fashion to 2-D models [Buck *et al.*, 2005; Behn and Ito, 2008], but that the along-axis gradients in lithospheric geometry investigated in the present study will be the controlling factors on the modes of transferring deformation along axis. This hypothesis will be tested by systematically varying  $\bar{M}$  and  $\partial_y M$  in conjunction with  $\bar{H}$ ,  $\partial_y H$ ,  $\partial_x H$ , and eventually lower-order parameters such as  $\partial_y(\partial_x H)$ .

### **6.5.3. Fault displacement profiles and fault linkage**

We now return to the only run that produced discontinuous faulting (*LS*) and briefly discuss the relay of deformation between faults 3e-3'e and 1'e (and their symmetric counterparts 3w-3'w and 1'w on the conjugate side, Figure 6-6f, h, and Figure 6-10c). These faults adopt a characteristic *en échelon* configuration with about 5 km of overlap in the along-axis direction. However, we see no linkage occurring during the simulation, which would take the form of a fault-oblique region of localized strain connecting fault 1'e and 3'e [Cowie, 1998 and references therein]. This could be due to the fact that the overlap is too large, and precludes strong stress concentration near the fault tips. This is consistent with the models of Crider and Pollard [1998], which showed that the Coulomb shear stress increase in between echelon normal faults is maximized for a given non-zero overlap. The Crider and Pollard [1998] geometry is however not directly applicable here because our closest overlapping faults (3'e and 1'e) have opposite dip directions. Alternatively, the opposing dip geometry could be the reason why fault linkage did not occur.

In Figure 6-12, we see that ~25% of the total extension is accommodated by faults 3e and 3'e. This amount transitions smoothly along-axis to ~50% of the total extension accommodated on fault 1'e alone. Further, the total displacement accommodated on individual faults decays smoothly, for instance at the tip of fault 1'e. Our simulation is therefore capable of resolving variable displacement along faults that do not cut along the entire domain. This suggests that this class of models should prove helpful to explain and eventually extract information from fault displacement vs. length scalings [Schlische *et al.*, 1996; Cowie and Scholz, 1992a; 1992b; Carbotte and Macdonald, 1994; Bohnenstiehl and Kleinrock, 1999].

### **6.5.4. On the applicability of 2-D scalings to 3-D fault growth**

In Chapters 2-5, the results of 2-D numerical models of normal fault evolution are well explained by simple 2-D force (or energy) balance models. The essential prediction of this analytical approach is that faults cutting through thinner elasto-plastic layers should be able to accommodate larger offsets [Buck, 1993; Lavier *et al.*, 2000]. The three-dimensional models presented here provide a unique opportunity to test the applicability

of this prediction to systems where the brittle layer thickens along-axis. Unfortunately, our initial simulations used a very fast weakening rate, which favored the nucleation of many simultaneous faults symmetrically about the axis, and has not allowed us to see clear abandonment of a fault in favor of another one. Instead, we see extension being partitioned on more and more faults. Interestingly, in the only run (*LS*) where faults evolved independently in the segment center versus the segment end, we find that after 20 km of extension more faults have developed at the segment end ( $n=8$ ) than at the segment center ( $n=6$ ). This is consistent with the 2-D prediction that new faults break more rapidly in thicker lithosphere due to a faster accumulation of stresses in the hanging wall and footwall blocks. Two-dimensional scalings may therefore be applicable to the variability of normal fault styles along a segment, provided the fault populations characteristic of segment ends are decoupled from the population characteristic of segment ends.

In addition, future work should focus on extending the 2-D energy budget model that underlies Chapters 2 and 3 into the third dimension. The mechanical cost of fault growth in 3-D can be divided into (1) overcoming the frictional resistance on the fault, (2) bending the lithosphere and sustaining topography, and (3) breaking new fault surface in intact lithosphere as the fault propagates along-axis. As detailed in Chapters 2 and 3, the key to achieving fault longevity is to limit the increase of each of those terms with increasing extension. By analogy with our 2-D model, the increase in the bending and topographic terms is likely controlled primarily by the average lithospheric thickness. The third energy term can be thought of as the product of a strain energy release rate and the surface area of the fault. It therefore depends on both the average lithospheric thickness and the along-axis geometry of the lithosphere. If we assume that the increase in energy required to break a new fault surface results primarily from along-axis fault propagation (i.e., the energy release rate and the vertical extent of the fault stay roughly constant throughout fault evolution), then its rate of increase with increasing extension should scale with the along-axis propagation rate of the fault. Our simulations (*SS* and *LS*, see Section 6.4.1) suggest that this rate is slower when the along-axis lithospheric slope is greater. Consequently, the ability of a fault to break through the entire segment from thin

center to thick end could result from a competition between the fault propagation velocity and the rate at which the bending and topographic terms increase.

#### ***6.5.5. Potential comparisons between models and observables***

The class of 3-D simulations presented in this chapter holds potential for direct comparison with observables. The present section outlines relevant datasets that can be used to validate or invalidate model assumptions using the example of a slow spreading MOR setting.

Seafloor bathymetry is the most straightforward observable to be compared to model outputs. At the segment scale, characteristic length scales such as the width and depth of the axial valley, the along-axis extent of a long-lived fault, or the spacing between successive faults can be extracted and compared with model predictions where lithospheric thickness and magma injection rates are varied systematically. In particular, comprehensive 3-D models should provide unprecedented insight into the along-axis component of the flexural processes that accompanies fault growth. For example, the mechanisms leading to the dome shape of oceanic core complexes have not yet been explored with 3-D models. It is therefore currently unknown whether the dome shape arises naturally from 3-D flexural readjustment to prolonged slip on a fault, or whether it requires additional controls such as a non-planar fault at depth, or a specific along-axis displacement profile on the fault perhaps accommodated with variable rates of melt intrusion along-axis. At a finer scale, detailed studies of individual fault scarps may be used to infer fault throw and curvature of the fault trace provided the bathymetry has not been substantially reworked by mass wasting.

Geophysical methods are necessary to image faults beyond their seafloor expression. Fault microseismicity as recorded by temporary OBS arrays can outline the sub-seafloor geometry of detachment systems, and shed some light on the maximum depth of brittle faulting as well as the curvature, concavity, and lateral extent of the fault at depth. To date, such a dataset is only available on a 2-D cross-axis section of the TAG detachment [DeMartin *et al.*, 2007]. New 3-D datasets on well-developed oceanic core complexes (e.g., at 13°20'N on the Mid-Atlantic Ridge) are expected to become available by early 2016. If the results of the *NOTCH* case hold over a wide range of parameter

values, a promising application of 3-D numerical models could be to quantitatively relate fault curvature and concavity to along-axis gradients in brittle layer thickness, which could then be confronted with the spatial distribution of microseismicity. If oceanic detachments develop their curvature from rooting in a "notched" lithosphere, the maximum depth of microseismicity should be greater near the along-axis edges of the fault than at the center.

In addition to microseismicity, passive seismic imaging methods can yield useful constraints for numerical models. While seismic reflection is notoriously difficult to apply to rugged axial terrains, it can prove useful to image fossil detachment systems that retain many characteristics of their active counterparts [*Reston and Ranero, 2011*]. This method has proven particularly helpful to identify rider blocks consisting of hanging wall material dissected by small steep faults that overlie a low-angle detachment. Numerical models can be used to determine the conditions that favor the formation of such rider blocks by extending the study of *Choi and Buck [2012]* into three dimensions. The necessary degree of weakening on the detachment fault that allows rider blocks to develop without terminating its growth is of particular interest, as are the along-axis extent and linearity of the steep faults that bound rider blocks.

Finally, 3-D generalizations of the models developed in Chapter 5 could make predictions of crustal architecture (in relation with faulting patterns) that are testable with seismic refraction studies, which have been shown to resolve lithological heterogeneities between ultramafic and gabbroic units exhumed in a detachment footwall on a fine (~ 5 km) scale [*Xu et al., 2009*]. Additional insight regarding lateral variations in crustal thickness and lithologies can be gained from potential field methods (gravity and magnetism). Because numerical models can keep track of crustal lithologies and tectonic rotation of magnetized units, a promising approach is to calculate the gravity and magnetic signature corresponding to a model output (using simple forward procedures), and to confront those directly with observations.

## 6.6. Conclusions and perspectives

We have conducted a three-dimensional study of spontaneous fault localization, propagation and interaction in a lithosphere of spatially varying thickness. The 3-D simulations presented here constitute an initial step toward complex 3-D modeling of rifting and seafloor spreading dynamics. The next step will consist of implementing a more realistic lithospheric rheology coupled with an evolving thermal structure. This will allow us to quantitatively investigate the tectonics of magma-starved continental rifts and ultraslow spreading ridges. Specifically, we will seek to extend the results of Chapter 2 to three dimensions and investigate the 3-D dynamics of fault rotation in relation to a 3-D energy balance model that incorporates along-axis fault propagation. Further, 3-D models can be straightforwardly coupled to realistic landscape evolution laws that need not make simplifying assumptions to represent erosion and sedimentation in the across rift dimension only. We will therefore attempt to generalize the results of Chapter 3 and focus on the effect of surface processes on fault propagation and linkage. Then, we will incorporate magma emplacement at spatially variable rates, and extend the results of *Buck et al.* [2005]; *Behn and Ito* [2008]; *Ito and Behn* [2008]; and Chapter 5 of this thesis to three-dimensions, in an attempt to produce self-consistent models of tectono-magmatic interactions at the segment scale.

An important part of the future work necessary to tackle complex 3-D problems will consist in improving the computational efficiency of our numerical code HiPStER. Implementing mesh refinement near the ridge axis coupled to a multigrid approach should significantly improve the computation speed. A major strength of the PETSc framework is that it allows great flexibility in the choice of solvers used to invert the  $J$  matrix (Section 6.2.2), and that those choices can be specified at run time. We will make use of this framework to systematically explore solver combinations and identify efficient strategies to solve for Stokes flow in a spatially heterogeneous visco-elasto-plastic medium, which is an open line of research in computational fluid dynamics.





## References

- Abers, G. A. (1991), Possible seismogenic shallow-dipping normal faults in the Woodlark-D'Entrecasteaux extensional province, Papua New Guinea, *Geology*, *19*, 1205-1208.
- Abers, G. A., Mutter, C. Z., and J. Fang (1997), Shallow dips of normal faults during rapid extension: Earthquakes in the Woodlark-D'Entrecasteaux rift system, Papua New Guinea, *J. Geophys. Res.*, *102*, 15301–15317, doi:10.1029/97JB00787.
- Agostini, A., Bonini, M., Corti, G., Sani, F., and P. Manetti (2011), Distribution of Quaternary deformation in the central Main Ethiopian Rift, East Africa, *Tectonics*, *30*, TC4010.
- Allken, V., Huismans, R. S., and C. Thieulot (2011), Three-dimensional numerical modeling of upper crustal extensional systems, *J. Geophys. Res.*, *116*, B10409.
- Allken, V., Huismans, R. S., and C. Thieulot (2012), Factors controlling the mode of rift interaction in brittle-ductile coupled systems: A 3D numerical study, *Geochem. Geophys. Geosyst.*, *13*(5), Q05010.
- Allken, V., Huismans, R. S., Fossen, H., and C. Thieulot (2013), 3D numerical modelling of graben interaction and linkage: a case study of the Canyonlands grabens, Utah, *Basin Research*, *25*, 1-14.
- Anderson, E. M. (1951), *The Dynamics of Faulting*, 2nd edition., Oliver and Boyd, Edinburgh, U. K.
- Armijo, R., Meyer, B., King, G. C. P., Rigo, A., and D. Papanastassiou (1996), Quaternary evolution of the Corinth Rift and its implications for the late Cenozoic evolution of the Aegean, *Geophys. J. Int.*, *126*(1), 11-53.
- Avouac, J. -P., and E. B. Burov (1996), Erosion as a driving mechanism of intracontinental mountain growth, *J. Geophys. Res.*, *101*, 17,747–17,769.
- Baines, A. G., Cheadle, M. J., John, B. E., and J. J. Schwartz (2008), The rate of oceanic detachment faulting at Atlantis Bank, SW Indian Ridge, *Earth Planet. Sci. Lett.*, *273*, 105-114.
- Balay, S., Gropp, W. D., McInnes, L. C., and B. F. Smith (1997), Efficient management of parallelism in object-oriented numerical software libraries, in *Modern Software Tools in scientific computing*, edited by E. Arge et al., Birkhauser Press.

- Barclay, A. H., Toomey, D. R., and S. C. Solomon (2001), Microearthquake characteristics and crustal  $V_p/V_s$  structure at the Mid-Atlantic Ridge, 35°N, *J. Geophys. Res.*, *106*, 2017-2034.
- Behn, M. D., and G. Ito (2008), Magmatic and tectonic extension at mid-ocean ridges: 1. Controls on fault characteristics, *Geochem. Geophys. Geosyst.*, *9*, Q08O10, doi:10.1029/2008GC001965.
- Behn, M. D., Lin, J., and M. T. Zuber (2002a), Mechanisms of normal fault development at mid-ocean ridges, *J. Geophys. Res.*, *107*(B4).
- Behn, M. D., Lin, J., and M. T. Zuber (2002b), A continuum mechanics model for normal faulting using a strain-rate softening rheology: Implications for thermal and rheological controls on continental and oceanic rifting, *Earth Planet. Sci. Lett.*, *202*, 725-740.
- Behn, M. D., Lin, J., and M. T. Zuber (2004), Effects of hydrothermal cooling and magma injection on mid-ocean ridge temperature structure, deformation, and axial morphology, in *Mid-ocean ridges: Hydrothermal Interactions between the lithosphere and oceans*, *Geophysical Monogr. Ser.*, *148*, edited by C. R. German et al., pp. 151-165, AGU, Washington D. C.
- Bercovici, D., and Y. Ricard (2014), Plate tectonics, damage and inheritance, *Nature*, *508*, 513-516.
- Beutel, E. K. (2005), Stress-induced seamount formation at ridge-transform intersections, *GSA Special Paper*, *388*, 581-593.
- Bialas, R. W., and W. R. Buck (2009), How sediment promotes narrow rifting: Application to the Gulf of California, *Tectonics*, *28*(TC4014), doi:10.1029/2008TC002394.
- Biot, M. A. (1961), Theory of folding of stratified viscoelastic media and its implications in tectonics and orogenesis, *Geol. Soc. America Bull.*, *72*, 1595-1620.
- Blackman, D. K., Karson, J. A., Kelley, D. S., Cann, J. R., Früh-Green, G. L., Gee, J. S., Hurst, S. D., John, B. E., Morgan, J., Nooner, S. L., Ross, D. K., Schroeder, T. J., and E. A. Williams (2002), Geology of the Atlantis Massif (Mid-Atlantic Ridge, 30°N): Implications for the evolution of an ultramafic oceanic core complex, *Mar. Geophys. Res.*, *23*, 443-469.
- Bodine, J. H., and A. B. Watts (1979), On lithospheric flexure seaward of the Bonin and Mariana trenches, *Earth Planet. Sci. Lett.*, *43*(1), 132-148.

- Bohnenstiel, D. R., and M. C. Kleinrock (1999), Faulting and fault scaling on the median valley floor of the trans-Atlantic geotraverse (TAG) segment, ~26°N on the Mid-Atlantic Ridge, *J. Geophys. Res.*, *104*(B12), 29351-29364.
- Bonatti, E., Ligi, M., Brunelli, D., Cipriani, A., Fabretti, P., Ferrante, V., Gasperini, L., and L. Ottolini (2003), Mantle thermal pulses below the Mid-Atlantic Ridge and temporal variations in the formation of oceanic lithosphere, *Nature*, *423*, 499-505.
- Bosworth, W. (1985), Geometry of propagating continental rifts, *Nature*, *316*, 625-627.
- Brown, J., Knepley, M. G., May, D. A., McInnes, L. C., and B. F. Smith (2012), Composable linear solvers for multiphysics, in *Proceedings of the 11th International Symposium on Parallel and Distributed Computing (ISPDC 2012)*, pp. 55-62.
- Buck, W. R. (1988), Flexural rotation of normal faults, *Tectonics*, *7*(5), 959-973, doi:10.1029/TC007i005p00959.
- Buck, W. R. (1991), Modes of continental extension, *J. Geophys. Res.*, *96*, 20,161-20,178.
- Buck, W. R. (1993), Effect of lithospheric thickness on the formation of high- and low-angle normal faults, *Geology*, *21*(10), 933-936.
- Buck, W. R., Lavier, L. L., and A. N. B. Poliakov (2005), Modes of faulting at mid-ocean ridges, *Nature*, *434*, 719-723.
- Burov, E. B., and A. N. B. Poliakov (2001), Erosion and rheology controls on synrift and postrift evolution: Verifying old and new ideas using a fully coupled numerical model, *J. Geophys. Res.*, *106*(B8), 16461-16481.
- Burov, E. B., and S. Cloething (1997), Erosion and rift dynamics: new thermomechanical aspects of post-rift evolution of extensional basins, *Earth Planet. Sci. Lett.*, *150*, 7-26.
- Byerlee, J. (1978), Friction of rocks, *Pure Appl. Geophys.*, *116*(4-5), 615-626, doi:10.1007/BF00876528.
- Canales, J. P., Collins, J. A., Escartin, J., and R.S. Detrick (2000), Seismic structure across the rift valley of the Mid-Atlantic Ridge at 23°20' (MARK area): Implications for crustal accretion processes at slow-spreading ridges, *J. Geophys. Res.*, *105*(B12), 28411-28425.

- Cann, J. R., Blackman, D. K., Smith, D. K., McAllister, E., Janssen, B., Mello, S., Avgerinos, E., Pascoe, A. R., and J. Escartin (1997), Corrugated slip surfaces formed at ridge-transform intersections on the Mid-Atlantic Ridge, *Nature*, 385, 329-332.
- Cannat, M. (1996), How thick is the magmatic crust at slow spreading oceanic ridges?, *J. Geophys. Res.*, 101(B2), 2847-2857.
- Carbotte, S. M., and K. C. Macdonald (1994), Comparison of seafloor tectonic fabric at intermediate, fast and superfast spreading ridges: Influence of spreading rate, plate motions, and ridge segmentation on fault patterns, *J. Geophys. Res.*, 99, 13609-13631.
- Chen, W.-P., and P. Molnar (1983), Focal depths of intracontinental and intraplate earthquakes and their implications for the thermal and mechanical properties of the lithosphere, *J. Geophys. Res.*, 88(B5), 4183-4214.
- Choi, E., and W. R. Buck (2012), Constraints on the strength of faults from the geometry of rider blocks in continental and oceanic core complexes, *J. Geophys. Res.*, 117, B04410, doi:10.1029/2011JB008741.
- Choi, E., Lavier, L. L., and M. Gurnis (2008), Thermomechanics of mid-ocean ridge segmentation, *Phys. Earth Planet. Interiors*, 171, 374-386.
- Choi, E., Tan, E., Lavier, L. L., and V. M. Calo (2013), DynEarthSol2D: An efficient unstructured finite element method to study long-term tectonic deformation, *J. Geophys. Res.*, 118, 1-16.
- Collettini, C. (2011), The mechanical paradox of low-angle normal faults: current understanding and open questions, *Tectonophysics*, 510, 253-268.
- Collettini, C., and R. H. Sibson (2001), Normal faults, normal friction?, *Geology*, 29(10), 927-930, doi:10.1130/0091-7613(2001)029<0927:NFNF>2.0.CO;2.
- Cooke, M. L., and S. Murphy (2004), Assessing the work budget and efficiency of fault systems using mechanical models, *J. Geophys. Res.*, 109, B10408.
- Cowie, P. A. (1998), Normal fault growth in three-dimensions in continental and oceanic crust, in *Faulting and Magmatism at Mid-Ocean Ridges*, *Geophys. Monogr. Ser.*, 106, edited by W. R. Buck et al., pp. 325-348, AGU, Washington, D. C.
- Cowie, P. A., and C. H. Scholz (1992a), Displacement-length scaling relationship for faults: Data synthesis and discussion, *J. Struct. Geol.*, 14, 1149-1156.

- Cowie, P. A., and C. H. Scholz (1992b), Physical explanation for displacement-length relationship for faults using a post-yield fracture mechanics model, *J. Struct. Geol.*, *14*, 1133-1148.
- Crameri, F., Schmeling, H., Golabek, G. J., Duretz, T., Orendt, R., Buitter, S. J. H., May, D. A., Kaus, B. J. P., Gerya, T. V. and P. J. Tackley (2012), A comparison of numerical surface topography calculations in geodynamic modelling: an evaluation of the 'sticky air' method, *Geophys. J. Int.*, *189*, 38–54, doi: 10.1111/j.1365-246X.2012.05388.x.
- Crider, J. G., and D. D. Pollard (1998), Fault linkage: Three-dimensional mechanical interaction between echelon normal faults, *J. Geophys. Res.*, *103*(B10), 24,373-24,391.
- Cundall, P. A. (1989), Numerical experiments on localization in frictional materials, *Ingenieur Archiv*, *59*, 148-159.
- DeMartin, B. J., Sohn, R. A., Canales, J. P., and S. E. Humphris (2007), Kinematics and geometry of active detachment faulting beneath the Trans-Atlantic Geotraverse (TAG) hydrothermal field on the Mid-Atlantic Ridge, *Geology*, *35*, 711–714, doi:10.1130/G23718A.1.
- Dempsey, D. E., Ellis, S. M., Rowland, J. V., and R. A. Archer (2012), The role of frictional plasticity in the evolution of normal fault systems, *J. Struct. Geol.*, *39*, 122-137 doi:10.1016/j.jsg.2012.03.001.
- Detrick, R. S., Needham, H. D., and V. Renard (1995), Gravity anomalies and crustal thickness variations along the Mid-Atlantic Ridge between 33°N and 40°N, *J. Geophys. Res.*, *100*, 3767-3787.
- Dick, H. J. B., Natland, J. H., Alt, J. C., Bach W., Bideau, D., Gee, J. S., Haggas, S., Hertogen, J. G. H., Hirth, G., Holm, P. M., Ildefonse, B., Iturrino, G. J., John, B. E., Kelley, D. S., Kikawa, E., Kingdon, A., LeRoux, P. J., Maeda, J., Meyer, P. S., Miller, D. J., Naslund, H. R., Niu, Y. L., Robinson, P. T., Snow, J., Stephen, R.A., Trimby, P. W., Worm, H. U., and A. Yoshinobu (2000), A long in situ section of the lower ocean crust: results of ODP Leg 176 drilling at the Southwest Indian Ridge, *Earth Planet. Sci. Lett.*, *179*, 31-51.
- Dick, H. J. B., Thompson, G., and W. B. Bryan (1981), Low-angle faulting and steady-state emplacement of plutonic rocks at ridge-transform intersections, *EOS Trans*, *62*(B10), 406.
- Dick, H. J. B., Tivey, M. A., and Tucholke, B. E. (2008), Plutonic foundation of a slow-spreading ridge segment: Oceanic core complex at Kane Megamullion, 23°30'N, 45°20'W, *Geochem., Geophys., Geosyst.*, *9*(5).

- Duretz T., May D. A., Gerya T. V., and P. J. Tackley (2011), Discretization errors and free surface stabilization in the finite difference and marker-in-cell method for applied geodynamics: A numerical study, *Geochem., Geophys., Geosyst.*, 12(7), Q07004.
- Elman, H. C., Howle, V. E., Shadid, J., Shuttleworth, R., and R. Tuminaro (2006), Block preconditioners based on approximate commutators, *SIAM J. Sci. Comput.*, 27(5), 1651-1668.
- Escartin, J., Hirth, G., and B. Evans (1997), Effects of serpentinization on the lithospheric strength and the style of normal faulting at slow-spreading ridges, *Earth Planet. Sci. Lett.*, 151(3-4), 181-189, doi:10.1016/S0012-821X(97)81847-X.
- Escartin, J., Mevel, C., MacLeod, C. J., and A. M. McCaig (2003), Constraints on deformation conditions and the origin of oceanic detachments: The Mid-Atlantic Ridge core complex at 15°45'N, *Geochem., Geophys., Geosyst.*, 4(8).
- Escartin, J., Smith, D. K., Cann, J., Schouten, H., Langmuir, C.H., and S. Escrig (2008), Central role of detachment faults in accretion of slow-spreading oceanic lithosphere, *Nature*, 455, 790-794, doi:10.1038/nature07333.
- Fialko, Y. A., and A.M. Rubin (1998), Thermodynamics of lateral dike propagation: Implications for crustal accretion at slow-spreading ridges, *J. Geophys. Res.*, 103(B2), 2501-2514.
- Forsyth, D. W. (1992), Finite extension and low-angle normal faulting, *Geology*, 20(1), 27-30, doi: 10.1130/0091-7613(1992)020<0027:FEALAN>2.3.CO;2.
- Garcés, M., and J. S. Gee (2007), Paleomagnetic evidence of large footwall rotations associated with low-angle faults at the Mid-Atlantic Ridge, *Geology*, 35, 279-282, doi:10.1130/G23165A.
- Gerya, T. (2010a), Introduction to numerical geodynamic modelling, Cambridge University Press, Cambridge, U. K.
- Gerya, T. (2010b), Dynamical instability produces transform faults at mid-ocean ridges. *Science*, 329, 1047-1050.
- Gerya, T. V. (2013), Three-dimensional thermomechanical modeling of oceanic spreading initiation and evolution, *Phys. Earth Planet. Interiors*, 214, 35-52.
- Gerya, T. V., and D. A. Yuen (2003), Characteristics-based marker-in-cell method with conservative finite-differences schemes for modeling geological flows with strongly variable transport properties, *Phys. Earth Planet. Interiors*, 140, 293-318.

- Gerya, T. V., and D. A. Yuen (2007), Robust characteristics method for modelling multiphase visco-elasto-plastic thermo-mechanical problems, *Phys. Earth Planet. Interiors*, 163, 83-105.
- Goetze, C., and Evans, E. (1979), Stress and temperature in the bending lithosphere as constrained by experimental rock mechanics, *Geophys. J. Roy. Astr. Soc.*, 59(3), 463-478.
- Harlow, F. H., and J. E. Welch (1965), Numerical calculation of time-dependent viscous incompressible flow of fluid with free surface, *Phys. Fluids*, 8(12), 2182-2189, doi:10.1063/1.1761178.
- Harris R. A., Smith R. B., Chang W. L., Meertens C., and A. Friedrich (2000), Temporal distribution of extensional strain across the southern Wasatch fault zone - Geological constraints for the GPS velocity field, *Eos Trans. AGU*, 81, p. 1230.
- Hayward, N. J., and C. J. Ebinger (1996), Variations in the along-axis segmentation of the Afar Rift system, *Tectonics*, 15(2), 244-257.
- Herman, F., Seward, D., Valla, P. G., Carter, A., Kohn, B., Willett, S. D., and T. A. Ehlers (2013), Worldwide acceleration of mountain erosion under a cooling climate, *Nature*, 504(423), doi:10.1038/nature12877.
- Hirth, G., Escartín, J., and J. Lin (1998), The rheology of the lower oceanic crust: Implications for lithospheric deformation at mid-ocean ridges, in *Faulting and Magmatism at Mid-Ocean Ridges*, *Geophys. Monogr. Ser.*, 106, edited by W. R. Buck et al., pp. 291-303, AGU, Washington, D. C., doi:10.1029/GM106p0291.
- Hooft, E. E., Detrick, R. S., Toomey, D. R., Collins, J. A., and J. Lin (2000), Crustal thickness and structure along three contrasting spreading segments of the Mid-Atlantic Ridge, 33.5°N - 35°N, *J. Geophys. Res.*, 105, 8205-8226.
- Ildefonse, B., Blackman, D. K., John, B. E., Ohara, Y., Miller, D. J., MacLeod, C. J., and Integrated Ocean Drilling Program Expeditions 304/305 Science Party (2007), Oceanic core complexes and crustal accretion at slow-spreading ridges, *Geology*, 35(7), 623-626.
- Ito, G., and M. D. Behn (2008), Magmatic and tectonic extension at mid-ocean ridges: 2. Origin of axial morphology, *Geochem. Geophys. Geosyst.*, 9, Q08O10.
- Jackson, J. A., and N. J. White (1989), Normal faulting in the upper continental crust: Observations from regions of active extension, *J. Struct. Geol.*, 11(1-2), 15-36, doi:10.1016/0191-8141(89)90033-3.

- Kaus, B. J. P., and T. W. Becker (2007), Effects of elasticity on the Rayleigh-Taylor instability: implications for large-scale geodynamics, *Geophys. J. Int.*, 168, 843-862.
- Kaus, B. J. P., and Y. Podlachikov (2006), Initiation of localized shear zones in viscoelastoplastic rocks, *J. Geophys. Res.*, 111(B04412).
- Keller T., May D. A., and B. J. P. Kaus (2013), Numerical modelling of magma dynamics coupled to tectonic deformation of lithosphere and crust, *Geophysical Journal International*, 195(3), 1406-1442.
- King, G. C. P., Stein, R. S., and J. B. Rundle (1988), The Growth of Geological Structures by Repeated Earthquakes 1. Conceptual Framework, *J. Geophys. Res.*, 93(B11), 13307–13318, doi:10.1029/JB093iB11p13307.
- King, G. C. P., Stein, R. S., and J. Lin (1994), Static stress change and the triggering of earthquakes, *Bull. Seismol. Soc. Am.*, 84(3), 935-953.
- Kong, L. S., Solomon, S. C., and G. M. Purdy (1992), Microearthquake characteristics of a mid-ocean ridge along-axis high, *J. Geophys. Res.*, 97, 1659-1685.
- Konstantinovskaia, E., and J. Malavieille (2005), Erosion and exhumation in accretionary orogens: Experimental and geological approaches, *Geochem. Geophys. Geosyst.*, 6(2), doi:10.1029/2004GC000794.
- Koons, P. O. (1989), The Topographic Evolution of Collisional Mountain Belts - a Numerical Look at the Southern Alps, New Zealand, *Am. J. Sci.*, 289, 1041–1069.
- Kuo, B.-Y., and D. W. Forsyth (1988), Gravity anomalies of the ridge-transform system in the South Atlantic between 31 and 34.5°S: Upwelling centers and variations in crustal thickness, *Mar. Geophys. Res.*, 10, 205-232.
- Lavier, L. L., and W. R. Buck (2002), Half graben versus large-offset low-angle normal fault: Importance of keeping cool during normal faulting, *J. Geophys. Res.*, 107(B6), doi:10.1029/2001JB000513.
- Lavier, L. L., Buck, W. R., and A. N. B. Poliakov (1999), Self-consistent rolling-hinge model for the evolution of large-offset low-angle faults, *Geology*, 27(12), 1127-1130, doi: 10.1130/0091-7613(1999)027<1127:SCRHMF>2.3.CO;2.
- Lavier, L. L., Buck, W. R., and A. N. B. Poliakov (2000), Factors controlling normal fault offset in an ideal brittle layer, *J. Geophys. Res.*, 105(B10), 23431-23442, doi:10.1029/2000JB900108.

- Le Pourhiet, L., Huet, B., May, D. A., Labrousse, L., and L. Jolivet (2012), Kinematic interpretation of the 3D shapes of metamorphic core complexes, *Geochem., Geophys., Geosyst.*, 13(9).
- Lin, J., Purdy, G. M., Schouten, H., Sempere, J. C., and C. Zervas (1990), Evidence from gravity data for focused magmatic accretion along the Mid Atlantic Ridge, *Nature*, 344, 627-632.
- MacDonald, K. C., and P. J. Fox (1988), The axial summit graben and cross-sectional shape of the East Pacific Rise as indicators of axial magma chambers and recent volcanic eruptions, *Earth Planet. Sci. Lett.*, 88, 119-131.
- Macdonald, K. C., Fox, P. J., Perram, L. J., Eisen, M. F., Haymon, R. M., Miller, S. P., Carbotte, S. M., Cormier, M.-H., and A. N. Shor (1988), A new view of the mid-ocean ridge from the behaviour of ridge-axis discontinuities, *Nature*, 335, 217-225.
- Macdonald, K. C., Scheirer, D. S., and S. M. Carbotte (1991), Mid-ocean ridges: Discontinuities, segments and giant cracks, *Science*, 253, 986-994.
- Macdonald, K. C., Sempere, J.-C., and P. J. Fox (1984), East Pacific Rise from Siqueiros to Orozco fracture zones: Along-strike continuity of axial neovolcanic zone and structure and evolution of overlapping spreading centers, *J. Geophys. Res.*, 89, 6049-6069.
- Mackwell, S. J., Zimmerman, M. E., and D.L. Kohlstedt (1998), High-temperature deformation of dry diabase with application to tectonics on Venus, *J. Geophys. Res.*, 103(B1), 975-984.
- MacLeod, C. J., Carlut, J., Escartin, J., Horen, H., and A. Morris (2011), Quantitative constraint on footwall rotations at the 15°45'N oceanic core complex, Mid-Atlantic Ridge: Implications for oceanic detachment fault processes, *Geochem., Geophys., Geosys.*, 12, Q0AG03, doi:10.1029/2011GC003503.
- MacLeod, C. J., Escartin, J., Banerji, D., Banks, G. J., Gleeson, M., Irving, D. H. B., Lilly, R. M., McCaig, A. M., Niu, Y., Allerton, S., and D.K. Smith (2002), Direct geological evidence for oceanic detachment faulting: The Mid-Atlantic Ridge, 15°45'N, *Geology*, 30(10), 879-882.
- MacLeod, C. J., Searle, R. C., Murton, B. J., Casey, J. F., Mallows, C., Unsworth, S. C., Achenbach, K. L., and M. Harris (2009), Life cycle of oceanic core complexes, *Earth Planet. Sci. Lett.*, 287, 333-344.
- May, D. A., and L. Moresi (2008), Preconditioned iterative methods for Stokes flow problems arising in computational geodynamics, *Phys. Earth Planet. Interiors*, 171, 33-47.

- Mohr, P. A., and C. A. Wood (1976), Volcano spacings and lithospheric attenuation in the eastern rift of Africa, *Earth Planet. Sci. Lett.*, *33*, 126-144.
- Molnar, P., and P. England (1990), Late Cenozoic uplift of mountain ranges and global climate change: chicken or egg?, *Nature*, *346*, 29-34.
- Moresi, L., Dufour, F., and H.-B. Mühlhaus (2003), Lagrangian integration point finite element method for large deformation modeling of viscoelastic geomaterials, *J. Comp. Phys.*, *184*, 476-497.
- Moresi, L., Quenette, S., Lemiale, V., Mériaux, C., Appelbe, W., and H.-B. Mühlhaus (2007), Computational approaches to studying non-linear dynamics of the crust and mantle, *Phys. Earth Planet. Interior*, *163*, 69-82.
- Morley, C. K. (1995), Developments in the structural geology of rifts over the last decade and their impact on hydrocarbon exploration, in *Hydrocarbon habitat in rift basins*, edited by J. J. Lambiase, *Geol. Soc. Spec. Pub.*, *80*, 1-32.
- Morley, C. K., Nelson, R. A., Patton, T. L., and S. G. Munn (1990), Transfer zones in the East African rift system and their relevance to hydrocarbon exploration in rifts, *AAPG Bull.*, *74*, 1234-1253.
- Mugnier, J. L., Baby, P., Colletta, P., Vinous, P., Balé, P., and P. Leturmy (1997), Thrust geometry controlled by erosion and sedimentation: A view from analogue models, *Geology*, *25*, 427-430.
- Murrell, S. A. F. (1976), Rheology of the lithosphere - experimental indications, *Tectonophysics*, *36*, 5-24.
- Naeser, C. W., Bryant, B., Crittenden, M. D. J., and M. L. Sorensen (1983), Fission-track ages of apatite in the Wasatch Mountains, Utah: An uplift study, in *Tectonics and stratigraphy of the Eastern Great Basin*, edited by D. M. Miller et al., *Geol. Soc. Am. Mem.*, *157*, 29-36, Boulder, CO.
- Olive, J.-A., and M. D. Behn (2014), Rapid rotation of normal faults due to flexural stresses: An explanation for the global distribution of normal fault dips, *J. Geophys. Res.*, *119*, doi:10.1002/2013JB010512.
- Olive, J.-A., Behn, M. D., and L. C. Malatesta (2014b), Modes of extensional faulting controlled by surface processes, *Geophys. Res. Lett.*, *41*(19), 6725-6733.
- Parry, W. T., and R. L. Bruhn (1987), Fluid inclusion evidence for minimum 11 km vertical offset on the Wasatch fault, Utah, *Geology*, *15*, 67-70, doi:10.1130/0091-7613(1987)15<67:FIEFMK>2.0.CO;2.

- Phipps Morgan, J., and D. W. Forsyth (1988), Three-dimensional flow and temperature perturbations due to a transform offset: Effect of oceanic crustal and upper mantle structure, *J. Geophys. Res.*, *93*(B4), 2955-2966.
- Phipps Morgan, J., and Y. J. Chen (1993), The genesis of oceanic crust: Magma injection, hydrothermal circulation, and crustal flow, *J. Geophys. Res.*, *98*(B4), 6283–6297, doi:[10.1029/92JB02650](https://doi.org/10.1029/92JB02650).
- Planert, L., Flueh, E. R., Tilmann, F., Grevemeyer, I., and T.J. Reston (2010), Crustal structure of a rifted oceanic core complex and its conjugate side at the MAR at 5°S: implications for melt extraction during detachment faulting and core complex formation, *Geophys. J. Int.*, *181*, 113-126.
- Poliakov, A. N. B., and W. R. Buck (1998), Mechanics of stretching elastic-plastic-viscous layers: Applications to slow-spreading mid-ocean ridges, in *Faulting and Magmatism at Mid-Ocean Ridges*, *Geophys. Monogr. Ser.*, *106*, edited by W. R. Buck et al., pp. 305–323, AGU, Washington, D. C.
- Pollack, H. N., Hurter, S. J., and J. R. Johnson (1993), Heat flow from the Earth's interior: analysis of the global data set, *Rev. Geophys.*, *31*(3), 267-280.
- Proffett, J. M. (1977), Cenozoic geology of the Yerington district, Nevada, and implications for the nature and origin of Basin and Range faulting, *Bull. geol. Soc. Am.*, *88*(2), 247-266, doi:[10.1130/0016-7606\(1977\)88 <247:CGOTYD>2.0.CO;2](https://doi.org/10.1130/0016-7606(1977)88<247:CGOTYD>2.0.CO;2).
- Püthe, C., and T. Gerya (2013), Dependence of mid-ocean ridge morphology on spreading rate in numerical 3-D models, *Gondwana Research*, *25*, 270-283.
- Rabain, A., Cannat, M., Escartin, J., Pouliquen, G., Deplus, C., and C. Rommevaux-Jestin (2001), Focused volcanism and growth of a slow spreading segment (Mid-Atlantic Ridge, 35°N), *Earth Planet. Sci. Lett.*, *185*, 211-224.
- Ranero, C. R., Phipps Morgan, J., McIntosh, K., and C. Reichert (2003), Bending-related faulting and mantle serpentinization at the Middle America trench, *Nature*, *425*, 367-373.
- Reston, T. J., and C. R. Ranero (2011), The 3-D geometry of detachment faulting at mid-ocean ridges, *Geochem. Geophys., Geosyst.*, *12*(7), doi:[10.1029/2011GC003666](https://doi.org/10.1029/2011GC003666).
- Ring, U. (2008), Extreme uplift of the Rwenzori Mountains in the East African Rift, Uganda: Structural framework and possible role of glaciations, *Tectonics*, *27*, doi:[10.1029/2007TC002176](https://doi.org/10.1029/2007TC002176).
- Schlische, R. W., Young, S. S., Ackerman, R. V., and A. Gupta (1996), Geometry and scaling relationships of a population of very small rift-related normal faults, *Geology*, *24*, 683-686.

- Schmalholz, S. M., and Y. Podlachikov (1999), Buckling versus folding: importance of viscoelasticity, *Geophys. Res. Lett.*, 26(17), 2641-2644.
- Schouten, H., Smith, D. K., Cann, J. R., and J. Escartin (2010), Tectonic versus magmatic extension in the presence of core complexes at slow-spreading ridges from a visualization of faulted seafloor topography, *Geology*, 38(7), 615-618.
- Searle, R. C., and A. S. Laughton (1977), Sonar studies of the Mid-Atlantic Ridge and Kurchatov Fracture Zone, *J. Geophys. Res.*, 82(33), 5313-5328.
- Segall, P. (2010), Earthquake and volcano deformation, Princeton University Press, Princeton, NJ.
- Shaw, P. R., and J. Lin (1993), Causes and consequences of variations in faulting styles at the Mid-Atlantic Ridge, *J. Geophys. Res.*, 98(21), 21,839-21,851.
- Shaw, W. T., and J. Lin (1996), Models of ocean ridge lithospheric deformation: Dependence on crustal thickness, spreading rate, and segmentation, *J. Geophys. Res.*, 101, 17,977-17,993.
- Small, C. (1998), Global systematics of mid-ocean ridge morphology, in *Faulting and Magmatism at Mid-Ocean Ridges*, *Geophys. Monogr. Ser.*, 106, edited by W. R. Buck et al., pp. 1-25, AGU, Washington, D. C.
- Spencer, J. E., and C. G. Chase (1989), Role of crustal flexure in initiation of low-angle normal faults and implications for structural evolution of the basin and range province, *J. Geophys. Res.*, 94(B2), 1765-1775, doi:[10.1029/JB094iB02p01765](https://doi.org/10.1029/JB094iB02p01765).
- Stock, G. M., Frankel, K. L., Ehlers, T. A., Scheller, M., Briggs, S. M., and R. C. Finkel (2009), Spatial and temporal variations in denudation of the Wasatch Mountains, Utah, USA, *Lithosphere*, 1(1), 34-40, doi:[10.1130/L15.1](https://doi.org/10.1130/L15.1).
- Strak, V. (2012), L'évolution du relief le long des escarpements de faille normale active: observations, modélisations expérimentales et numériques, Ph.D. Thesis, Univ. Pierre et Marie Curie, Paris, France.
- Tapponnier, P., and J. Francheteau (1978), Necking of the lithosphere and the mechanics of slowly accreting plate boundaries, *J. Geophys. Res.*, 83(B8), 3955-3970.
- Thatcher, W., and D. P. Hill (1991), Fault orientations in extensional and conjugate strike-slip environments and their implications, *Geology*, 19(11), 1116-1120, doi:[10.1130/0091-7613\(1991\)019<1116:FOIEAC>2.3.CO;2](https://doi.org/10.1130/0091-7613(1991)019<1116:FOIEAC>2.3.CO;2).
- Thatcher, W., and D. P. Hill (1995), A simple model for the fault-generated morphology of slow-spreading mid-oceanic ridges, *J. Geophys. Res.*, 100(B1), 561-570, doi:[10.1029/94JB02593](https://doi.org/10.1029/94JB02593).

- Tolstoy, M., Harding, A., and J. Orcutt (1993), Crustal thickness on the Mid-Atlantic Ridge: bulls-eye gravity anomalies and focused accretion, *Science*, 262, 726-729.
- Tucholke, B. E., and J. Lin (1994), A geological model for the structure of ridge segments in slow spreading ocean crust, *J. Geophys. Res.*, 99(B6), 11937-11958.
- Tucholke, B. E., Behn, M. D., Buck, W. R., and J. Lin (2008), Role of melt supply in oceanic detachment faulting and formation of megamullions, *Geology*, 36, 455-458.
- Tucholke, B. E., Lin, J., and Kleinrock, M. C. (1998), Megamullions and mullion structure defining oceanic metamorphic core complexes on the Mid-Atlantic Ridge, *J. Geophys. Res.*, 103(B5), 9857-9866.
- Tucholke, B. E., Lin, J., Kleinrock, M. C., Tivey, M. A., Reed, T. B., Goff, J., and G.E. Jaroslow (1997), Segmentation and crustal structure of the western Mid-Atlantic Ridge flank, 25°25'-27°10'N and 0 - 29 m.y., *J. Geophys. Res.*, 102(B5), 10203-10223.
- Turcotte, D. L., and G. Schubert (2002), *Geodynamics*, 2<sup>nd</sup> edition, Cambridge University Press, Cambridge, U. K.
- van Wijk, J. W., and D. K. Blackman (2005), Deformation of oceanic lithosphere near slow-spreading ridge discontinuities, *Tectonophysics*, 407, 211-225.
- Vening-Meinesz, F. A. (1950), Les grabens Africains résultants de compression ou de tension de la croûte terrestre?, *Bull. Inst. R. Colon. Belg.*, 21, 539-552.
- Wang, T., Tucholke, B. E., and J. Lin (2014), Spatial and temporal variations in crustal production at the Mid-Atlantic Ridge, 25°N - 27°30'N and 0-28 Ma, *submitted to J. Geophys. Res.*
- Watts, A. B. (2001), *Isostasy and flexure of the lithosphere*, Cambridge University Press, Cambridge, U.K.
- Watts, A. B., and E. B. Burov (2003), Lithospheric strength and its relationship to the elastic and seismogenic layer thickness, *Earth Planet. Sci. Lett.*, 213, 113-131, doi:10.1016/S0012-821X(03)00289-9.
- Weissel, J. K., and G. D. Karner (1989), Flexural uplift of rift flanks due to mechanical unloading of the lithosphere during extension, *J. Geophys. Res.*, 94(B10), 13919-13950, doi:10.1029/JB094iB10p13919.
- Wernicke, B., and G. J. Axen (1988), On the role of isostasy in the evolution of normal fault systems, *Geology*, 16(9), 848-851.

- Whipple, K. X. (2004), Bedrock Rivers and the Geomorphology of Active Orogens. *Annu. Rev. Earth Planet. Sci.*, 32, 151-185.
- Whitney, D. L., Teyssier, C., Rey, P., and W. R. Buck (2013), Continental and oceanic core complexes, *Geol. Soc. Am. Bull.*, 125, 273-298.
- Willett, S. D. (1999), Orogeny and orography: The effects of erosion on the structure of mountain belts, *J. Geophys. Res.*, 104, 28957-28981.
- Willett, S. D. (2009), Erosion on a line, *Tectonophysics*, 484, 168-180, doi:10.1016/j.tecto.2009.09.011.
- Xu, M., Canales, J. P., Tucholke, B. E., and D.L. DuBois (2009), Heterogeneous seismic velocity structure of the upper lithosphere at Kane oceanic core complex, Mid-Atlantic Ridge, *Geochem., Geophys., Geosyst.*, 10(10).
- Yang, Z., and W.-P. Chen (2008), Mozambique earthquake sequence of 2006: High-angle normal faulting in southern Africa, *J. Geophys. Res.*, 113, B12303, doi:10.1029/2007JB005419.
- Zhang, F., Lin, J, and W. Zhan (2014), Variations in oceanic plate bending along the Mariana trench, *Earth Planet. Sci. Lett.*, 401, 206-214.